ANALYSIS OF THE EFFECTIVENESS OF SPECTRAL MIXTURE ANALYSIS AND MARKOV RANDOM FIELD BASED SUPER RESOLUTION MAPPING IN THE CONTEXT OF URBAN COMPOSITION

D.R.Welikanna

December, 2007

ANALYSIS OF THE EFFECTIVENESS OF SPECTRAL MIXTURE ANALYSIS AND MARKOV RANDOM FIELD BASED SUPER RESOLUTION MAPPING IN THE CONTEXT OF URBAN COMPOSITION

by

D.R.Welikanna

Thesis submitted to the International Institute for Geo-information Science and Earth Observation in partial fulfilment of the requirements for the degree of Master of Science in Geo-information Science and Earth Observation, Specialisation: *Geoinformatics*

Thesis Assessment Board

Thesis advisors Dr.V.A.Tolpekin
Dr.Yogesh Kant
B.D.Bharath

Thesis Examiners Prof. Dr.Ir.A.Stein (Chairman)
Prof. Dr.Sanjeevi (External Examiner)

INTERNATIONAL INSTITUTE FOR GEO-INFORMATION SCIENCE AND EARTH OBSERVATION
ENSCHEDE, THE NETHERLANDS
&
INDIAN INSTITUTE OF REMOTE SENSING, NATIONAL REMOTE SENSING AGENCY (NRSA),
DEPARTMENT OF SPACE, DEHRADUN, INDIA

Disclaimer

This document describes work undertaken as part of a programme of study at the International Institute for Geo-information Science and Earth Observation. All views and opinions expressed therein remain the sole responsibility of the author, and do not necessarily represent those of the institute.

Abstract

The information in a pixel of satellite data within the instantaneous Field of View (IFOV) of the sensor is a mixture of different land cover types, and the individual land cover components can be estimated using soft classification techniques. However these techniques do not account for the spatial distribution of the class proportions, the information itself has a great relevance. Over the years techniques have been developed in attempting to provide an improved spatial distribution of land cover. Few studies have been tested on the difficult task of mapping the land cover from real satellite images, and more over a very few attempts have been done in a heterogeneous urban environment. Over the years the Markov Random Field (MRF) based Super Resolution Mapping (SRM) technique has been used for land cover classifications, and found to be an effective tool for the generation of land cover maps from remotely sensed images and it consider the spatial distribution of class proportions with in and between the pixels.

In this study MRF based SRM with certain modifications have been analysed for its performance with respect to the linear unmixing technique applied on hyperspectral data. To standardize the application of these techniques the urban environment was defined by the Vegetation, Impervious surface and soil (V-I-S) model which has been used as an accepted alternative in characterising the urban land cover components. Linear unmixing technique with a hyperspectral remote sensing image (Hyperion) has been used to generate fractions according to the spectral variability of the V-I-S classes. Modified MRF based SRM technique was applied on IKONOS, ASTER MSS and Landsat images with markedly different spatial and spectral resolutions. Those are the 3 band with 15m spatial resolution and 6 bands with 30m spatial resolution of the ASTER image, 4m spatial resolution of IKONOS image and the 6 bands with 30m spatial resolution of the Landsat image. Reference maps for the validation were created from the IKONOS MSS image using hard Maximum likelihood classification. And the super resolution maps which contain the spatial information were again turned in to fractions representing each class (V-I-S). The results of MRF based SRM technique and the linear unmixing technique were validated using three measures of accuracy with respect to the reference fractions of the IKONOS image, the Area error proportion (AEP), Root Mean Square Error (RMSE) and the Correlation Coefficient (CC). The results shows the improvement in the classification results by the proposed SRM methods over the Linear unmixing method and it also reveals the improvement of the class proportions due to the consideration of the spatial distribution of classes.

Several experiments were also carried out to understand the effects of different input image characteristics on MRF based SRM parameters. And the results suggest the parameters depend more on the spatial resolution than the spectral resolution of the images. The outcome of this study can be used for the better application of the MRF based SRM technique in super resolution land cover mapping.

Key words: *Linear spectral unmixing, MRF based SRM, Smoothness parameter, Neighbourhood size, Kappa coefficient, RMSE, AEP, CC*

Acknowledgements

It is with great pleasure I pay my gratitude to the people who have helped and encouraged me during the difficult and challenging time of this study, without you I would not have come this far.

Before thanking God, I would like to give all my gratitude to my first supervisor Dr.V.A.Tolpekin who made this work a success. I am indebted for his intelligent guidance over me. I highly appreciate his careful thoughts, invaluable comments, constructive suggestions and criticism and patients. And he has been a great teacher to me. Dear sir it has indeed been a great pleasure and a privilege for me to be your student.

I also would like extend many thanks to my IIRS supervisor Dr.Yogesh kant for the effort he has put in making this work a success, and also believing and encouraging me in this study period. You have really been a father to me. I also like to thank Mr.B.D.Bharath as my IIRS supervisor. I indebt gratitude goes to Dean, IIRS for selecting my candidature for the M.Sc program and the overall guidance during my research work. I would also like to acknowledge the support and encouragement rendered by all faculty and staff of IIRS and GID in particular during my study and stay in IIRS.

I am great full to the Sri Lankan parliament for awarding me the parliamentary scholarship and the Vice chancellor and the Dean of Faculty of Geoinformatics of the Sabaragamuwa University of Sri Lanka for helping me to follow this study.

Big thank go to all my Sri Lankan friends at ITC and IIRS, especially to *Nishantha, Jayasumana* and *Samantha* for showing me the real brotherhood at Enschede. *Krishanthi* I also thank you for the understanding and the encouragement you have given me, your are really an amazing and a special person in my life. I also thank all my Indian friends at IIRS, especially my dearest friend *Thushar* who has been a wonderful friend in my good and bad times, your friendship really made me come this far. I thank all my Sri Lankan friend back at home and especially *Derik* who teached me what life is. I thank my loving sister *Manuri*, though you are far a way I still love you.

Finally the love of my life my loving mother *Nimala* and my farther *Mahinda* , thank you for giving me this life. Thank you for bringing me up as a Buddhist and giving me a stable mind to think and work for science. Thank you for the prayers you have done for me back at home. It's because of you that I am standing here. "Ammi" your words gave me courage and strength, I am thankful to you for all what you have done for me. No words to describe my debt and my love for you may the "Triple Gem Bless You".

……..I dedicate this work to my loving Mother……..

"The scientific method is not a belief or religious dogma, but rather a manner of thinking and working towards more complete knowledge of the world.…...."

May God speed to you all……. I thank you!

Table of contents

List of figures

List of tables

1. Introduction

1.1. Background

The highly dynamic and heterogeneous nature, diverse material content (eg.Concrete, asphalt, metal, water, vegetation, and soil), and biophysical composition of an urban environment should be studied for important implications such as larger environmental system process controlling the cycling and processing of water, nutrients, carbon, and energy, issues related to human quality of life and the conservation of biodiversity [1]. With the increment of the world human population, urbanization is continuing to accelerate [2]. For sustainable urban development and to understand and manage the urban environment, accurate information about this urban land cover classes are very important. But the identification of these classes in a heterogeneous urban environment is a very difficult task. Under such circumstances remote sensing act as a highly productive tool in monitoring and understanding the urban morphology and its environment. In remote sensing several models and highly advance techniques have been developed for the study of urban land cover. One of the models developed to understand and to standardise the urban environment is described with the Vegetation- Impervious surface-soil (V-I-S) model [3]. This model is becoming an accepted alternative to parameterize biophysical composition of urban environments [4,5,6]. The model helps in understanding the urban/suburban environments in urban analysis. But the productivity of the remote sensing techniques depends on the ability of the technique to correctly categorize these land cover components for there spatial and spectral arrangement from the remote sensing images. Studying these techniques for there accuracies and productivity is also very important for the future of urban land cover studies.

Studies using Remote Sensing (RS) use different type of imageries. Hyperspectral images which correspond hundreds of wavelength channels for the same area on the surface of the earth have the ability to detect and identify individual materials or land cover classes in a highly efficient manner. With its high spectral resolution (narrow and continuous bands) hyperspectral images have an advantage over multispectral images to address the spectral variation of each V-I-S components in a heterogeneous urban environment. This is the pre requisite of its use in urban composition studies. But the problem associated with this is that images contain mixed pixels. Mixed pixels are the pixels in an image which represents a reflectance value corresponding to a combination of reflectances of several individual materials with in the Instantaneous Field Of View (IFOV) of the sensor. When a pixel observed by a sensor covering a large (low spatial resolution images) heterogeneous area on earth surface it tend to become a heavily mixed pixel.

Conventional classification techniques assign a single pixel into one land cover class, in the case of a coarse spatial resolution images this will directly effect the information extracted by the remote sensing image. Spectral Mixture Analysis (SMA) is utilized to calculate the land cover fraction within a pixel and model a mixed spectrum as combination of spectra for pure land cover types, called endmembers [7]. It does not show the spatial distribution of class proportions (spatial contextual information) within a pixel. Modelling the contextual information in land cover classification can

improve the accuracy of the classification significantly [8]. In this regard super resolution mapping (SRM) split the pixel into sub pixels and assigned the classes to the sub pixels depending on there spatial and spectral information, generating an image with higher resolution than the original image. A range of algorithms based upon knowledge-based analysis procedures, Hopfield neural networks, and linear optimization methods have been proposed for super resolution mapping [9,10]. Markov random field model is another method [11,12] of super resolution mapping and it describes the spatial dependencies quite accurately.

1.1.1. The V-I-S Model

The spatial composition of a segment of urban landscape may be classified by the Vegetation-Impervious Surface-Soil (V-I-S) model. Along the V-I axis lies a typical residential area, traditional commercial and industrial areas lie near I-S axis, the S-V axis along the bottom represents the land not yet urbanized, or the urban land undergoing changes. The V-I-S diagram demonstrates the need for a composition based (land cover) classification because it is land cover that can be sensed remotely not the land use that does not generate a signature.

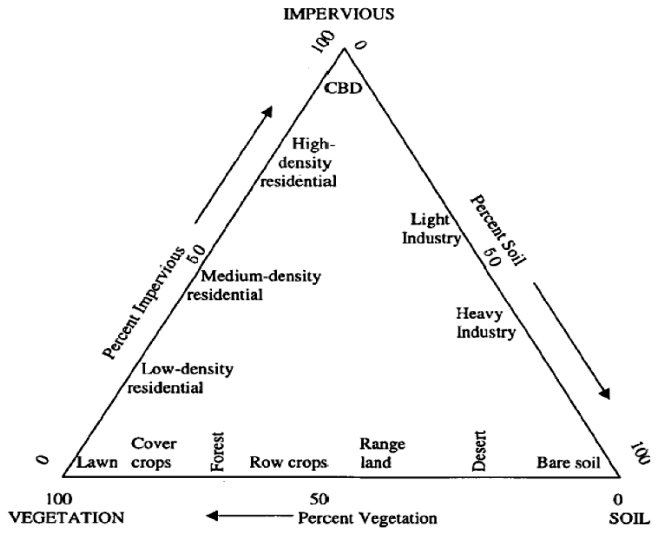

Fig 1. 1 Some urban and near urban features placed in the V-I-S model (Ridd, 1994)

Urban Impervious surface is a combination of low albedo (e.g. asphalt) and high albedo (e.g. glass and plastic). Due to the leaf characteristics, amount of chlorophyll content and the canopy elements (e.g. density shape, angle) the spectra of the vegetation may vary substantially. Similarly due to the water content, grain size, and the Iron concentration different type of soils demonstrate significant spectral variations. Due to these reasons, modelling such classes with the use of end-members is inadequate.

1.1.2. Spectral mixture analysis (SMA) and Super resolution mapping (SRM)

Remotely sensed data with the use of land cover classification can be used to characterise urban environment for its land cover components. In this discipline mostly a single image pixels is treated as the smallest unit in the image to be assigned to an independent land cover class. The problem encountered in characterizing land cover features (particularly in urban environment) using remote sensing data is to assign each pixels to exclusive classes which is difficult due to the mixed pixel

effect. Sub-pixel classification techniques in contrast overcome the problem of mixed pixels with respect to the conventional per pixel classification techniques. It has being utilized for calculating the land cover fractions within a pixel and involves modelling a mixed spectrum as a combination of spectra for pure land cover types called endmembers [4]. Depending on the complexity of the scattering SMA can also be subdivided into linear and non linear SMA techniques. For each class SMA techniques will provide its proportion within a pixel for the whole image as a fraction image.

Super-resolution mapping (SRM) is a technique that transforms a soft classification result into a finer scaled hard classification result [11]. Models which describes he movement of neighbouring particles has being tried to define the spatial dependence (i.e. spatially closer pixels tend to be more alike than the more distant ones [11]) between pixels which leads to the SRM. The "Ising Model" is one of them which says the neighbouring particles are more likely to rotate in the same direction or why intensity values of adjacent pixels of an image are more likely to be the same than different values. Later Markov random field models (MRF) has been implemented to describe the problems which were modelled by the Ising models. MRF model is a spatial-domain extension of a temporal Markov chain where an event at the current time instant depends only on events of a few previous time instants [13].

1.2. Problem Statement

Spectral mixture analysis technique with multispectral remote sensing images has been widely applied in the past to study the urban composition. Lot of technical difficulties has being arisen due to the spectral variation of each of the V-I-S components due to brightness differences and the limitations in the spectral resolution of the multispectral imageries. Hyperspectral images with their high spectral resolution have the ability to account for these brightness variations over the multispectral imageries. Very little attention in the past has been done to use the hyperspectral images to model the V-I-S components using SMA techniques over an urban environment.

The out put of SMA technique is set of fraction images each describing the proportion of a particular land cover class with in a pixel with respect to its pure spectra. Though the mixed pixel problem of the course spatial resolution images is addressed well by the SMA techniques, they do not account for the spatial distribution of the class proportions within the pixel. The ability of MRF to account for the spatial distribution, complexity of the scene and multiple land cover classes needs to be tested to identify the complex V-I-S components in a heterogeneous urban environment. According to Kasetkasem *et al*., 2003 the properties of MRF based super resolution mapping approach to accurately characterize the spatial distribution of the classes might give better classification results over the sub pixel classification techniques and this needs to be analyzed.

1.3. Research Objectives

The main objective of this research is to analyze the effectiveness of MRF base SRM approach in the context of urban subpixel composition analysis. It includes several sub objectives.

- Use the existing Markov Random Field based super resolution mapping method and modify it in order to apply on different spatial and spectral resolution images

- To integrate the advantages of hyperspectral images for the study of urban composition
- To study the effect of different input image characteristics on super resolution mapping and the determination of model parameters in the context of urban composition study
- Finally to compare the effectiveness of super resolution methods with the standard SMA techniques (Linear Unmixing)

1.4. Research questions

With the objectives of the study and past research outcomes several research questions were identified

1. Depending on the class definition and different resolution images how does the neighbourhood size relates to the scale factor for a best output results?

2. How do the optimal values of MRF based super resolution mapping internal parameters, i.e. neighbourhood size, normalized smoothness parameter change for different spatial and spectral resolution images?

3. How do the local specifics (e.g. smog and dust) affect the classification results?

4. What is the best method to asses the accuracy of the results (in the context of sub pixel classification)?

5. What is the effectiveness of MRF based SRM technique with respect to the linear unmixing technique?

1.5. Research approach

The area of study is a part of the Dehradun city, India. The area was chosen for several reasons. One is the availability of the images for that site, the proximity of the area in the case of a field check and its fast growing nature. This area contains most of the representative land cover classes like high and low density impervious, water, vegetation, exposed soil, etc. It has a high population growth and rapid urban expansion so it forms the basis of a complex urban environment which is also a prerequisite for the proposed study.

This research mainly focuses on two techniques of subpixel classification, the linear spectral mixture analysis and the Markov random field based super resolution mapping. These techniques will be tested in a complex urban environment and their performance will be compared. Multispectral images from ASTER, Landsat, and IKONOS sensor as well as hyperspectral image form Hyperion sensor will be used for this purpose. The conceptual frame work involved in the study for accomplishing its objectives is as follows.

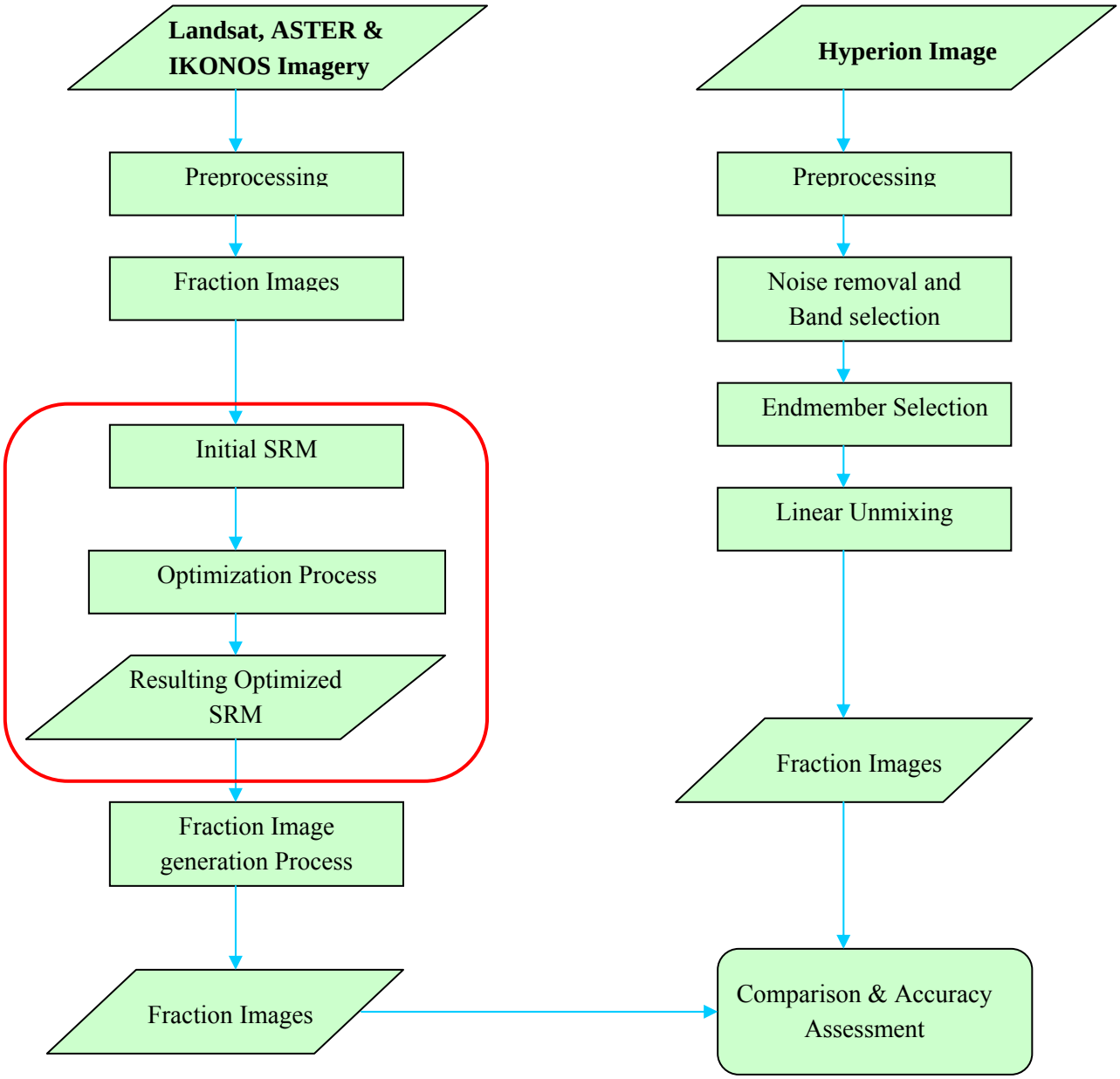

Fig 1. 2 The general methodology adopted for the study

1.6 Structure of the thesis

This thesis contains six chapters. The first chapter describes the background, objective and the conceptual frame work of the study. Chapter two describes the concepts of urban land cover mapping, image classification, limitations with the mixed pixels, and the methods developed to address it, and also some super resolution mapping techniques. Chapter three highlights the study area involved and the description of the data used and there pre-processing steps. Chapter four describes the Markov random field mathematical background, parallely with the method adopted in the application of it for this study. Chapter five review the results of the research with an analysis and discussion with respect to the data used. Chapter six conclude the study with some recommendation for the further research.

2. Urban-land cover mapping, spectral mixture analysis and super resolution mapping techniques.

2.1. Urban land cover mapping

Understanding the urban landscape for its structure with its rapidly alliterating manmade and natural objects is indeed a challenging task. Urban land is a composition of different land cover classes, ranging from natural to semi natural or totally man made, which can be directly observable on the land surface and it tend to change frequently within a small distance making it difficult to characterise them. Remote sensing technique with its moderate resolution satellite images helps to understand these as it capture the urban land cover types in timely and cost effective manner [14]. Traditional and most frequent, per pixel classification methods assigns an image pixel to a class which it has a high likelihood of being a member. Normally, this has been used to map the urban land cover types using the remote sensing images. Due to the heterogeneous nature of the urban landscape, an image pixel record more than one land cover class (mixed pixels) and these mixed pixels make the per pixel classification techniques inadequate for an urban land cover mapping. In order to solve the problem of mixed pixels [15], sub pixel classification techniques helps to retrieve the land cover information within the inherited pixel resolution.

Sub pixel classification techniques for the urban land cover mapping, work by quantifying the multiple class memberships for each pixel, which decompose the mixed pixel into required number of land cover classes. Spectral mixture analysis (SMA) has been widely used to divide these mixed pixels into its components. The linear SMA has so far been the most popular approach among the SMA family. It generates fractions of urban land cover classes according to the spectral variability inherited in the multi spectral or hyper spectral images [4]. To standardize the application of linear SMA in the urban land cover mapping, Ridd (1995) [3] first proposed the V-I-S model to represent the biophysical composition of an urban environment as vegetation impervious and soil. This model was later widely adopted as a scheme for choosing appropriate end members in linear SMA model for urban land cover mapping [16]. In the context of urban composition determination by sub pixel classification methods several attempts were made in the past but a study leading towards the super resolution mapping of these V-I-S components have not being tried. Literature review also suggests that the use of hyperspectral images has never been attempted for this purpose.

According to Ridd, V-I-S model helps to parameterize the biophysical composition of the urban environment and it can serve as the foundation for characterizing the urban/near-urban environments universally [3]. Further he proposed these models for urban change detection, growth modelling, environmental impact analysis from urbanization, energy and water related investigations and for certain dimensions of human echo system analysis of the cities.

Phinn in 2002 [16] used constrained spectral unmixing approach with Landsat Thematic Mapper data to identify the V-I-S composition. He stated that per pixel classification techniques do not produce

accurate results for urban land cover mapping and image data should have higher spatial resolutions for per pixel classification. He also pointed out that due to higher spectral variance of high spatial resolution images can create more problems.

In 2002 Wu and Murray [4] used spectral mixture analysis methods to investigate the impervious surface distribution using Landsat ETM+. They identified impervious surface as a major component of the V-I-S model and the difficulties in estimating it. They used fully constrained linear spectral mixture model to estimate the impervious surface distribution and pointed out the problem of assigning single pixel into one land cover type when a pixel contains multiple ground cover types.

Wu in 2004 [6] proposed a normalized spectral mixture analysis method to examine the urban composition. Using the brightness normalization method, brightness variability within each V-I-S component was reduced or eliminated. From the normalized image, three end members (vegetation, impervious surface, and soil) were chosen to model the heterogeneous urban composition.

2.1.1. Class Separability in image classification

Satellite image based land cover mapping and pattern recognition can be done through digital image classification techniques. Image classification techniques sort all the pixels in the digital image into a finite number of individual classes associated to number of land cover features on the ground given a pixel to satisfy certain number of conditions depending on the classes definitions, and this process is also known as image segmentation [17] .

Class separability is a statistical measure that indicates how well the classes can be separated during the classification process. For the Euclidean distance evaluation, the spectral distance between the mean vectors of each pair of class signatures is computed, if this distance is not significant for any pair of bands available they may not be distinct enough to produce a successful classification. In this study two main statistical parameters, the transformed divergence (TD) and the Jeffries-matusita distance (JM) for class separability has being used. Both these statistical measures take into account the co-variances of the signatures and there mean vectors for the bands being compared.

Transform Divergence (TD) is estimated as,

$$TDiver_{cd} = 2000[1-\exp(\frac{-Diver_{cd}}{8})]$$

$$Diver_{cd} = \frac{1}{2}tr[(V_c - V_d)(V_d^{-1} - V_c^{-1})] + \frac{1}{2}tr((V_c^{-1} + V_d^{-1})(\mu_c - \mu_d)(\mu_c - \mu_d)^T)$$

Where:

c,d=the two signatures(classes) being considered

V_c=the covariance matrix of signature c

μ_c=the mean vector of signature c

tr=the trace of a matrixc (i.e.,the sum of diagonal eliments)

T=the transpose function

The TD gives an exponentially decreasing weight to increasing distance between the classes [17]. The scale of the divergence values range from 0 to 2000, and a general rule suggests that if the result is

greater than 1900 then the classes can be separated, between 1700 and 1900 separation is fairly good and TD below than 1700 means that the separation is poor.

Jeffries-matusita distance (JM) is estimated as,

$$JM_{cd} = \sqrt{2(1-e^{-Bhat_{cd}})}$$

$$Bhat_{cd} = \frac{1}{8}(\mu_c - \mu_d)^T \left(\frac{V_c + V_d}{2}\right)(\mu_c - \mu_d) + \frac{1}{2}\ln\left(\frac{|(V_c + V_d)/2|}{\sqrt{|V_c| \times |V_d|}}\right)$$

Where:

$Bhat_{cd}$=Bhattacharyya distance

ln=the natural logarithm function

$|V_c|$=the determinant of V_c(matrix algebra)

JM has a saturating behaviour with increasing class separation like TD [17,18], but less efficient than the TD. The scale of the value ranges from 0 to 1.414.

2.1.2 Mixed pixels spatial scale and spatial-spectral trade off in urban land cover mapping

A mixed pixel is a result of the content of land cover types in the ground represented with in the instantaneous field of view (IFOV) of the sensor. Depending on the spatial resolution of the remote sensing system and the spatial scale of the surface features interested the amount of mixed pixels with in an image varies. Though with the high spatial resolution sensors such as IKONOS MSS provides images with 4m spatial resolution its limited number of spectral bands adds limitations in the production of an accurate land cover map. In contrast medium spatial resolution sensors such as ASTER MSS and hyper spectral sensors such as Hyperion provide larger range of spectral bands. But these images contain large number of mixed pixels depending on the scale of the surface features it maps.

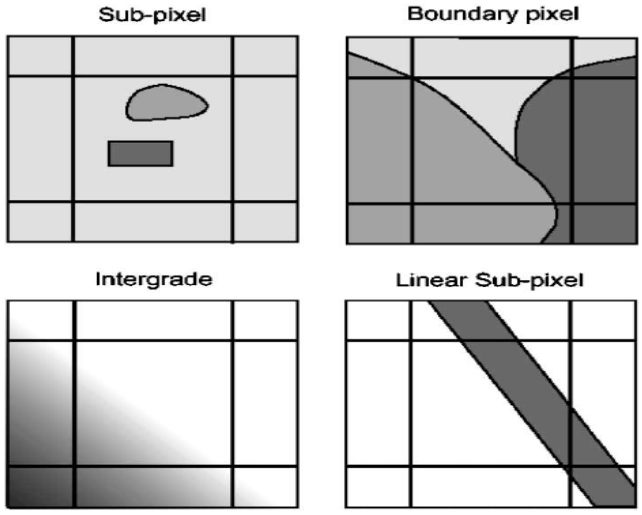

Fig 2. 1 Four cases of mixed pixels (Fisher 1997)

Figure 2.1 shows four types of mixed pixel occurrence. The presence of sub pixel objects, the spatial frequency of some urban land cover classes such as soil, built-up, and the mixed pixel response of the edge, pixels makes this medium resolution images contain large number of mixed pixels.

2.2. Linear Spectral Mixture Analysis

If the land cover classes are represented by there mean *m* and variance-covariance matrix *N,* with *n* being the number of spectral bands of the multispectral sensor, linear mixture modelling assumes that the spectral distributions of each land cover class are *n*-dimensional Gaussian distributions [1]. Assuming a normal distribution, the spectra of mixed pixel with land cover proportions $f = (f1,....., fc)^T$ is given by.

$$m\ (\ f\ )\ =\ \sum_{i=1}^{c}\ fi\ \times\ m_{\ i}$$

$$N\ (\ f\ )\ =\ \sum_{i=1}^{c}\ fi\ \times\ N_{\ i}$$

Where *m(f)* and *N(f)* can be considered as the mean vector and variance-covariance matrix of the multivariate normal distribution under the condition of the central limit theorem. The variance-covariance matrix will be valid only if the variables relating to the spectra of different land cover classes
are statistically independent [1]. This statistical independence means no multiple scattering between different land cover types, so that all photons within the instantaneous field of view (IFOV) of the satellite sensor are reflected from just one land cover type. This assumption may oversimplify the complex reflectance process of many land cover types, but most urban land covers like asphalts, roads or buildings show strong linear reflectance properties [1]. The land cover proportion of the mixed pixel can be approximated by inverting the statistical model, *m(f)* and *N(f)* shown above. The spectral signature of a mixed pixel is expressed as

$$x = Mf + e$$

Where, for *n* spectral bands and *c* is the reflectance components (represents the end member spectrum for each land cover type) of the endmembers for each of the spectral band. *M* is a $n \times c$ matrix of the end member spectra; f is the $c \times l$ vector of land cover class proportions, and *e* is a zero mean noise term. Endmember spectrum is defined from the reflectance properties of pure land cover type. The error vector, *e,* measures the statistical fluctuation around the mean value, and satisfies the condition of the multivariate normal distribution with a mean of zero and a variance-covariance of *N(f).* Model fitness is assed by the RMS error.

$$RMS = (\sum e^2 / N)^{1/2}$$

2.2.1. Endmember Extraction

Endmembers represents the pure features in a mixed pixel. Determining the endmember spectra, which consist of the columns of the matrix M is the most critical step in spectral unmixing process. This extraction of endmembers is involved in identifying the number of endmembers and their corresponding spectral signature [6]. When the end members are defined the spectral signature for the endmembers can be determined by different ways. Principle component analysis (PCA), linear regression analysis and K-mean clustering [1], the most common two methods involved and taken into consideration in this study are:

1. Optical approach using laboratory-based spectra from the field

2. From the pure pixels in the image itself (Supervised selection).

The advantage of the second method is that the endmembers can be collected with the similar atmospheric conditions. End-members can be collected from an image by various techniques. Pixel purity Index (PPI) which finds the most spectrally pure pixels in an image which corresponds to the unmixing endmembers. The PPI is calculated by plotting the n-dimensional scatter plots to 2-D space and noting down the most extreme pixels in each projection. The Endmember spectra consist of the columns of the M matrix, the final urban land cover proportion information is extracted from a remotely sensed image based on these end member spectra.

2.2.2. Singular Value Decompositioning for Linear Unmixing

In this study the linear unmixing was done through the Singular Value Decompositioning (SVD) technique. A singular value decomposition of a matrix X can be illustrated as follows.

$$X = UDV' = \sum d_a U_a V_a'$$

Here U is a $N \times A$ matrix. Its columns are the eigenvectors of XX' a $K \times A$ matrix. They are orthonormal. V is a $K \times A$ matrix. Its columns are eigenvectors of $X'X$. They are orthonormal.V is a diagonal matrix of size $A \times A$. The diagonal elements d_a are the singular values, the square roots of the eigenvalues λ_a of $X'X$ .A is the rank of X. The relationship with PCA is easily established:

$$X = \sum t_a p_a' = T'P$$

This means that the p_a from PCA are nothing but the v_a from SVD. The t_a from PCA are the products $d_a U_a$ from SVD [20].

2.3. Super resolution mapping and Markov random field models

Generation of a fine resolution land cover map from a coarse resolution image based on an accurate characterization of the spatial distribution of classes with in the mixed pixels is called sub-pixel

mapping or super resolution mapping. This approach accounts for the spatial distribution of the class proportions within the pixel [12].

MRF models have being applied for the various image processing tasks such as image classification, segmentation and change detection. The ability of MRF models to account for the spatial dependence between the classes proportions of the neighbouring pixels, in a very accurate manner can be used to refine the results from a subpixel classification more accurately. Under MRF models, the intensity values of pixels in a particular spatial structure (i.e. neighbourhood) are allowed to have higher probability (i.e. weight) than others [12]. In a remotely sensed land cover classification, when the spatial structure is usually in the form of homogeneous regions of land cover classes, a MRF model assigns higher weights to these regions than to the isolated pixels there by accounting for spatial dependence in the dataset.

The pioneering work by Geman and Geman (1984) [21] introduced a statistical methodology based on an MRF model. They assumed that a noiseless image contains MRF properties. Atkinson *et.al* [22] attempted to obtain the most suitable locations for the different class fractions within a pixel, assuming the spatial dependence, i.e. the tendency of neighbouring pixels to have closer value than distant ones.

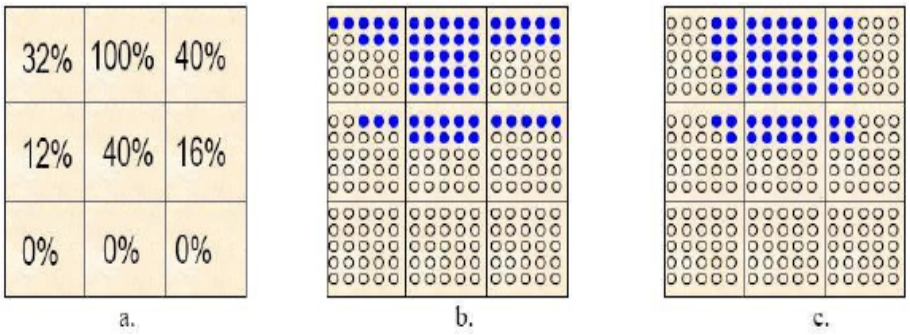

Fig 2. 2 Super resolution mapping (Atkinson 1997)

As above figure shows the SRM works by dividing the coarse spatial resolution pixels by a scale factor (S), the scale factor is the ratio between coarse and fine spatial resolution pixels in the row and column directions. Then these resulting sub pixels will be allocated with the land cover in a way which maximizes the spatial dependency between them. Above it is shown how the sub pixels are assigned to particular land cover proportion.

Sub pixel classification methods were applied to urban composition studies most of the times. It addresses the mixed pixels problem in course spatial resolution images. In 2003 Kasetkasem et al., [12] introduced Markov random fields to generate sub-pixel land cover maps. He pointed out that the ability of MRF to accurately characterize the spatial distribution of the classes might give better solutions over the sub pixel classification methods. In his study he has generated a fine resolution land cover map from the course resolution images. Kasetkasem mentioned that the sub pixel maps generated from MRF approach have the Markovian property i.e., two adjacent pixels are more likely to belong to the same land cover class than different classes which is likely to make a significant improvement in the accuracy of the sub pixel map over the conventional and most widely used methods.

Kasetkasem 2005 [23] used Markov random field based approach to generate super resolution land cover maps using IKONOS MSS and Landsat ETM+ images. He states that MRF models are well suited to represent the spatial dependence within and between pixels. He further studied the effectiveness of this method with the integration of the different spatial resolution images. Finally he concludes that accuracy of land cover mapping is significantly improved by this method.

Neher and Srivastava in 2005 [24] used the Markov random field base frame work to label the terrain using hyper spectral Images. They stated that hyper spectral data are more naturally treated as random and requires a statistical analysis. They identify two main goals of hyper spectral images namely libelling imaged terrains (Classification) or regions and target recognition.

Hailu 2006 [11] studied the suitability of Markov Random Field for land cover mapping with certain modifications on the existing method. She did modifications on the neighbourhood size with respect to the scale factor and also some modifications on the Gibbs potential parameter estimations. Then went on to conclude that with the proper parameters best results can be gained and also the capability of the method to cope with complexity of the scene and the multiple land cover classes makes it a highly potential method for the super resolution land cover mapping application.

This study tries to analyze the effectiveness of MRF based SRM techniques over the subpixel classification technique the linear unmixing. The study will take these two techniques to address the heterogeneous urban environment through the urban composition, which defines the urban landscape through V-I-S model. A detail discussion about the application of these methods will be provided in Chapter 4.

3. Study area and Data preprocessing

This chapter briefly describes the study area, the data involved in the study and there preprocessing steps. Mainly multispectral and hyperspectral data has being used for the study. The validation data set was also created from the remote sensing data. Section 3.1 describes the study area, section 3.2 and 3.3 describe the pre-processing of Hyperion data set. Subsequent section describes the pre-processing of ASTER, Landsat and IKONOS data sets, a brief introduction about the usage of R programming language in the study will be provide in the end.

3.1. Study area

Dehradun is the capital of Uttarakhand state, as well as it is the district headquarters. Uttarakhand is one of the newly formed states of India, out of the total population, 18.98% of the state is living in slums [25]. Among the six towns of this state Dehradun is one, which is situated in the Shiwalik ranges of the Himalaya, between 78^0 00'E to $78^0$10'E and $30^0$15'N to 30^0 25'E . The city enjoys its strategic location and undulating topography. Dehradun is a fast growing area and it contains most of the representative land cover and land use classes like high and low density residential, water, vegetation, exposed soil, business areas. It has a high population growth and rapid urban expansion. Many remote sensing images acquired over this area are subjected to mixing of spectral signatures. This is mainly due to high frequency of the land cover as a result of spatially mixed nature of most natural land cover classes, the frequency of sampling due to sensor spatial resolution, Point spread function (PSF) and resampling for geometric rectification [26]. Figure 3.1 shows the location of the study area. Because of the availability of the images, accessibility and the availability of the prior information of its urban land cover this area was selected for this study.

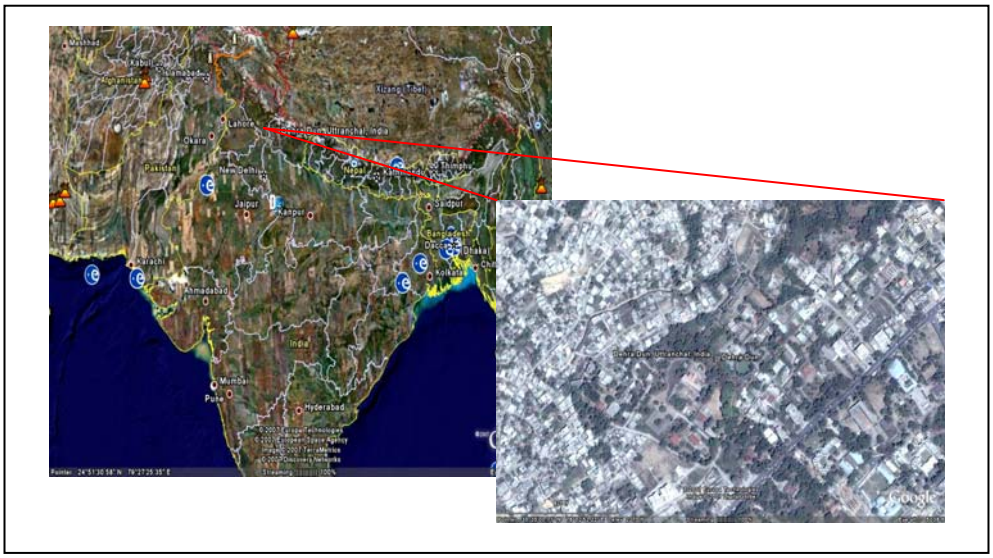

Fig 3.1 Location of the study area Dehradun, India, showing the heterogeneous urban environment *(source Google Earth)*

3.2. Hyperion Data

The data set of Hyperion over Dehradun was acquired on December 25, 2006. It contains a spectral range of 356-2576 *nm* at 10 *nm* band width and 220 unique bands. The Level 1 radiometric (L1R) product used in the study has 242 bands; only 198 of them are calibrated (band 8 to 57 for visible-to-near-infrared (VNIR) and 77 to 224 in shortwave-infrared (SWIR) regions). The over lap between the focal planes of VNIR and SWIR makes only 196 unique channels available. Due to low detector response all 242 bands are not calibrated and they are set to zero. The Hyperion sensor has a nominal ground instantaneous field of view (GFIOV) of 30m and 16 bit radiometric quantization [27]. Sensor characteristics of Hyperion are shown in the table 3.1.

Table 3.1 Hyperion sensor characteristics

Sensor altitude	705Km	No. of rows	256
Spatial resolution	30 m	No. of columns	3407
Radiometric resolution	16 Bits	VNIR range	0.45-1.35
Swath	7.2 Km	SWIR	1.40-2.48
IFOV*(mrad)*	0.043	No. of Bands	224

3.2.1. Level 1R pre-processing

Due to the large volume of data, numerous spectral bands, and the computational complexities high dimensional hyperspectral data processing is a very difficult and challenging task. Preprocessing is necessary not only to remove the sensor errors during the acquisition but for the corrections of the display, band selection (reducing data dimensionality) and to reduce the computational complexity. Hyperion dataset has to be corrected for abnormal pixels, striping and smiling effects prior to the atmospheric correction.

Hyperion data is initially processed by the EO-1 product generation system (EPGS) and distributed in different processing levels. In this study radiometrically corrected level 1R product of Hyperion has been used, and the understanding of the characteristics of the product is important for its Preprocessing. Level 1R is the out come of level 0 (raw) products which is subjected to four types of corrections, the dark current effect, sensor bias effect and two specific artefacts known to affect the (SWIR) region the SWIR smearing which is the leakage of signal from one pixel into the next readout pixel in the spectral direction and the SWIR echo, which occurs when the signal from one image echoes into another pixel. Radiometric correction applies sensor gain values which based on post-launch calibration coefficients. The radio metrically corrected image has a scaling factor of 40 and 80 for the VNIR bands and the SWIR bands respectively. Bad pixels for these data are determined during the pre-flight testing and listed to make a bad pixel mask, which is provided in the level 1R header files with additional updates for the scene capture day, this can be used to remove an average number of bad pixels. Due to the two sets of radiometers used to image the VNIR and SWIR regions a shift is there between these bands, so they are realigned to produce a single product. During this realignment actual SWIR bands are shifted across track by -1 field-of-view (FOV) in X direction and +1 pixel down track in Y direction. The predicted signal to noise (SNR) ratio performance of Hyperion is in range of 0-150 [27].

3.2.2. Band selection and identification of bad columns

Hyperion is a pushbroom type sensor; characteristically these sensors have poorly calibrated detectors. These detectors cause high frequency errors in the VNIR or SWIR regions, which can be identified as vertical strips in the image bands. In the level 1R products these vertical strips are not corrected. These stripping errors can affect the spectral characteristics of the Hyperion bands (also can effect the mean and slandered deviation of the data values for particular band), which would not facilitate the extraction of the calibration spectra from the data set for the linear unmixing. As an important preprocessing step these stripping effects should be balanced with there neighbouring columns.

Out of the calibrated bands of Hyperion (band 8 to band 55, band 56 and band57, band 79 to band 224), bands in the high water absorption range from 1400nm to 1900nm and bands which deemed to have unacceptable noise and streaking were removed from further processing. Hence, 150 bands from the 196 unique bands were selected. These selected bands were visually inspected for the bad columns to eliminate the stripping errors (see table 3.2). This helped to avoid the enforcing of severe changes in the original spectra.

Table 3.2 Location of bad columns in level 1R product for the Dehradun data set

Band	Bad Columns
15	114
16	114
55	32,34,37,39
56	32,33,37,39
57	33,36,38
90	90
94	90,91,92
190	112

The “Hyperion tool kit” was used to import the L1R product from HDF format to ENVI slandered format in ENVI 4.3 (Environment for Visualizing Images, Research System, Inc.). The Flag Mask correction option available in the tool kit was used to correct vertical striping, stripping will be removed by replacing the bad values with the average of the good values on either side of them [28]. The image was then visually checked to identify the left over bad columns. These were corrected by replacing there values by the average value from the two adjoining bands using ENVI spatial pixel editor

In addition to the vertical stripping an error common to the pushbroom sensors is caused by the low frequencies, and it is referred as the “smiling effect”. Smiling is the across track wavelength shift from the nominal centre wavelength. This wavelength shift is known to occur due to a change in depression angle with field position. The amount of shift is dependent on pixel position in the across track direction. The range of shift is reported to vary from $2.6\,nm$ to $3.5\,nm$. The maximum shift is recorded at pixel 256 at band 10 in VNIR region. The wave length shift affects the diagnostic absorption features in the spectra this influence the process of extraction of calibrated spectra from satellite platforms. The effect of ‘smile’ can be seen with Minimum Noise Fraction (MNF) transformation results. The first MNF image (see Appendix-A, fig A.2), shows a brightness gradient for the Hyperion

data, revealing the significant "smiling" effect in the image. This wavelength shift in Hyperion dataset cannot be ignored and has to be compensated for [29]. In this study specific correction for the "smiling" effect was not applied, it is also assumed as the noise in the data and, was accounted with the use of MNF transformation, this will be discussed in section 3.3.1.

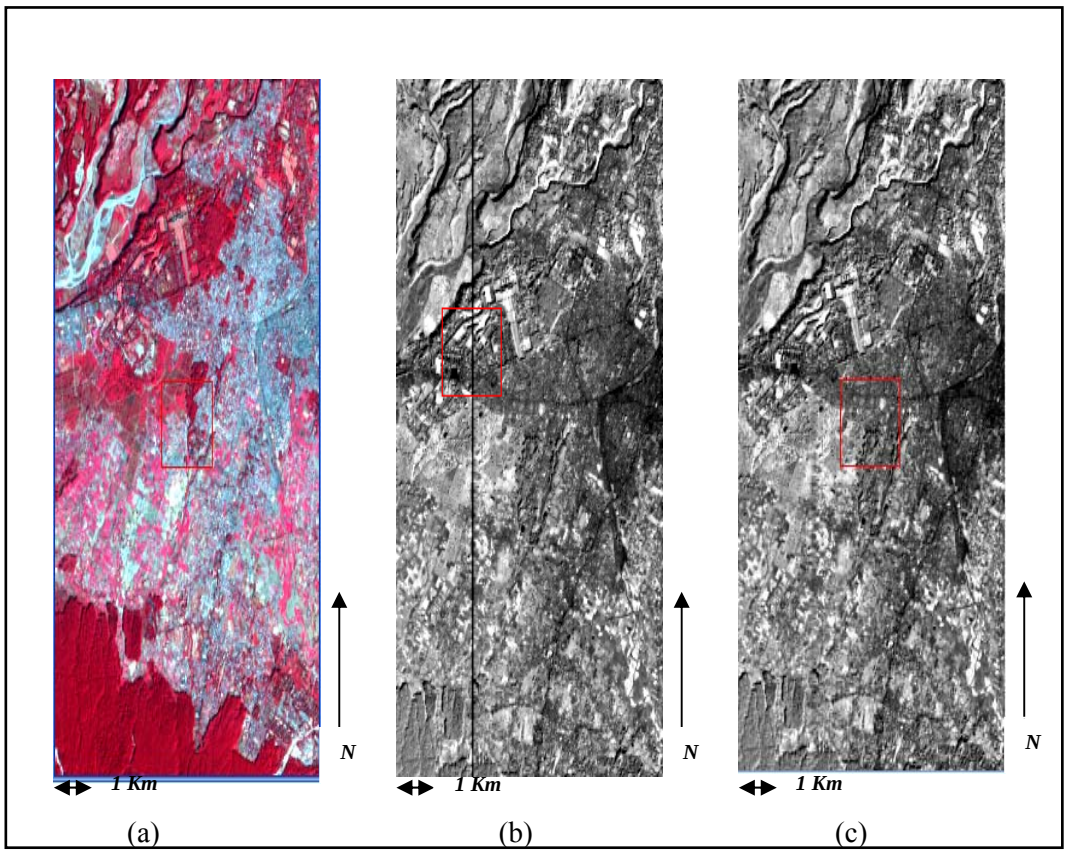

Fig 3.2 Hyperion scene over Dehradun: (a) false colour composite of Hyperion (b) Striping and smiling effect on band 94 of the Hyperion dataset (c) Bad column removed band 94 of Hyperion dataset

3.2.3. Atmospheric correction for the Hyperion image

The reflected solar radiation from earth surface in its way before red by the satellite sensor has to traverse through the intermediate atmosphere, and hence contains the information both of earth surface as well as that of the atmosphere. In order to only retrieve the surface reflectance and study the surface reflectance properties (which is important in the linear unmixing studies), the atmospheric components has to be removed. This is referred to as atmospheric correction and was applied to Hyperion data set. Atmospheric correction was achieved by using ENVI's fast line-of-sight atmospheric analysis of spectral hyper-cubes (FLAASH) module. FLAASH corrects wavelengths in the visible through near-infrared and short-wave infrared regions, up to 3 μm and it incorporates MODTRAN4 radiation transfer code [30].

Necessary parameters for the FLAASH were determined by the metadata of the image files. Flight date and time in GMT was taken from the header file of Hyperion L1 data product. The digital values

of the Level 1 products are in 16-bit radiances and stored as a 16-bit signed integer. The SWIR bands have a scaling factor of 80 and VNIR bands have a scaling factor of 40 as discussed earlier. The units are $W / m^2 SR\mu m$ [27].

VNIR L=Digital Number/40
SWIR L=Digital Number/80

An ASCII file was prepared for each band of the selected 150 bands, with a scaling factor of 40 for the first 43 bands of VNIR and 80 for the rest SWIR bands and provided as the scale factor file for the FLAASH to convert the DN values of the L1 data in to the units of radiance. The "Hyperion tool kit" was used to converts the file from ENVI native format, that is to BSQ, BIL or BIP format which are the needed formats for FLAASH to run. Parameters used for the atmospheric correction is provided below in the table 3.3.

Table 3.3 Parameters used in the FLAASH atmospheric correction

Scene Canter location	30.34020042 N 78.00659943 E	Initial Visibility	30 Km
Sensor Altitude	705Km	Spectral Polishing	Yes
Ground elevation	0.6 Km	Width (no of bands)	9
Pixel Size	30m	Wavelength Recalibration	No
Flight date	25.12.2006	Aerosol scale height	2.00Km
Flight time	5h 10m 58 sec	Co2 mixing ratio (ppm)	390 ppm
Atmospheric Model	Tropical	Use adjacency correction	Yes
Water retrieval	Yes	Modtran Resolution	15cm-1
Water absorption feature	1135 *nm*	Modtran Multiscatter Model	Scaled DISORT
Aerosol model	Urban	No of Disort streams	8
Aerosol retrieval	None	Output reflectance scale factor	10000

The results after the FLAASH atmospheric correction on the Hyperion image is shown with there respective spectral profiles in the fig 3.3 below. Significant change in the spectra can be seen after the atmospheric correction. As in the figure the reflectance spectra over a vegetation cover resembles its spectral signature.

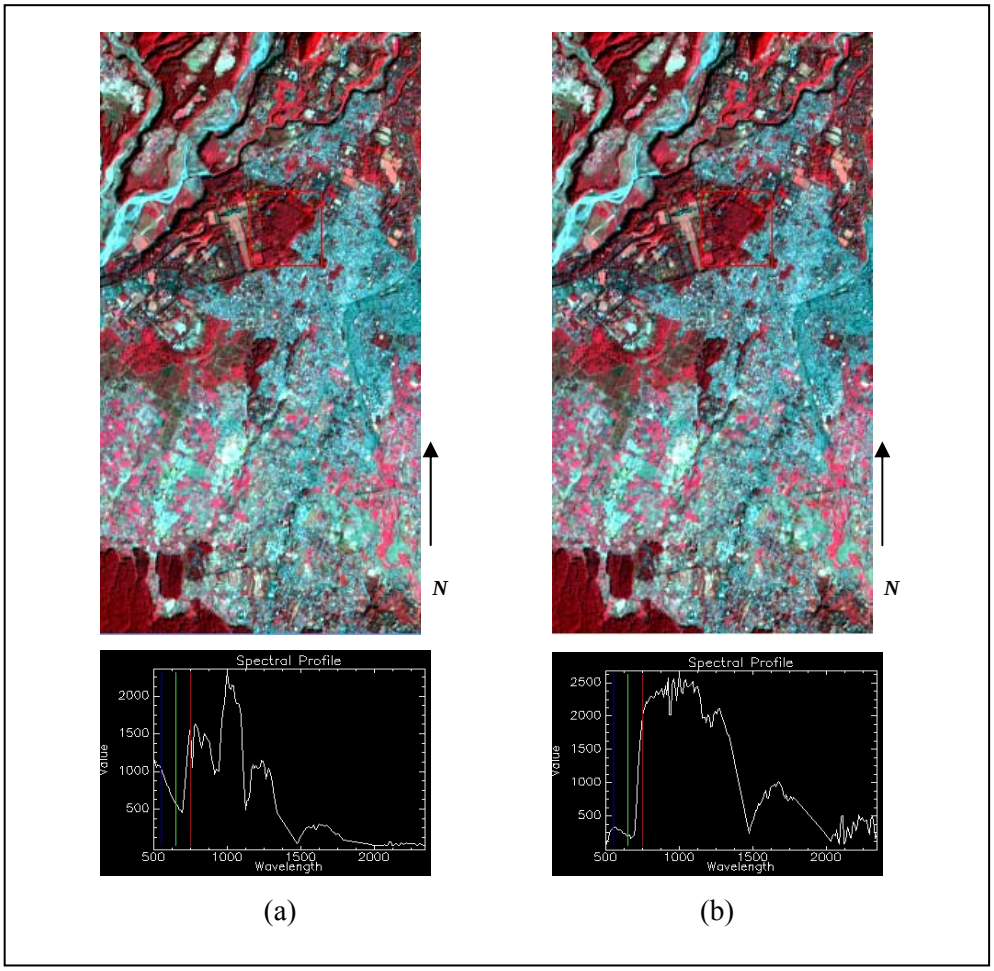

Fig 3.3 Atmospheric correction results from FLAASH (a) Hyperion false colour composite (FCC) for bands 40,30,20 and spectral profile before the application of FLAASH (b) The changes made for the image and for the spectral profile after the application of FLAASH

3.2.4. Image co-registration

As the objective of this study is to analyzing the super resolution mapping technique, the registration or co-registration between all the images is very important and critical. Registration should perform in a manner where all pixels in each image were supposed to be common to both images on a one-to-one basis. Registration is the process of making an image conforms to another image. For the purpose of this study, Hyperion data was co-registered to an Advanced Space borne Thermal Emission and Reflection radiometer (ASTER) image of the study area. ASTER image which was provided in geographic lat/long coordinate system was transformed to UTM with WGS84 north spheroid and datum, Zone Number 44 system. The pre-processing of the ASTER data and the purpose of co-registering Hyperion with it will be discussed in section 3.4.

Hyperion was used as the warp or target image and the ASTER image was taken as the base image. For the images to map perfectly the selection of the Ground Control Points (GCPs) should be very precise. Road intersections, Bridges and sharp distinct shapes which were dispersed around the image were selected carefully as GCPs. A total of 10 GCP points were selected for the co-registration process. First order polynomial model was used as the geometric model. The total RMS error was

0.078 pixels which is considered to be well enough for the SRM techniques. The pixels in the new grid may not be conformed to the pixels of the original grid so the pixels must be resampled. Resampling is the process of extrapolating data values for the pixels on the new grid from the values of the source pixels .For this study the resampling method used was the bilinear interpolation. Bilinear interpolation was selected because of its advantages over the basic nearest neighbour interpolation; it produces outputs which are smoother and does not contain the stair-stepped effect. And it is more spatially accurate than the nearest neighbour interpolation which is important in SRM studies, but some spectral integrity of the data can be lost during the rectification.

3.3. Preparation of Hyperion data for Linear Unmixing

Image classification is a more objective way of interpreting satellite images. Mixed pixels always bring in inaccuracies to the image classification results. Realistically the pixel consists of more than one surface feature. There for techniques accounting for the surface heterogeneity during image classification is highly important. Spectral unmixing technique is developed to derive fractions of spectrally pure materials that contribute to observed spectral reflectance characteristics of a mixed pixel using endmember spectra. The steps involved in the linear unmixing for the Hyperion data will be discussed in this section.

3.3.1. Band reduction and Endmember selection

Dimensionality reduction refers to the process by which the main components attributing to the spectral variance of the data set are identified and removed reducing the dimensionality of the data. This is also referred as the noise removal. The aim is to reduce the spurious information present in hyperspectral imagery so that it can be displayed in a minimized form without any changes to the original data. MNF transformation was implemented in this study to achieve this task. The MNF transformation is a linear transformation related to Principle components (PC) that orders the data according to signal-to-noise-ratio(S/N). It includes two principle component transformations in which the first transformation based on an estimated noise covariance matrix (correlation between the noise and the bands), de-correlating and rescaling the noise in the data; it is also assumed that the smiling effect is also accounted during this process. This results in a transformed data set in which the noise has a unit variance and no band–to-band correlations. The second step is standard PC transformation which creates several new bands containing majority of the information. With these two processes inherent dimensionality of the data will be preserved and noise will be segregated. After the transformation data space can be divided to two parts. One which is associated with large eigenvalues and coherent eigenimages, and a second with near-unity eigenvalues and noise-dominated images (see Appendix-A, figure A.2). By using only the portion with eigenvalues greater than one, noise can be separated from the data, which improves the spectral processing results [31].

Once applying the MNF technique on the 150 Hyperion bands we will get 150 new MNF bands. The image pixels are represented by eigenvalues, the dimensionality of the data will be determined by examining these values. When examining these values it is seen that first eight bands have the highest eigenvalues (>1) while the rest remain low values these low values are seen as noise. So the first eight bands of the MNF transformation were selected for the further processing.

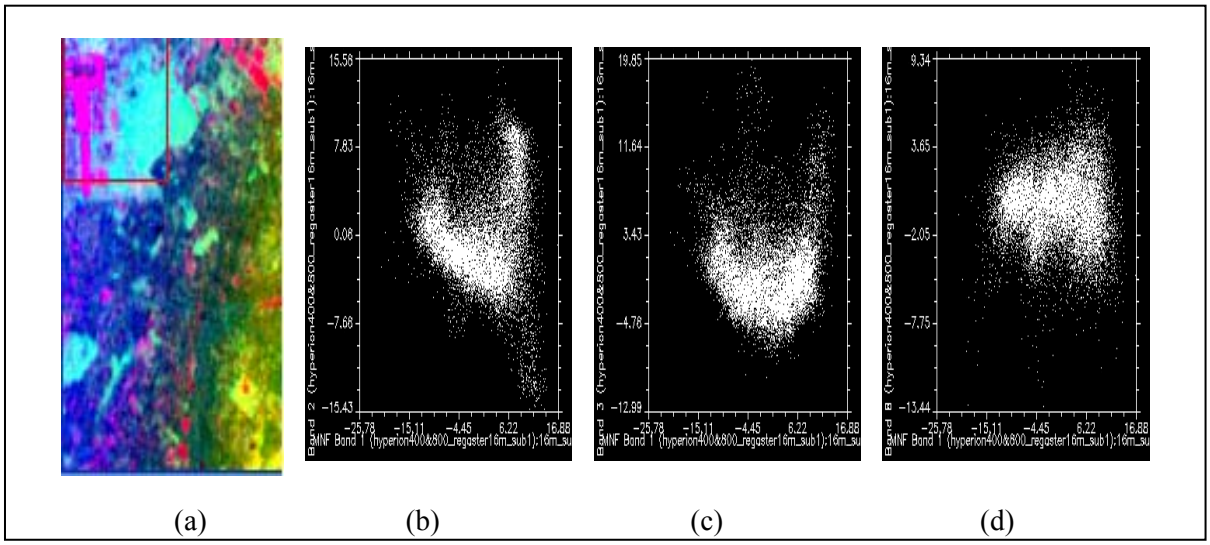

(a) (b) (c) (d)

Fig 3.4 (a) MNF image for band 2,3,1 in RGB,(b) Scatter plot between MNF band 1 and 2 (c) MNF band 1 and band 3 (d) MNF band 1 and 8

The MNF image (fig 3.4(a)) shows the interested land cover features sharply. The scatter-plots of the data in different MNF band combinations give an idea of the spectral data distribution. The arms or the separate clusters outside of the main data cloud are of special interest. These areas represent unique spectra called "end-members". These endmembers represent unique ground components. With the use of the scatterplot it is possible to identify these end members on the image.

Endmember selection

As stated before supervised selection of the end members has being implemented in this study to identify the end members for the V_I_S classes. In hyperspectral analysis purer pixels should be separated from the mixed pixels in order to reduce the number of pixels to be analyzed for the identification of the most pure pixels or the endmembers. The pixel purity index (PPI) identifies these pure pixels. And it can be used to find out the endmembers for each class. The most spectrally pure pixels typically corresponds to spectrally unique materials, these are the pixels to be find out as endmembers to perform the linear unmixing. The PPI signifies how many times the pixel is recorded in the extremes of the scatter plot. The value of a pixel in the PPI image corresponds to the number of times it was recorded as extreme pixel during the PPI process. Threshold of the PPI image can stipulate the most extreme pixels results in further spatial reduction. In this work the PPI was performed using the eight bands of MNF transformation. PPI was processed with 10000 iterations which is always better for the imaging of hyperspectral data (see Appendix-A, fig A.1). Threshold factor in data units was given as 2.5, which selects the pixels on the end of the projected vector or the proximity of each pixel to the convex hull of the data cloud. The threshold should be approximately two or three times the noise level of the data [31].

The "n-Dimensional Visualizer" which is an interactive tool in ENVI software, allowing the user to select end members in n-dimensional space was incorporated in this study to select the endmembers. This generates a cloud of points related to the pixels in an n-dimensional space defined by the MNF components. It gives you the ability to see the spectral data in many dimensions from many angles.

From here supervised selection of end members was done. A co-registered high resolution IKONOS segmented image was assisted for this supervised selection of endmembers.The preparation of this reference image is discussed in section 3.5 and the linear unmixing results of the Hyperion data will be discussed in Chapter 5.

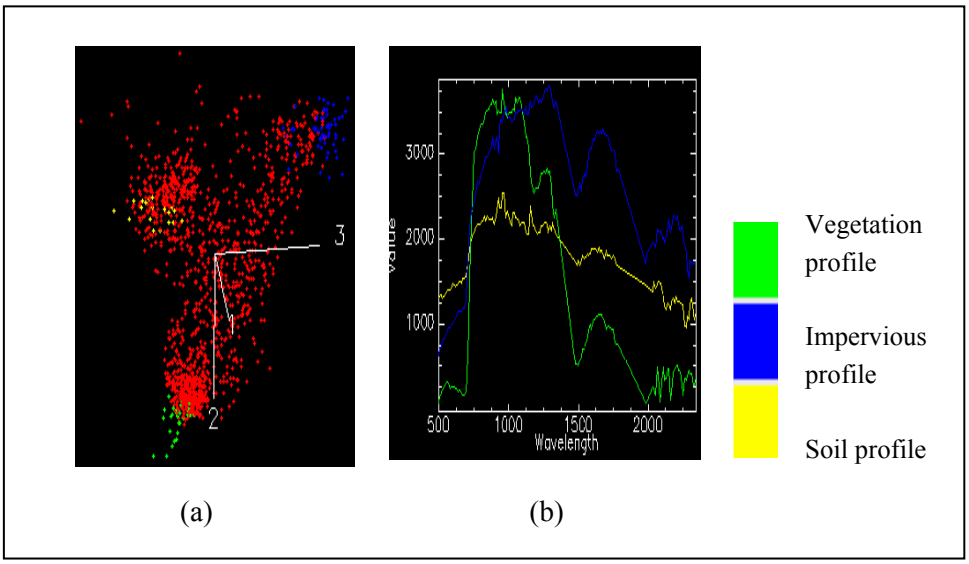

Fig 3.5 (a) Endmembers in n-Dimensional space of the MNF bands (b) and there respective spectral profiles.

3.4. Preprocessing ASTER Data

ASTER is a high efficient optical sensor which covers a wide region from the visible to thermal infrared by 14 spectral bands. In this study ASTER is selected as the main input for the MRF based SRM technique. The first three bands of the ATSER image in the VNIR region has a spatial resolution of 15m and the next six band in the SWIR region has a spatial resolution of 30m. These two regions were processed separately for the land cover classification using SRM. The digital values were recorded in unsigned 8bit values; the image was acquired on 1st November 2006 covering the Dehradun area. The spectral characteristics of the ASTER data are listed in table 3.4.

Table 3.4 Spectral characteristics of the ASTER data [32]

Band	Wave length (μm)	Spatial Resolution (m)	Radiometric Resolution
Band1(VIS)	0.52-0.60	15	Unsigned 8 bit
Band2(VIS)	0.63-0.69	15	
Band3N(NIR)	0.78-0.86	15	
Band4(SWIR)	1.600-1.700	30	
Band5(SWIR)	2.145-2.185	30	
Band6(SWIR)	2.185-2.225	30	
Band7(SWIR)	2.235-2.285	30	
Band8(SWIR)	2.295-2.365	30	
Band9(SWIR)	2.360-2.430	30	

3.4.1. Geometric correction and rectification

ASTER VNIR bands and SWIR bands were processed separately; preprocessing steps were mostly common for the both regions. First the processing of VNIR bands will be discussed and it will be followed by a discussion of the processing of the SWIR bands.

First the row ASTER data which has been provided in *HDF-EOS* format was imported to *img* format through ERDAS IMAGINE software before the necessary projection changes. Due to the curvature of the earth and type of the sensor used these raw images are subjected to distortions. During the import correction parameters have been used to perform a geometric rectification on the data that is to convert the data into different units. *Write transform* to image was used to rectify the data for panoramic distortion and calibrate the image by applying a 1st order polynomial transformation to the data. Then the rectification process was used to change the image from one grid system to another grid system using geometric transformation. The ASTER data was provided in geographic (lat/long) coordinate system with map units in degrees and seconds. A first-order polynomial transformation was used to transform the image from lat/long projection to UTM with WGS84 North spheroid and datum, Zone 44. The resampling method used here was bilinear interpolation as discussed earlier for its advantages for SRM. All the results and validations were done under this projection for all the images. During the projection transformation grid sampling determines the number of equally spaced samples to use (for X and Y) to complete the polynomial approximation. The original ASTER image comes with a grid sampling rate of 16 by 16 for the VNIR bands. In this study ASTER image has been kept in 16 by 16 grid sampling rate without changing the grid size. This helps to keep the spectral integrity of the original ASTER data intact. ASTER data covers a large area for the purpose of our study an area was selected as a subset with a good distribution of the V-I-S classes for the further analysis.

The six bands in the SWIR region were processed in the same manner as discussed above, but the grid size of the data was set to 30m in this case. Same area as in ASTER VNIR was taken as a subset for the further analysis. The FCC images belong to ASTER VNIR and SWIR regions are shown in fig 3.6.

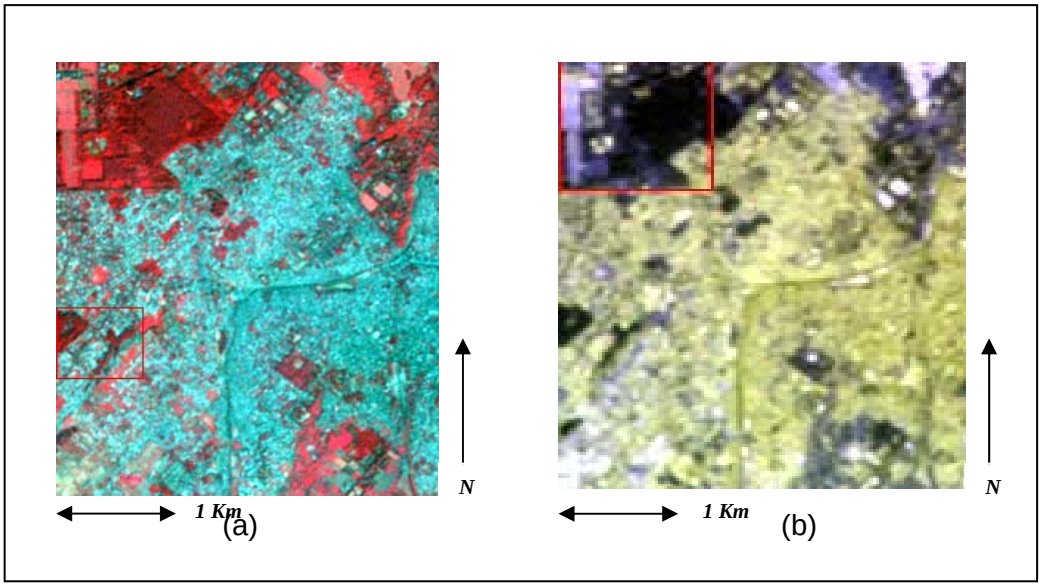

Fig 3.6 (a) ASTER (FCC) image for the study area in 16m resolution with VNIR spectral bands 3,2,1 (b) ASTER (FCC) image for the study area in 30m spatial resolution with SWIR bands 4,5,6 in combination.

3.5. Preprocessing of Landsat data

Landsat-7 data with ETM+ (Enhance Thematic Mapper) scanner was used in this study as another input for the MRF based SRM technique. Bands 1 to 5 and band 7 in visible (VIS) and SWIR regions with a spatial resolution of 30m was taken as the input for the study. The digital values of the image were recorded in unsigned 8bit values. The image was acquired over Dehradun on 25th November 2000. The spectral characteristics of the Landsat-7 ETM+ data is shown in table 3.5.

Table 3.5 Spectral characteristics of the Landsat-7 ETM+ data [33]

Band	Wave length (μm)	Spatial Resolution (m)	Radiometric Resolution
Band1(VIS)	0.45-0.52	30	Unsigned 8 bit
Band2(VIS)	0.52-0.60	30	
Band3N(VIS)	0.63-0.69	30	
Band4(NIR)	0.76-0.90	30	
Band5(SWIR)	1.55-1.75	30	
Band6(TIR)	10.4-12.5	60	
Band7(SWIR)	2.08-2.35	30	

3.5.1. Geometric correction and rectification

Row Landsat data provide in *GeoTIFF* format was imported through ENVI software and layer stacked to build the new multiband file. While layer stacking these bands were resampled and reprojected to UTM with WGS84 North spheroid and datum, Zone 44, and a pixel size of 30m. The resampling method used is the bilinear interpolation. The same subset area as for the previous images was taken for the further analysis. Then the Landsat image was compared with the ASTER (SWIR) image for evaluating the co-registration between the images using the viewer swipe in ERDAS IMAGINE software. As the Landsat image was turn to the same projection system as the ASTER (SWIR) image, the co-registration between the images found to be satisfactory. The resulting Landsat image is shown below in fig 3.7. A subset of this image corresponding to the previous subsets was taken from this image.

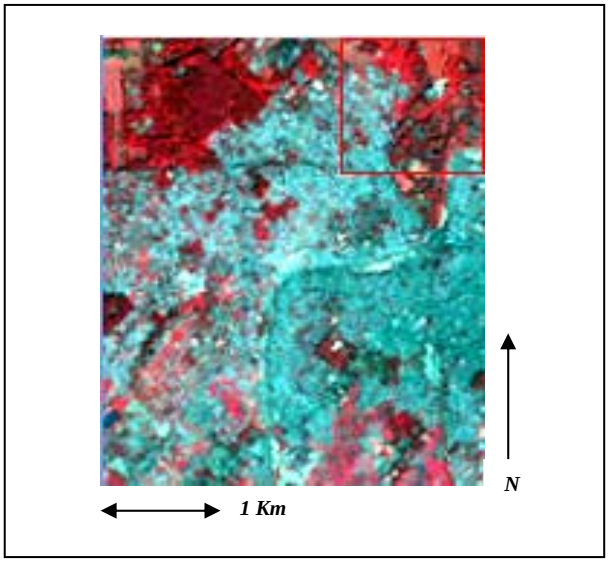

Fig 3.7 FCC of Landsat image for the study area in 30m resolution as a combination of bands 4, 3, 2

3.6. Preprocessing of IKONOS Multispectral data

For this study IKONOS data has being used as the reference image. IKONOS data records 4 channels of multispectral data at 4m resolution and one panchromatic channel with 1m resolution. Its high spatial resolution of 4m is the main factor of considering and processing it as the reference image. It has also being used as an input for the SRM to find out the efficiency of the technique. The IKONOS image for this study was acquired over Dehradun on 5th January 2005.Table 3.5 demonstrate these characteristics.

Table 3.6 Spectral characteristics of IKONOS data [34]

Band	Wave length (μm)	Spatial Resolution (m)	Radiometric resolution
Band 1	0.45-0.53(Blue)	4	Unsigned16 bit
Band 2	0.52-0.61(Green)	4	
Band 3	0.64-0.72(Red)	4	
Band 4	0.77-0.88(NIR)	4	

3.7. Image co-registration

As described earlier in this study the ASTER image was taken as the base image for the image co-registration. The row IKONOS multispectral image was in *TIFF* format for the VNIR bands. The digital values of the image were recorded in16 bit signed integer values. The four bands of the IKONOS image was layer stacked in ERDAS imaging software and saved in *img* format.

For the purpose of this study all the images were made to have the same projection that is the UTM projection. In the process of co-registration normally the high resolution image is taken as the base image. But in this study the main input for the SRM which is the ASTER image is used as the base image to avoid it being resampled. The modification of the geometric properties of the image pixels should be kept to a minimum, as the resampling can have serious effects on the SRM results. So the IKONOS image was treated as the "warp" image and was co-registered to the ASTER image. The registration was done for the VNIR band and the SWIR bands separately. In the case of SWIR bands the reference image was made to have a ground resolution of 5m, which enable us to have a scale factor of 6. There for in this case IKONOS image was degraded to 5m by applying the geometric correction on the image with no projection change but changing the out put cell size to 5m. The geometric correction was done with polynomial approximation using 1st order bilinear resampling method.

GCPs were selected very precisely and were well distributed over the image. A total of 10 GCPs were selected from the image. The geometric model was specified to be in first order. The RMS error was 0.207 and 0.161 pixels for the ASTER VNIR and SWIR bands respectively. Resampling was done using bilinear interpolation. In the case of Landsat image, as it was having a good registration with the ASTER (SWIR) with the projection change to UTM with WGS84 North spheroid and datum, Zone 44 projection, the same IKONOS reference image produced for the ASTER (SWIR) image, was used as the reference image.

For the analysis of the Markov Random Field based SRM technique for its efficiency without the introduction of registration errors and the errors due to class definitions as discussed in depth in Chapter 4, the IKONOS image was degraded to 16m spatial resolution and taken as an in put for SRM. This was done by aggregating four by four pixels of IKONOS image and getting the mean of them to represent a pixel in the degraded 16m IKONOS image. This process was performed using R programming language and environment for statistical computing, version 2.5.0 (see section 3.9) [35]. The IKONOS image subset for the SRM input is shown below in fig 3.7. A good distribution of the V-I-S classes can be recognized through the visual interpretation of the image.

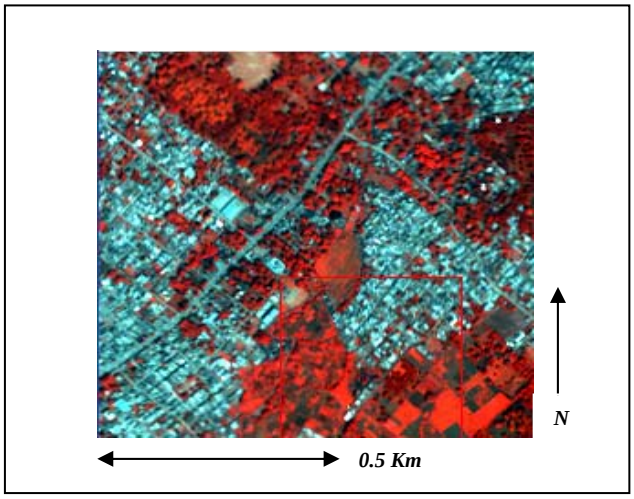

Fig 3.8 IKONOS (FCC 4,3,2) multispectral image subset of the study area

3.8. Preparation of reference images

To analyze the accuracy of the super resolution maps several reference images were prepared using the hard maximum likelihood classification (MLC) technique. Considering the co-registration aspects and the training set pixels, reference maps for the ASTER (VNIR) image, ASTER (SWIR) image and the Landsat image were produced separately. For the SRM technique defining the class covariance and mean vectors is an extremely important step. The likelihood energy of the MRF model depends on the definition of these statistics, a more descriptive discussion will be done on this matter in Chapter 4.There for the training set pixels defined on ASTER and Landsat images for the V-I-S classes were transferred to the IKONOS image. This is to make the reference image to have same pixels as the SRM input image. Then the IKONOS image was classified using maximum likelihood classifier to prepare the reference data set. This procedure was followed for both ASTER data sets with different spatial resolutions and for the Landsat dataset separately.

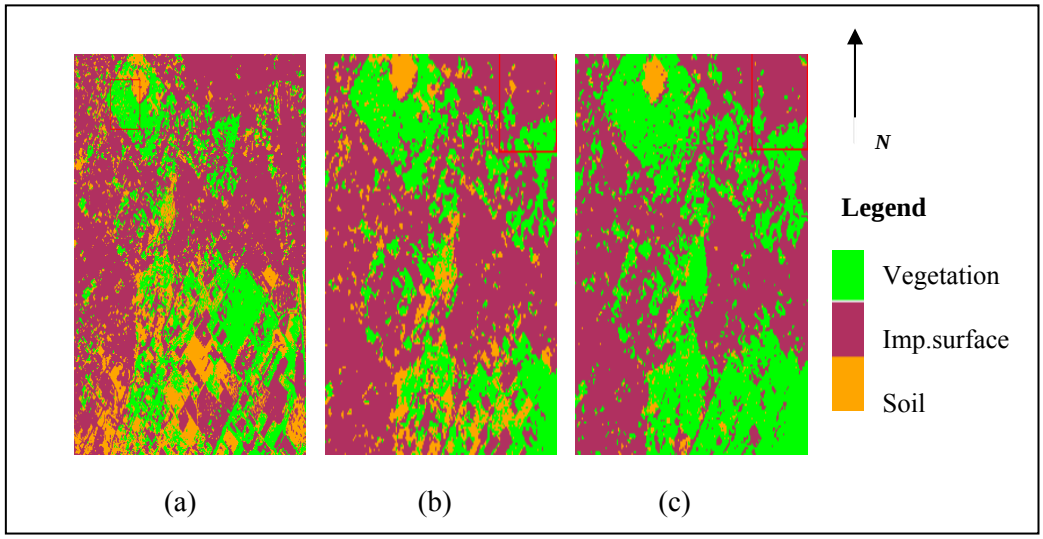

Fig 3.9 Maximum Likelihood Classification results for the IKONOS image (a) for ASTER (VNIR) (b) for ASTER (SWIR) (c) for Landsat images.

The resulting reference maps are shown in fig 3.9. Although the training pixels for the classes were selected carefully it should be mentioned that considerable amount of pixels can be misclassified in the reference image. The problem mainly lies in the assumption that each pixel contains one pure land cover class with homogeneous reflectance across it. With the high spatial resolution (4m) of the IKONOS image it can be assumed to overcome this problem, since within a 4mx4m area on the ground it is highly possible to have more homogeneous single land cover component even in an urban environment. Each reference image was generated from the training samples selected on the respective coarse spatial resolution image. The MLC classification considers these training data statistics for each class in respective band to be normally distributed, so the training data with bi-or-trimodal histograms in a single band is not ideal. The classification accuracies of these reference maps were conducted in the ENVI software by generating 100 random points as ground truth on the image. The overall accuracy and kappa coefficients in IKONOS reference map for ASTER and Landsat images are shown in table 3.7.

Table 3.7 Accuracy statistics for the reference images

Reference Image (IKONOS)	Overall Accuracy%	Kappa Coefficient
Reference image for ASTER (VNIR)	90.72	0.845
Reference image for ASTER (SWIR)	87.46	0.792
Reference image for Landsat	80.83	0.679

These accuracy statistics for each reference image shows satisfactory results with the average kappa values and overall accuracy in the range of 0.7 and 80% respectively. These images were transferred to R statistical software package as matrices for the further analysis.

According to the work of P.M.Atkinson [22], it has been shown that the hard maximum likelihood classification can be used to produce known class fractions as the reference. This has been implemented in this study for the preparation of the validation data set. Each of these reference data sets (with hard MLC) were turned into images representing fractions of each class, which is further discussed in Chapter 5. This conversion was carried out using the R software (see section 3.9).

3.9. The R software

All the major implementations of the techniques discussed were carried out using the R programming language and environment for statistical computing version 2.5.0 software. R is an open-source software which can be used for the statistical computing and visualization. It is based on the S language developed previously. R is basically a well developed programming language, which supports input and outputs of the images as matrices; conditional loops and user define functions. Its faceable graphical capabilities support most of the image analysis tasks. In this study, the MRF based SRM technique with simulated annealing was implemented using the R programming language. It has also been used to generate the fraction maps from the maximum likelihood classification results and the SRM results. Finally, all the accuracy assessments and validations were carried out using this programming environment.

4. MRF-based SRM technique

4.1. Introduction

MRF have been used by statistical physicists to explain various phenomena occurring among neighbouring particles because of their ability to describe local interaction between them. MRF model has also been used to explain why intensity values of adjacent pixels of an image are more likely to be same than different values. There are large number of problems that can be modelled using the MRF models [13].

In interpretation of a scene, contextual information might be very useful. By considering the pixel in context with other measurements more complete information might be derived and the suitable use of context allow the elimination of possible ambiguities, the recovery of missing information and correction of errors. Context can be defined in three dimensions; the spectral, spatial and temporal dimensions [36]. The spectral dimension can be defined as the different bands of the electromagnetic spectra. In a pixel labelling problem, spatial context refers to the correlation between the class labels of neighbouring pixels.

In statistical image classification the Bayesian theory has a profound influence. And Bayesian classification formulae depend on two key elements the prior and conditional probability density functions (p.d.f). However the use of context to model these prior (as image pixels are assumed conditionally independent in MRF) probability in order to help in the interpretation of remotely sensed imagery is considered to be a reasonable procedure [36]. When using the concept of context, pixels are not treated in isolation, but are considered to have a relation with their neighbours. Thus the relation ship between pixels of interest and its neighbours are treated as being statistically dependent. MRF models have a flexible framework for the combination of the contextual information from neighbouring pixels and the spectral information from the image data. So it has been used to model the images.

In this chapter we describe how MRF theory can be used to model this p.d.f of context dependent patterns and the development of the methodology of this study to implement it in real data with certain modifications from its previous applications as mentioned in Chapter 2. The effectiveness of this method will be analyzed with respect to the linear unmixing technique finally.

4.2. The maximum a posterior probability (MAP)

In statistical or Bayesian rules, the decision making is based on the concept of the maximum a posterior (MAP) probability [36,37]. And it has been the most popular choice in MRF vision modelling [8]. The Bayes theorem which converts the prior probability to a posterior probability takes a form as below.

$$p(c \mid y, M_w) = \frac{p(c)\, p(y \mid M_w)}{p(y)} \tag{4.1}$$

Where $p(c)$ is the prior probability that the given pattern belong to class c, $y = \{y_1, y_2, ..., y_I\}$ is a set of observations, I is the number of observations, $p(y \mid M_w)$ is the conditional probability of the observation set y for a given model M_w, $p(y)$ is the probability of the observation set y and $p(c \mid y, M_w)$ is the probability that the pattern belongs to class c for the observation set and model. This is the posterior probability. Since $p(y)$ is not related to any class, we can write the eq (4.1) as follows:

$$p(c \mid y, M_w) \propto p(c)\, p(y \mid M_w) \qquad (4.2)$$

The classification decision can be made by

$$c' = \arg\max_{c} \{ p(c)\, p(y \mid M_w) \} \qquad (4.3)$$

Where c' is the estimated pattern class. If $p(c)$ is unknown, it is set to constant and the MAP estimation becomes a maximum likelihood (ML) estimation.

4.3. Mathematical concepts in MRF based SRM

Let y be a coarse resolution multispectral remote sensing image containing K spectral bands. The pixel locations are denoted as $b_i \in B$, where B is the set of pixels with size $M \times N$. Spatial resolution of the image is denoted with the pixel size R, so that every pixel b_i is assumed to correspond with a square area on the ground of size R^2. The resulting super resolution map is a classified map which is denoted by c and defined on a set of pixels A.The area the pixels in A covers is as the same as B,but bears a high spatial resolution which is denoted by a lower pixel size of r. The original image with the pixel size of R will be referred to as coarse resolution image and the super resolution map with pixel size r will be referred as the fine resolution image.

The scale factor of the super resolution map is denoted as S which is the ratio between the coarse and fine resolution pixel sizes and can be denoted as $S = R/r$. This means each pixel b_i will contain S^2 fine resolution pixels of $a_{j/i}$ or a_j. There for the pixel matrix A will have the dimensions of $(SM) \times (SN)$ pixels. Thus the number of pixels belonging to A will be S^2 times the number of pixels in set B.

Assuming a multispectral image x having the same spectral bands as y as well as the spatial resolution of r, image y can be seen as a degraded version of x. Image y however is measured by satellites or other measuring equipment, while image x is not. Furthermore it is assumed that every pixel in image x can be assigned to a unique class $c(a_j) = \alpha$, where $\alpha \in \{1, 2, ..., L\}$. For

convenience the class of pixel a_j will be referred to as c_j. The relation established between images y and x can be described by:

$$y(b_i) = \frac{1}{S^2} \sum_j x(a_{j/i}) \tag{4.4}$$

For each pixel a_j in A a symmetric neighbourhood $N_j = N(a_j)$ can be defined. Where N_j is a set of pixels neighbouring pixel a_j. In this neighbourhood system a pixel cannot be neighbour to itself and the neighbouring relationship is mutual [11]. A set of pixels inside a square window, excluding the pixel a_j at the centre of the window and with the window size W being the length of one side, defines the complete neighbourhood. Here neighbourhoods are defined with there order, and first and second order neighbourhood systems are used commonly. As seen in figure 4.1 a window size of W=3 defines a second order neighbourhood while a window size of W= 5 defines a fifth order neighbourhood. Higher order neighbouring systems can be grown in a similar manner.

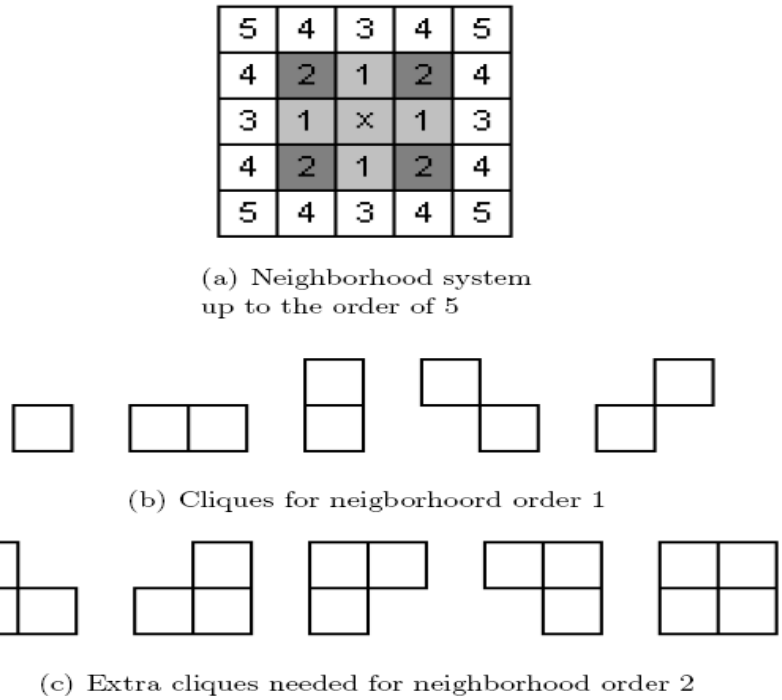

Fig 4.1 Neighbourhoods and the definition of cliques

According to the figure above the first order neighbours for a pixel $a = (i, j)$ is denoted by $N(i, j) = \{(i-1, j), (i+1, j), (i, j-1), (i, j+1)\}$ which shares the sides with x. And similarly the second order neighbours are the four pixels having corner boundaries with the pixel of interest [36]. A clique is defined as a subset of this in which all pair of pixels are mutual neighbours. It can be a single site, or a pair of neighbouring site, or a triple of neighbouring sites depending on the growth of the neighbouring order. The size of the window also determines the amount of cliques which can fit inside as neighbourhood. The contextual constraints introduced from the neighbouring pixels will be modelled by the means of prior energy. In SRM the neighbourhood order should increase in relation to the scale factor (S). This will include all the sub-pixels present within the coarse pixel in the

neighbourhood system. As a result the Markovian property within the neighbouring sub-pixels will be preserved.

In this study the minimum neighbourhood order considered is second order with respect to the scale factors used. To implement this growth of the neighbourhood size in relation to the scale factor a relationship between S and the window size W has been developed as $W = S - 1$. Under the given window size the number of maximal pixel neighbours (Nn) to be considered is also realized by $Nn = ((W \times 2) + 1)^2 - 1$. In case for a scale factor of $S = 3$ the number of maximal pixel neighbours to be considered is 24, which makes a window size of 5.

4.3.1. Proposed approach for the study

According to the concepts of MRF discussed in section 4.3 a methodology has been developed and executed for the generation of SRM. The approach was first applied to the IKONOS images and the efficiency of the process was analyzed (see Chapter5). The proposed approach is mainly consisting of two major steps, the initial SRM generation and the optimization of the SRM. And the generation of fractions for the final analysis for the comparison with the Hyperion fractions.

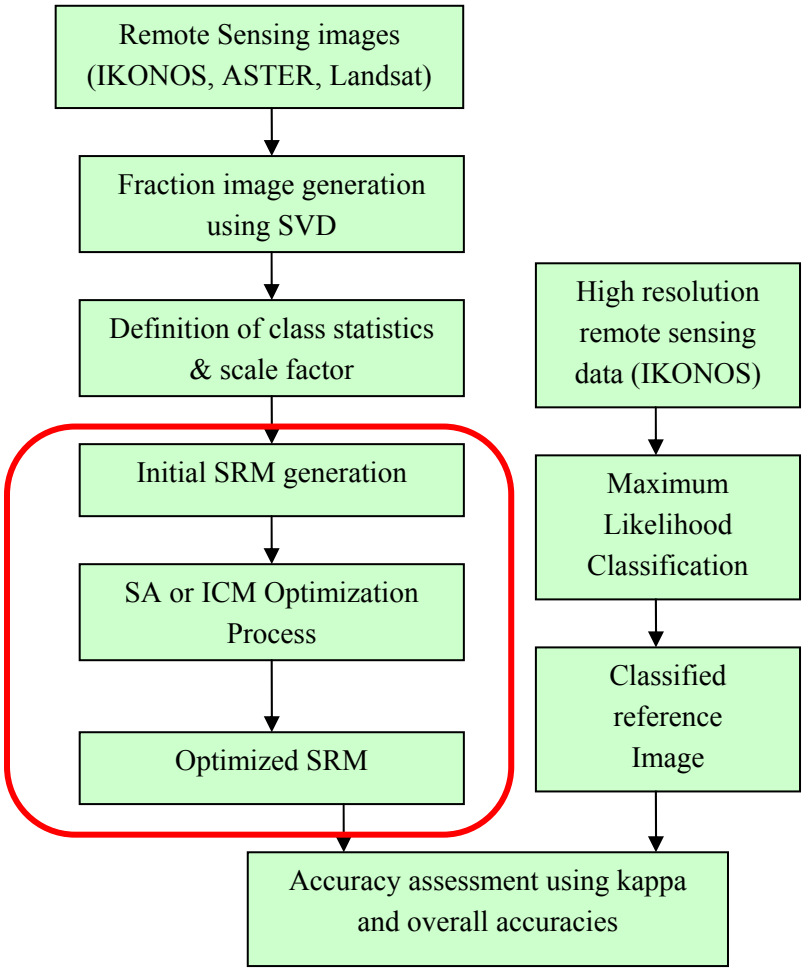

Cont…

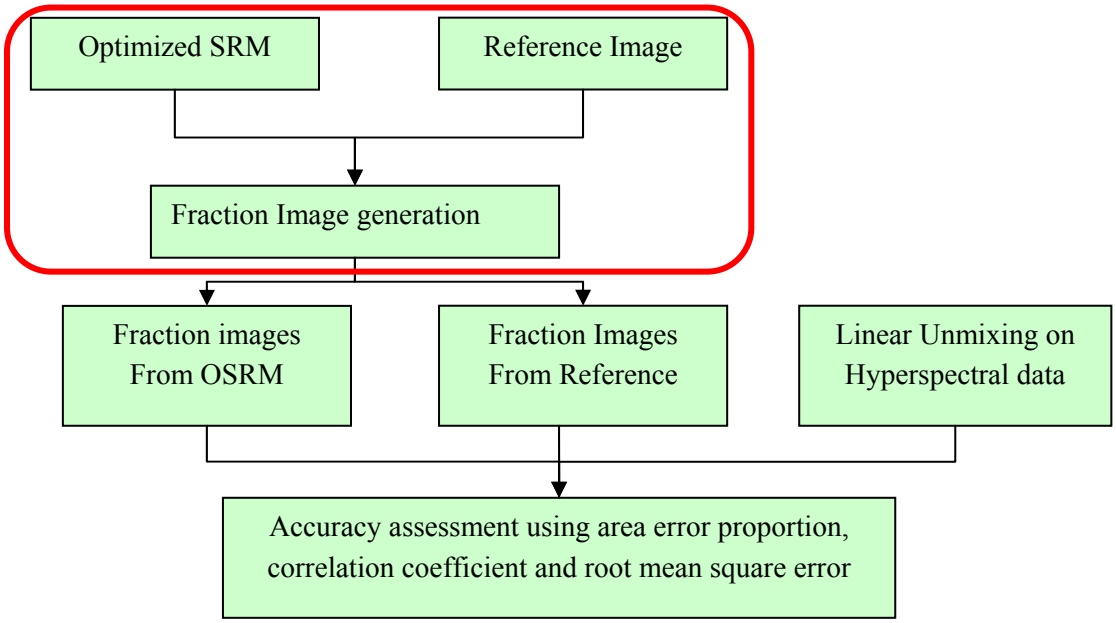

Fig 4.2 The overall approach for the SRM generation and the validation of the results

Above figure (fig 4.2) delineate the overall methodology adopted for the study. According to this the IKONOS, ASTER and Landsat images will be going through the MRF based SRM technique to produce super resolution land cover maps and the optimal parameters required for each image will be determined according to the accuracy of the STM. These maps will be converted to fraction images representing each land cover class to be compared with the linear unmixing fractions of the Hyperion image.

4.3.2. Initial SRM generation

In the first step the fraction image produced by SVD is the input for the initial SRM generation. Each pixel was divided by S to get the sub-pixels, and then each pixel was randomly labelled with the corresponding classes from the coarse fraction image. The classes were defined by there mean vectors and covariance matrices. Prior to that the separability of these classes defined on the course spatial resolution image was assessed using the TD and JM. The parameters related to Gibbs potential function as discussed in section 4.4 were also estimated. The Gibbs potential function will have low values in the case of high spatial resolution images, due to more number of pure pixels leading to neighbouring pixels occupying the same class. The number of subpixels allocated to the given class for the initial SRM can be expressed as $n = \theta_{bi} \times S^2$, where θ_{bi} is the proportion of a given class in pixel b_i of the coarse resolution image. Thus; n number of sub-pixels will be randomly labelled within the original pixel y_i with respect to this class proportions. The mean and covariance matrices were defined by carefully selecting pure training pixels for the desired land cover classes from the coarse resolution image. And fractions for each land cover class in pixel b_i is defined by SVD. The output of this initial step is an initial SRM with many isolated pixels. This should be optimized considering the spatial dependence between the pixels, to get the optimized SRM with more contextually smoothed classes.

4.3.3. Optimization of the initial SRM

In the second step the initial SRM is optimized to yield the optimized SRM. The optimization process is based on the simulated annealing (SA) algorithm, which is described in depth in section 4.4.1. Here the simulated annealing algorithm iteratively refines the initial SRM by updating each pixel with the new class label to accurately characterize the spatial dependence between the class proportions of the neighbouring pixels. Simulated annealing is controlled by the annealing parameters; the initial temperature T_0 and the updating schedule T_{upd} (see section 4.4.1). These parameters were estimated prior to the execution of the algorithm. The prior $(U(c))$ and likelihood $(U(c \mid y))$ energy functions were defined to introduce both contextual constraint and spectral information. These two energy functions were combined to define a global energy (U_{global}) function. The smoothening parameter (λ) was introduced as a balancing factor between these two constraints. The pixel labelling was carried out by minimizing the energy function which was equivalent to maximizing the probability of the labelling. Thus a pixel value corresponding to a lower energy value had higher likelihood of being generated than the one with a higher energy value.

4.4. MRF and Gibbs distribution

In order to proceed further, we hope to continue the discussion we had in section 4.3 with the theoretical back ground of MRF.

The observed coarse spatial resolution multi spectral image y, is represented in vector form as $y(b_j) \in \mathrm{R}^k$ for a pixel b_j where R denotes the set of real numbers representing the intensity values and k for the number of spectral bands. Let $A^j = \{a_1{}^j, ..., a_{s^2}{}^j\}$ represent the set of pixels in the set A, that corresponds to the same area as the pixel b_j in set B. As a resulting SRM pixel is pure and can represent only by one land cover class its value $c(a_j)$ or c_j can only take an integer value that corresponds to a particular land cover class at pixel a_j in the actual scene. Hence $c(a_j) = \alpha = \{1, ...L\}$, as shown earlier in section 4.3. A markov random field is a random field which shows the following properties with respect to its neighbourhood system:

- *Positivity*: $p(c_j) > 0$, this states that the joint probability $p(c_j)$ of any random field is uniquely determined by its local conditional probabilities.

- *Homogeneity*: This specifies the conditional probability for the label of a pixel, given the label of the neighbourhood pixel, regardless of the relative location of the pixel.

- *Markovianity*: This shows that labelling of the pixel is only dependent on its neighbouring pixels. That is, the conditional probability of the value of a pixel given pixel values of the entire image excluding the pixel of interest is equal to the conditional probability of a value of a pixel given values of its neighbouring pixels. This can be expressed in mathematical terms as below.

$$p(c_j \mid c_{C-j}) = p(c_j \mid c_{N_j}) \tag{4.5}$$

Where c_{C-j} refers to all the classes except the class at j, and c_{N_j} refers to the classes neighbouring the class at j. This means the class at j, c_j depends on the classes at the sites neighbouring j, $N(c_j)$. In the context of land cover classification this property implies that same land cover class is more likely to occur in connected regions than isolated pixels [22]. The MRF model characterizes the spatial dependence among neighbouring sites; however a direct implementation of (4.5) is not simple because the probabilities can take up any values. As a result we introduce GRF.

When the above properties are satisfied the MRF is equivalent with the Gibbs Random Field (GRF), because according to Hammersley-Clifford theorem a GRF exist for every MRF as long as the GRF defined in terms of cliques on a neighbourhood system [36]. A MRF is defined in terms of local properties, i.e. a label assigned to a pixel is affected only by its neighbours, whereas a GRF describes the global properties of an image, which is the label given to a pixel is affected by the labels given to all other pixels in the image.

Therefore the posterior probability for each class c given the observed image y can be specified by the means of a posterior energy function.

$$p(c \mid y) = \frac{1}{Z}\exp\left(\frac{-U(c \mid y)}{T}\right) \tag{4.6}$$

Where

$$Z = \sum \exp\left(\frac{-U(c \mid y)}{T}\right) \tag{4.7}$$

Where Z is the normalizing constant and T is a constant termed temperature. Here we can define an energy function $U(c \mid y)$. From equation (4.6) we can say that maximizing $p(c \mid y)$ is equivalent to minimizing the energy function which can be formulated as:

$$U(c) = \sum_{c \in C} V_C(c) \tag{4.8}$$

$V_C(c)$, is the Gibbs potential function with respect to clique C, of all the available cliques in the neighbourhood. In this study we stick to pairwise cliques only, they are the vertical, horizontal, left-diagonal and right-diagonal pairs. And the single site clique was not considered, because the probability of each class was considered to be same and thus set to 0 as in most applications [36].

And the prior probability can be expressed as:

$$p(c) = \frac{1}{Z}\exp\left(-\frac{U(c)}{T}\right) \tag{4.9}$$

So with the Gibbs parameters as the prior information and V_2 the pairwise clique potential, equation (4.8) can also be expressed for prior energy as:

$$U(c) = \sum_{j,i}\sum_{l\in N_j} V_2(c_j, c_l) \tag{4.10}$$

Low values of the Gibbs potential function corresponds to similar values whereas high values corresponds to dissimilar values of a clique. Further explained by the model (Bremaud, 1999 and Winkler, 1995) [23] given by.

$$V_{\{j,l\}}(c) = \begin{Bmatrix} -\beta; if\ \ c_j = c_l\ \ and\ \ l \in N_j \\ +\beta; if\ \ c_j \neq c_l\ \ and\ \ l \in N_j \\ 0; l \notin N_j \end{Bmatrix} \tag{4.11}$$

This model justifies the phenomena exists in the class distribution of a SRM, that is the classes occupying the neighbouring pixels are likely to be the same. So in the study to maximize the posterior energy function, when a pixel belong to the same class as the class of the pixel in focus it was given a value 0 and 1 otherwise, and they were weighted with respect to the Euclidian distance, this is discussed below.

According to the equation (4.6) to allocate pixel a_j to class α ,the posterior probability has to be minimized. As described in equation (4.3) a MAP solution can be incorporated for this.

$$c_j = \arg\max\{p(c \mid y)\}$$

Using the Bayes rule:

$$P(c \mid y) = \frac{p(y \mid c)\, p(c)}{p(y)}$$

And the likelihood probability, which is the conditional distribution of the observed data y given the class c assumed as a Gaussian distribution and defined as:

$$p(y|c)=\frac{1}{\sqrt{2\pi^{\rho}}\sqrt{|\sum_{\alpha}|}}\exp(-U(y|c))$$

Where ρ is the dimensionality of the feature space, for example the number of image bands, $\sum_{\alpha}$ is the class-conditional covariance matrix for class α.

The likelihood energy can be defined by using the mean vector μ_{α} of class α and the covariance matrix, by the following equation:

$$U(c|y)=\sum_{i}\frac{1}{2}(y(b_i)-\mu_{\alpha})^{T}\sum_{\alpha}^{-1}(y(b_i)-\mu_{\alpha})+\frac{1}{2}\ln\det\sum_{\alpha} \quad (4.12)$$

Here T denotes the transpose of a matrix and $\sum_{\alpha}^{-1}$ is the inverse of the covariance matrix. As S^2 pixels in the SRM correspond to one pixel in the coarse spatial resolution image (y), the p.d.f of an observed vector b_i is also assumed normally distributed with mean vector and covariance matrix given by,

$$\sum_{i}=\sum(y(b_i))=\sum_{\alpha=1}^{L}\theta_{\alpha}(b_i)\sum_{\alpha}$$

$$\mu_i=\mu(y(b_i))=\sum_{\alpha=1}^{L}\theta_{\alpha}(b_i)\mu_{\alpha}$$

Where θ_{α} is the proportion of land cover class α in pixel $y(b_i)$. And a class can be assigned to a pixel when prior $p(c)$ and posterior $p(c|y)$ probabilities are maximized. This is equivalent to minimizing the energy functions:

$$c_j=\arg\min\{U(c)+U(c|y)\} \quad (4.13)$$

The likelihood energy in equation (4.12) depends on the Mahalanobis distance of the pixels and the prior energy in equation (4.9) depends on the pairwise clique's V_2. For the pairwise clique potential function *Kassaye* [11] used the following equation:

$$V_2(c_j,c_l)=\omega(a_l)\delta(c_j,c_l) \quad (4.14)$$

Where $\omega(a_l)$ is the weight function. In this study an extra term is added to normalize the weight function, so the prior energy lies between 0 and 1 and it takes the form of:

$$V_2(c_j, c_l) = \frac{1}{\sum_{l \in N_j} \omega(a_l)} . \omega(a_l) \delta(c_j, c_l) \tag{4.15}$$

Where $\delta(c_j, c_l)$ takes the value 1 if $c_l \neq c_j$ and 0 otherwise. The weight function is made to stay inversely proportional to the square of the distance $d(a_j, a_l)$ between pixel a_j and a_l and described in mathematical form as:

$$\omega(a_l) = \frac{1}{Nn_j . d(a_j, a_l)^2} \tag{4.16}$$

Where Nn_j is the amount of pixels in the neighbourhood for the pixel j.

Since it is assumed that a pixel at coarse spatial resolution comprises of a number of pure pixels at fine spatial resolution and the observation of any distinct pixels at fine spatial resolution are independent, statistical mean vector and covariance matrix of observed data at a given pixel at coarse spatial resolution are directional sum of mean vectors and covariance matrices of corresponding pixels at fine spatial resolution, respectively [24]. Hence, the p.d.f of the observed image can be stated as:

$$p(y \mid c) = \prod_{b \in B} p(y(b) \mid \theta(b)) = \prod_{b \in B} \frac{1}{(2\pi)^{\rho/2} \sqrt{|\det(\sum_b)}} \exp\left[-\frac{1}{2} (y(b) - \mu(b))^T \sum_b{}^{-1} (y(a) - \mu(a)) \right] \tag{4.17}$$

Where $\theta(b) = [\theta_1(b), \ldots\ldots \theta_L(b)]^T$. Maximizing the equation (4.17) directly yields the maximum likelihood estimation (MLE) of a. However the MLE of a does not utilize the connectivity property of the SRM given in equation (4.6) [24].

For the equation (4.13) a special parameter λ, the smoothening parameter has been used. This controls the balance between the two energy functions. In previous studies this parameter was only used to control the prior energy, which result in optimal λ in between 0 and ∞.Here we normalize this parameter between 0 and 1:

$$c_j = \arg \min \{ \lambda U(c) + (1 - \lambda) U(c \mid y) \} \tag{4.18}$$

This equation should be minimized to find the most reasonable class for the pixel a_j. For this minimization here we use the simulated annealing algorithm which has been proven to perform with good results over the other search approach techniques such as Iterated Condition Mode (ICM), Maximum a Posterior Margin (MPM).

4.4.1. Simulated Annealing algorithm

The concept of SA is based on the manner in which liquids freeze or metals recrystalize. The process which is initially holding a high temperature and in a disordered stage, is slowly cooled and become more ordered as it approaches the frozen state with the cooling proceeds. Once the global energy constructed and the smoothness parameters have been determined, as the next step we start the pixel labelling. As discussed earlier in section 4.2 we use the MAP estimation for this. To find the MAP solution we adopt the SA algorithm in this study.

SA generates a sequence of $\{c_p\}_p = 1,2,3,.....$ using a random number generator where p denotes the iteration number. The p.d.f of a proposed state c_{p+1} depends on the current state c_p, observed data set y and the temperature parameter. SA algorithm allows the randomness (T),to decrease in an iterative way that the best solution for equation (4.16) can be made. This can be shown in pseudo code as follows:

```
initialize T,c;
repeat
        repeat
                generate c_j' ÎN_j;
                δE = E(c_j') - E(c_j);
                Q = min(1, exp(-δE / T));
                if random[0,1] < Q then c_j = c_j';
                decrease T;
        until equilibrium;
until T = 0;
return c;
```

Here $E(c)$ is defined as

$$E(c) = \lambda U(c) + (1-\lambda) U(c \mid y) \tag{4.19}$$

Within every step a c' is randomly chosen from the neighbours N_i. The difference of both energies, using equation (4.19) is calculated. Variable Q holds the evaluation of the equation $\exp\frac{-\delta E}{T}$ or 1, which ever is minimum. If the random value from the uniform distribution in [0, 1] is lower than Q, c will receive the value c'. That is it generates a new label c_j' for each pixel c_j based on prior and conditional energies. The Metropolis algorithm in the most nested repeat block, is tend to converge to equilibrium at the current temperature T .When equilibrium is reached ,the temperature T will be decreased according to the criterion called cooling schedule. The process is repeated until the system

becomes frozen $(T \to 0)$, that means pixels stop updating. The outer repeat block is known as simulated annealing algorithm. The cooling schedule associated with this study can be expressed as:

$$T(t) = T_0 \times T_{upd} \tag{4.20}$$

Where $T(t)$ is any next temperature value depending on the t^{th} iteration. As explained earlier in section 4.3.3 these values are determined first. According to *Kassaye* [11] results, the value for the updating schedule (T_{upd}) typically in the range of 0.8 to 0.99. So for this research we have incorporated a value of 0.9 for T_{upd}. The initial temperature T_0 use to control the randomness of the optimization algorithm ($T_0 \propto$ Randomness). A large number of pixels having different values indicate a high degree of randomness of the SA algorithm. So a high temperature can increase the probability of a pixel being replaced by a new class label though the energy of a new class is higher. Due to these reasons and according to previous studies [11,24,38,39,40,41] a value in the range of 2.0 to 3.0 does suffice the parameter T_0. Here we incorporate 3.0 for the initial temperature. The updating process for the new temperature value (equation 4.18) is controlled by two constraints, if the number of pixels that have a different value after one updating is less than a predefined value, minimum activation threshold (*min_acc_thr*) or by keeping the counter with in a limit defined by the variable called, number of iterations (*Niter*). The pixel updating was performed by a row wise visiting scheme, which determines the order of the pixels in the SRM for the updating. The SRM will gradually change reducing the number of isolated pixels. The Gibbs potential function will force the SA algorithm to iteratively generate a SRM which is close to the solution of the MAP criterion in equation (4.3), as the desired SRM. One of the major drawbacks of this algorithm is the convergence occur when number of iterations approaches infinity. The SRM was then turned into contextually refined fraction images, with higher classification accuracy than the initial subpixel classification.

4.5. Measures of accuracy

In order to assess the level of agreement between labels assigned by the classifier and the reference data several measures of accuracies have been used in this study. The generated SRM was tested for the fitness of use with respect to the reference image with the use of a confusion matrix. The confusion matrix compares these two images for a class-by-class agreement. Two measures of accuracy the overall accuracy (OA) and the Kappa coefficient (K) derived by the confusion matrix has been used for the assessment of the SRM in this study. They are defined as:

$$OA = \frac{1}{N} \sum_{i=1}^{r} c_{ii}$$

Where N is the total number of pixels in the image, r denotes the number of rows and columns in the confusion matrix and c_{ii} is the number of correctly classified pixels for each class.

$$\mathrm{K} = \frac{N \sum_{i=1}^{r} c_{ii} - \sum_{i=1}^{r} (c_{i+}.c_{j+})}{N^2 - \sum_{i=1}^{r} (c_{i+}.c_{j+})}$$

Where c_{i+} and c_{j+} are the marginal total of row i and j respectively. The K uses the information from the whole error matrix, and because of this advantage it has been used with OA as initial accuracy measures for the optimized SRM.

Three other measures of accuracy the Correlation Coefficient (CC), Root Mean Square Error (RMSE) and the Area Error Proportion (AEP), has been incorporated in the study to evaluate the agreement between the fraction Images generated from the linear unmixing and SRM technique, with the reference fraction image. Let us take a set of known or target proportions as Y and the set of estimated proportions as A, let n be the total number of pixels. Here Y represents the values coming from the reference image and A represent the values coming from the images from SRM or the linear unmixing.

The CC represents an alternative measure of the amount of association between target and estimated proportions. It indicates the strength and direction of a linear relationship between the two variables. And can be expressed as:

$$\mathrm{CC} = \frac{C_{Yj.Aj}}{S_{Yj}.S_{Aj}}$$

Where $C_{Yj.Aj}$ is the covariance between Y and A for class j and S_{yj} and S_{Aj} are the slandered deviations of Y and A for class j represented as:

$$C_{Yj.Aj} = \frac{\sum_{i=1}^{n} (\overline{Y_j} - Y_{ij}).(\overline{A_j} - A_{ij})}{n-1} \quad \text{And} \quad S_{Yj} = \sqrt{\frac{1}{n-1} \sum_{i=1}^{n} (Y_i - \overline{Y})^2}$$

In this study CC provides us the information about the precision of the sub-pixel spatial distribution [10,26]. The correlation is defined only if both the standard deviations are finite and both of them are nonzero. The CC will be 1 for an increasing linear relation ship and -1 for a decreasing linear relation.

The RMSE describe the accuracy including both random and systematic errors. Here it is used to acquire the information about the accuracy of the prediction that is the biasness, and also the precision [9,41,44]. And it can be represented as:

$$RMSE=\sqrt{\frac{\sum_{i=1}^{n}(Y_{ij}-A_{ij})^2}{n}}$$

One of the simplest measures of agreement is the AEP. As it is based solely on the area predictions; it represents a measure of the success of the proportion constraint in maintaining the target proportion. And AEP can be represented as:

$$AEP_j = \frac{\sum_{i=1}^{n}(y_{ij}-A_{ij})}{n}$$

These measures play a major role in this study. The analysis of the effectiveness of the SRM and the linear unmixing technique is critically explored by this measure.

5. Results and discussion

This chapter presents the experimental results obtained during the process and the analysis of it. Section 5.1 discuses the results of linear unmixing on Hyperion data. Section 5.2 shows the experimental results on IKONOS data. Section 5.3 and 5.4 presents the experimental results on ASTER VNIR and SWIR images respectively. And finally the findings on the Landsat image will be discussed on section 5.5.

5.1. Spectral unmixing results for the Hyperion data

In this section we present the results obtained from the linear unmixing process over the Hyperion data. After the pre-processing steps the Region of Interests (ROI) created for the endmembers were entered into the unmixing classification function to perform a constrained unmixing. After the examination of the abundance images with RMSE value final selection of the fraction images were carried out. The resulting images for the V-I-S classes have been shown below.

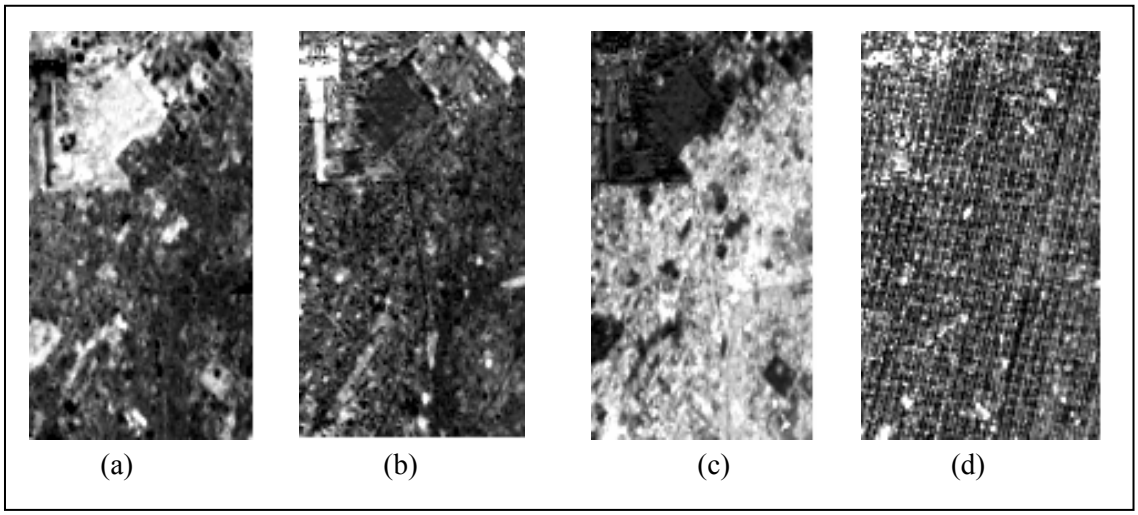

Fig 5.1 Endmember abundance images from linear unmixing (a) Vegetation (b) Soil (c) Impervious (d) Error image showing RMSE

The output of the spectral unmixing includes RMSE and endmember abundance images. The endmember abundance images derived from the unmixing analysis should posses a value between 0 and 1. Sometimes the fraction proportion may have values more than 1 or less than 0 due to several reasons- that the pixel is purer than the selected endmember, variability in the selected classes, non-linearity of mixing etc. Due to the broader class definitions involved in this study, the representative endmembers for these classes (V-I-S) may not be the most pure pixels in the image. Highly positive and negative values corresponds to the areas having high RMSE values (Figer.5.1 (d)).The error images shows the distribution of these errors. Statistics for these unmixing results are shown in the table below.

Table 5.1 Statistics of fractional abundances and RMSE images obtained through the unmixing

Class	*Min*	*Mean*	*Max*	*<0%*	*>1%*	*Stdv*
Vegetation	-0.913	0.500	1.362	38.190	0.305	0.283
Soil	-0.990	0.176	1.365	12.020	0.532	0.193
Impervious	-0.524	0.466	2.200	13.540	3.093	0.346
RMSE	0.000	0.141	1.000	0.0450	0.007	0.071

According to these results, the mean abundance of the endmembers derived from the Hyperion data shows a positive value. And the low standard deviation shows the acceptable deviation from the mean. Next the minimum and maximum abundances for vegetation and soil are more likely to be the same. But for vegetation the percentage of pixels having values less than 0 is 38.19%.This is mainly due to the different types of vegetation in the area an the chosen endmembers are not capable of representing all this vegetation types. Impervious surface class shows a higher maximum abundance value than the other classes. But the percentage of pixels representing this high values is in the range of 3.09%, which make the results justifiable for the use. Overall results indicate the validity of the results for the further analysis. And for this study these results has been accepted to be good enough. Detailed figures and statistical reports of the linear unmixing process for the Hyperion image are given in Appendix-A (fig A.1).

5.2. Experimental results for the IKONOS degradation image

To understand the efficiency of the MRF based SRM technique first it was applied on a degraded IKONOS image which holds a spatial resolution of 16m (section 3.5.1). By doing so temporal effects and the co-registration errors will be stopped effecting the accuracy assessment. Here the degraded IKONOS image pixel is made to have a value, which is the mean of 4x4 pixels in the fine resolution image (IKONOS 4m multispectral image). This makes the degraded image high in mixed pixels making it one of the best inputs for the MRF based SRM technique. In order to overcome the lengthy processing time a subset of the image with 60x60 pixels were chosen for this. Selected subset of the IKONOS image with there feature space plots are shown in the figures below.

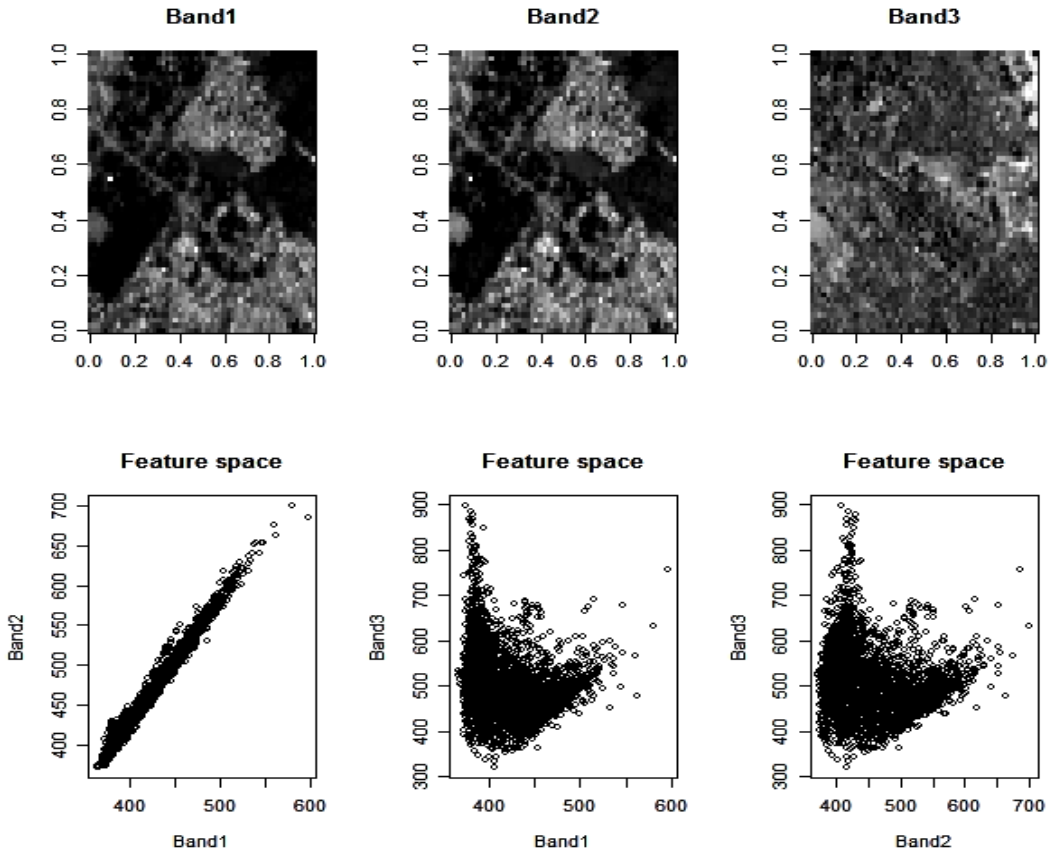

Fig 5.2 Degraded IKONOS multispectral image with feature space plot

The scale factor was set to $S = 4$. This S value defines a neighbourhood by a 7x7 square window. According to Kassaye [11] for a successful optimization of the SRM the initial temperature (T_0) should be set to 2 or 3. This finding justified the findings of the earlier studies of Geman and Geman [21] and Kasetkasem [23]. Due to this in this study T_0 was set to $T_0 = 3$. For the updating schedule T_{upd} Kassaye [11] suggested two values 0.8 and 0.9 for a low complex and a highly complex scene respectively. As the study deals with a highly complex urban scene we chose the T_{upd} value accordingly for 0.9.

Mean vector and the covariance information for the V-I-S classes were defined by the selected pure training pixels representing each of these classes from the original IKONOS image. The classes defined were well separated with TD values in the range of 1.9 to 2.0 (see Appendix-A, figA.3 to fig A.5 and tableA.1 to table A.3 for details). Good class separability leads to a higher spectral distance between the class means which can make the prior constraint provide more information for the pixels to be classified correctly. This may yield the prior constraint getting a very similar weight as for the likelihood constraint, which can refine the classification on the basis of contextual information. This also provides a prior condition for the testing of the SRM technique.

5.2.1. Optimal smoothness parameter estimation

In this study the use of smoothness parameter has being changed from its previous ones (see eq.4.18). Here the smoothness parameter (λ) controls the balance between the prior and the likelihood energies in the global energy (see eq.4.16). The rationale for introducing smoothness assumption is that image properties in a neighbourhood shows some coherence and generally do not change abruptly [11]. The λ value controls the smoothness and it assures the pixels to be labelled according to the majority of the pixels in the neighbourhood. This is an important aspect in a heterogeneous urban scene, where the spatial variability increases rapidly. To achieve a successful optimization, by controlling the over smoothening and maximizing the spatial correlation between neighbouring subpixel, setting of an appropriate smoothening parameter is very important.

The algorithm was executed with different λ values (Λ), and the Kappa coefficient (K) and the overall accuracy (OA) were tested and the results were summarized in the table 5.2 below. The resulting plots are shown in figure 5.3.

Table 5.2 Overall accuracies and the Kappa coefficients for the degraded IKONOS image

Λ (λ)	OA (%)	Initial K	K
0.1	70.310	0.2813	0.4610
0.25	72.828	0.2813	0.5041
0.3	72.939	0.2813	0.5075
0.35	73.003	0.2813	0.5114
0.4	72.008	0.2813	0.5084
0.45	56.590	0.2813	0.3491
0.85	14.736	0.2813	0.0002

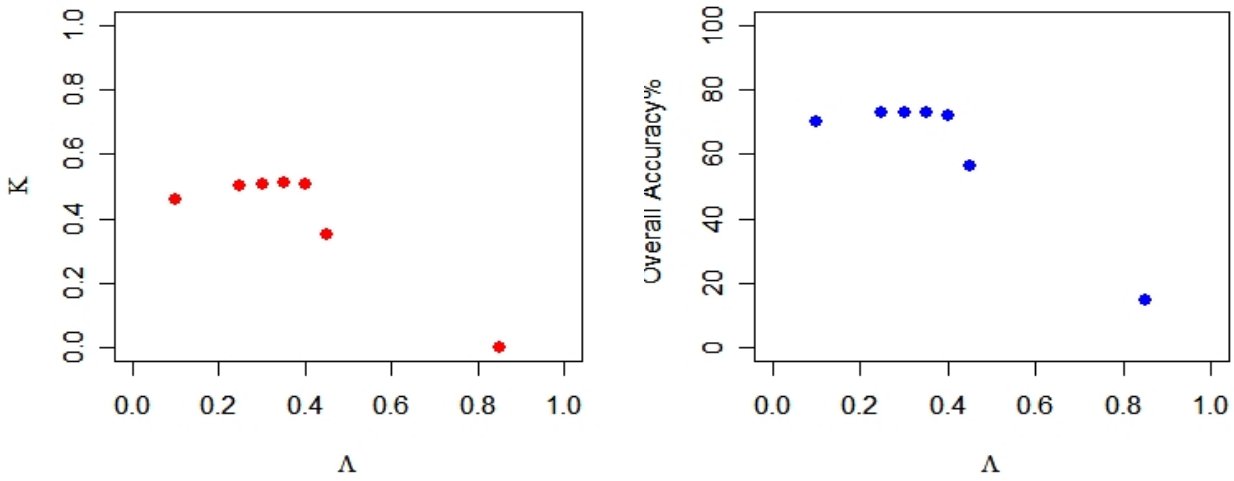

Fig 5.3 The effect of smoothness parameter (λ) by K and OA respectively.

The graph shows the effect of $\lambda(\Lambda)$ on the quality of the SRM. Resulting K values increases with the increase of the λ values and it reach a unique optimal value of 0.35 where K =0.5114. An abrupt

drop in the K values can be seen for the value of λ from 0.4 to 0.45. Beyond this the K values started dropping steadily. This drop shows that at the range starting from 0.45 to 1 for the λ values it starts giving lower weight to the likelihood energy than the prior energy. Therefore 0.35 value was considered as the optimal smoothening parameter. The resulting optimized super resolution maps are shown in figure 5.4.

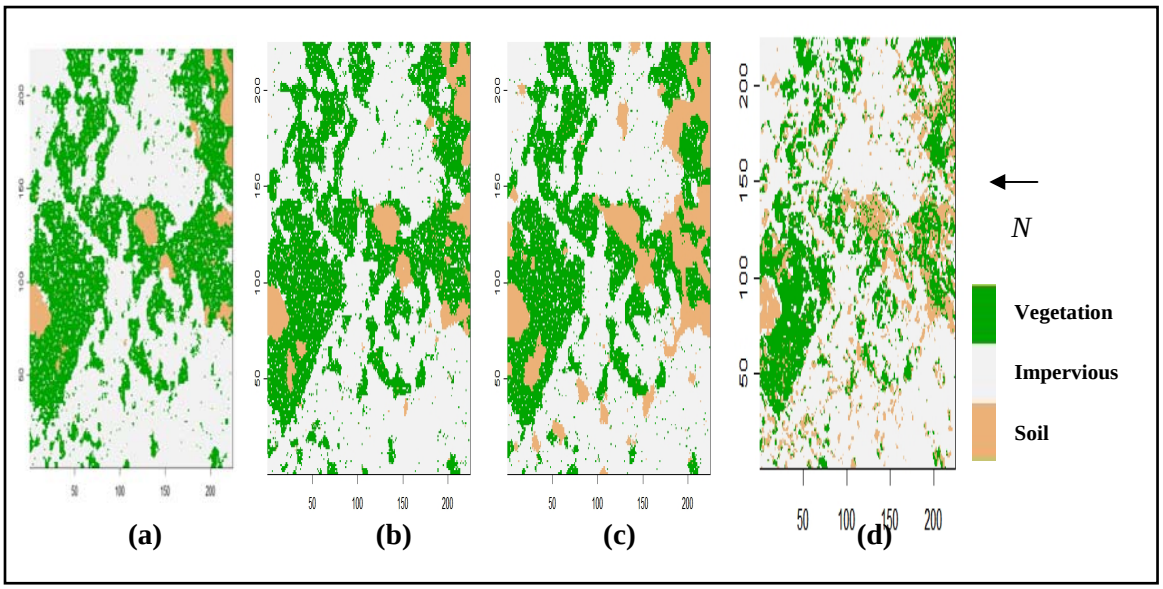

Fig 5.4 Effect of smoothening parameter on SRM, λ = (a) 0.30, (b) 0.35, (c) 0.40 and (d) Reference image

The visual interpretation of figure 5.4 shows that the vegetation and impervious classes are more closely classified to the reference image. But the soil class, especially in the upper left corner of the image has been misclassified for the vegetation class. This is mainly due to the representation of the soil class is a heavy mix of soil and grass in the Dehradun area this is much prominent for the 'fragmentized' grass land areas. Moreover soil class in most of the parts of the image represents a very small distribution. As a result it represents a very small number of pixels with respect to the other two classes. So the contextual information provided by this class will not be enough to satisfy the Markovian property. The confusion matrix shown in table 5.3, gives a better understanding over this fact. From the table 5.3, it is evident that the error of commission for the soil and the vegetation classes are at higher values with 40% and 46% respectively. These errors are visualized by the poor user accuracies for these classes. The confusion between these two classes as seen on the image and has been significantly highlighted in the confusion matrix. On the other hand impervious surface shows better user accuracy with 88%.

Table 5.3 Confusion matrix for the SRM of IKONOS image for an optimal λ value of 0.85

Class	V	S	I	Total	Error of Commission (%)	User Accuracy (%)
V	9629	3218	5301	18148	46	54
S	934	1977	424	3335	40	60
I	1558	2111	25024	28693	12	88
Total	12121	7306	30749	50176		
Error of Omission (%)	20	72	18			
Producer Accuracy (%)	80	28	82			

Considerable amount of over smoothening can be seen in figure 5.4(c) with respect to the figure 5.4(b). The abrupt drop in the Kappa agreement with the reference image shows this over smoothening effect. Overall analysis shows us when the spatial variability increases between the neighbouring pixels, for an optimal SRM the modified smoothness parameter should be set to a value in the range from 0.1 to 0.4. This also justify the condition we enforced in section 5.2, which means that for these values of λ and for the predefined class seperabilities, it can be seen the prior constraints providing additional information. The optimization process and the class seperabilities are shown in Appendix-A (fig A.6).

5.2.2. Experimental results for the comparison of OSRM fractions for the degraded IKONOS image with the Hyperion linear unmixing results

This section presents the results of the comparison of OSRM fractions with the fractions from linear unmixing of Hyperion image. As mentioned earlier, three measures of accuracy, the AEP, RMSE and the CC have been chosen for that reason.

Here we have turned the OSRM into fractions representing each class. The smooth OSRM suggests that they are well described by the contextually smooth MRF model. The fraction images generated from these OSRM can hold higher classification accuracies than the initial subpixel classification from linear unmixing due to this contextual refinement. To analyze this effectively we have compared the fractions coming from OSRM of degraded IKONOS image and linear unmixing fractions of the Hyperion image with the fractions of the reference IKONOS image.

Initially the OSRM with 4m spatial resolution has to be turned into fractions of 30m spatial resolution to compare with Hyperion fractions of 30m. To do this the OSRM pixels were aggregated to form a 30m spatial resolution image with pixels representing the fractions for each class. This aggregation was possible mainly because the OSRM represent only the pure pixels. By analyzing the two images in a pixel by pixel basis, it has been found out that 7x7 pixels of the OSRM corresponds to a 1 pixel of the Hyperion image. So to generate the fractions a formula was developed as below:

$$f(l) = \sum_{l=1}^{L} \frac{\sum_{i=1}^{N} \sum_{j=1}^{N} n_l}{N^2} \quad (5.1)$$

Here $f(l)$ represents the fraction value for a class l in a pixel, and L being the total number of classes. N represents the number of pixels in OSRM in row (i) and column (j) directions corresponding to a single pixel of the Hyperion image. Therefore 49 pixels from OSRM were used to generate a class proportion measure in a single 30m pixel. The same procedure was carried out to convert the reference image of 4m spatial resolution in to 30m fractions. In order to analyze how the initial fractions of SVD contextually get refined during the optimization process, the initial fractions were also compared to the reference fractions. To do this the initial fractions for the degraded IKONOS image at a spatial resolution of 16m had to be converted to 30m spatial resolution fractions first. By care full analysis of pixels it is found out that 4 pixels should be aggregated to convert the initial fractions to the desired 30m spatial resolution. The aggregation of these 4 pixels was carried out by taking the mean of the respective fractions in each pixel. The results of all these comparisons are shown below in the tables.

Table 5.4 Accuracy statistics for IKONOS degraded image by CC, RMSE and AEP (a) between fractions of Hyperion linear unmixing & Reference fractions (b) between SVD fractions and the reference fractions (c) between OSRM fractions and the reference fractions (d) Between the OSRM fractions and Hyperion fractions

Class	*CC*	*RMSE*	*AEP*
Vegetation	0.6432	0.2749	1.6385
Soil	0.2460	0.1870	-0.0823
Impervious surface	0.7196	0.2688	0.2910
Total		0.7307	1.8472

(a)

Class	*CC*	*RMSE*	*AEP*
Vegetation	0.3909	0.5413	-0.6202
Soil	0.1308	0.6173	-1.4286
Impervious surface	0.3908	0.3853	-0.0975
Total		1.5439	2.1463

(b)

Class	*CC*	*RMSE*	*AEP*
Vegetation	0.8521	0.2271	-0.3296
Soil	0.6846	0.1692	1.7299
Impervious surface	0.9200	0.1584	0.0579
Total		0.5547	1.4582

(c)

Class	*CC*	*RMSE*	*AEP*
Vegetation	0.6076	0.4004	-0.7459
Soil	0.2225	0.2202	1.9748
Impervious surface	0.7351	0.2829	-0.1806
Total		0.9035	1.0483

(d)

The results justify the assumptions we made before the experiments (contextual refinement leading to higher classification accuracy). The CC and the RMSE in tables 5.4(a) and 5.4(c), respectively shows the significant improvement in the classification accuracy with respect to the maximum likelihood results. The soil class which initially shows a less correlation with 0.2460 values, has been improved up to 0.6846 with the SRM, this is confirmed by the RMSE values improving from 0.1870 to 0.1692. The AEP also follows the same trend and overall values for RMSE and AEP shows the improvement in the accuracy with the values dropping from 0.7307 to 0.5547 and 1.8472 to 1.4582 respectively. This drop in overall RMSE shows the improvement in the prediction (the biasness and variance), while the AEP shows the success rate in maintaining the known proportions during prediction [10,26]. The comparative results in tables 5.3(b) and (c) shows high accuracy in the prediction and the success rate with the significant drop in RMSE and AEP values during the optimization process. And the association between the target and the prediction proportions has also been increased with the improved correlation coefficients. This justifies the contextual refinement in the fractions during the OSRM generation. Initially the fractions generated from Hyperion image shows a better overall RMSE and AEP values with 0.7307 and 1.8472 respectively and mean CC in the range of 0.6 with respect to the SVD results. This shows the increased classification accuracy that Hyperion is producing than the SVD fractions from the IKONOS degraded image. This is obvious due to the higher spectral information content hold by the Hyperion image over the degraded IKONOS in defining the endmembers for the V-I-S classes. According to the table 5.3(d) results the SRM results shows a considerably good association with respect to the Hyperion fractions, with a CC value of 0.7351 for the impervious class. But the overall RMSE of 0.9035 suggests some prediction errors in SRM with respect to Hyperion fractions. The overall AEP of 1.0483 shows an improved identical area error proportions than the other comparisons. The bivariate distribution of the known which is the Hyperion fractions and prediction variables or the fraction defined from OSRM, for each class is shown below.

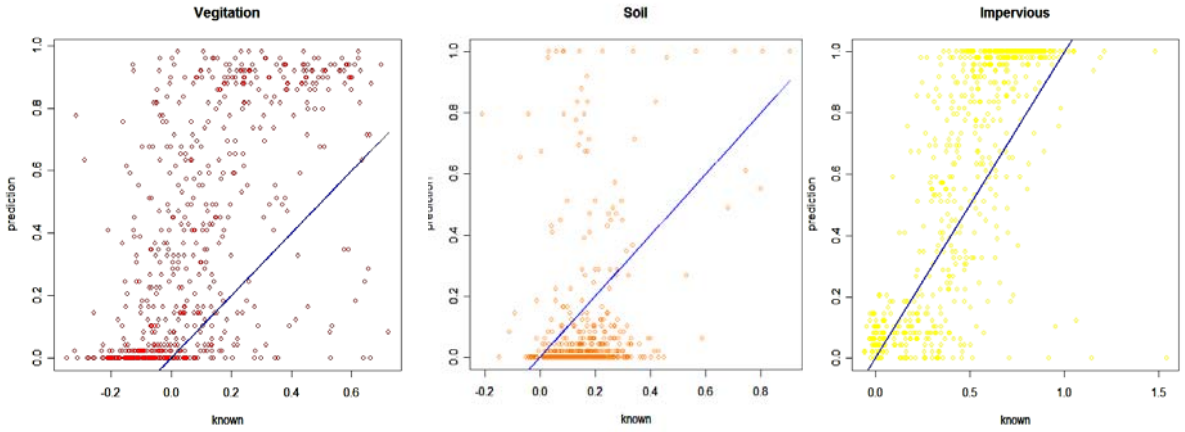

Fig 5.5 Bivariate distribution of the class proportions between the predicted fractions using MRF based SRM on degraded IKONOS image and the known fractions using linear unmixing on Hyperion image, with the best fitting line, for the classes (a) vegetation (b) Soil (c) Impervious

According to the plots impervious class shows a high correlation between the predicted and known fractions, by best fitted line being close to a one to one relationship(y=x line). The low correlation between the two variables for the soil class is significant through the plot (figure.5.5 (b)). For all the classes, number of predicted fractions is estimated as 0 or 1. Such situation can be a result of several reasons, spectral closeness or overlap between the endmembers due too the spectral similarity for the classes in urban landscape, and the aggregation process which has been used to produce the degraded

image resulting in pixels representing an average radiance values of sixteen pixels of the original data set of IKONOS multispectral image. But the overall results suggest that the OSRM holds increased classification accuracies than the linear unmixing results.

5.3. Experimental results for the ASTER (VNIR) image

In this section MRF based SRM technique is applied to a ASTER image for the bands in the VNIR region. This image was processed in way that it prevents original pixels getting resampled. In other words the three bands of the ASTER VNIR region were kept to the original grid size of 16m. This leaves the pixels getting resample by any interpolation method (see section 3.5.1). Due to this spectral integrity of the original data set the resulting SRM results will be free of the effect of resampling. The ratio between the pixel resolutions of the ASTER and IKONOS images defines a scale factor of 4. The temperature parameters were set to the same values as previous. A subset of 60x60 pixels was chosen to match the previous subset area of the IKONOS image. The classes were defined with there mean and covariance matrices by carefully selected endmembers for each class from the original 16m resolution image. The PPI image was assisted for this selection. These defined classes posses a high separability with the TD values ranging from 1.9 to 2.0 (see Appendix-B fig B.1 to B.3 and table B.1 to B.3).

5.3.1. Optimal smoothness parameter estimation

Experiments were carried out to find the optimal smoothening parameter which results in the best SRM for the ASTER image. Several smoothening parameters were used to fined out the resulting SRM accuracy, and the results are summarized in the table 5.5 with the resulting plots in fig 5.6.

Table 5.5 λ values and the resulting OA and K values, for the ASTER (VNIR) image

Λ (λ)	OA (%)	Initial K	K
0.3	65.5871	0.2134	0.3754
0.4	66.6095	0.2134	0.3962
0.45	66.6036	0.2134	0.4018
0.5	65.6435	0.2134	0.4016
0.55	66.0000	0.2134	0.3750
0.6	48.9756	0.2134	0.2561
0.9	14.8060	0.2134	0.0003

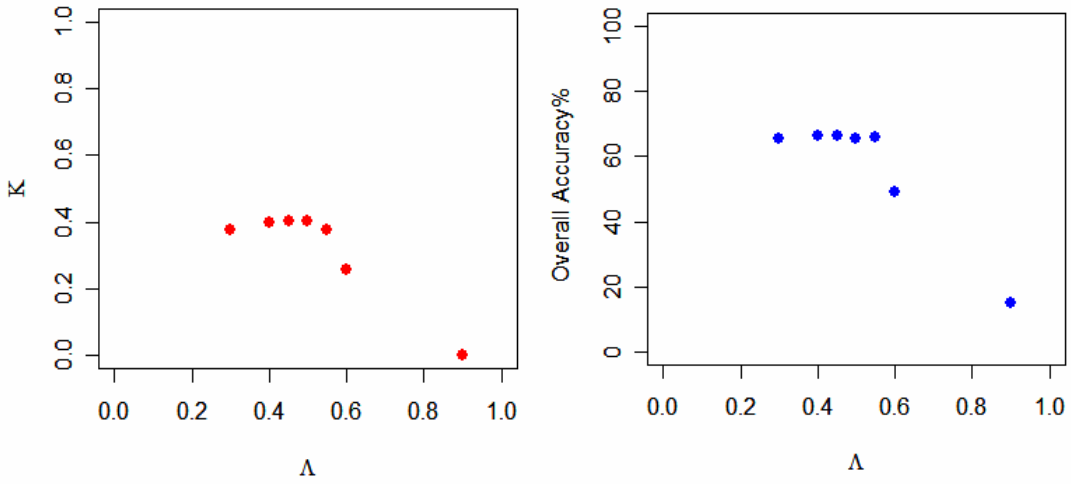

Fig 5.6 Effect of smoothness parameter on the accuracy of SRM, by OA and K , for ATSTER (VNIR) image

The results show that for the optimum results λ can take a value in the range of 0.4 to 0.5.Here the highest value of K= 0.4018 is reached for a λ value of 0.45, with a slightly higher accuracy than the values of 0.5 and 0.4 respectively. This result justifies and mirrors the conclusions of the previous results of IKONOS image. Suggesting that the optimal λ values for a scene with high spatial variability lies in the range of 0.3 to 0.5 (see section 5.2.1), which has considered the prior constraints equally as well as the likelihood constraints in SRM generation. The resulting super resolution images are shown below. The OSRM generation process for λ =0.45 is shown in Appendix-B (fig B.4).

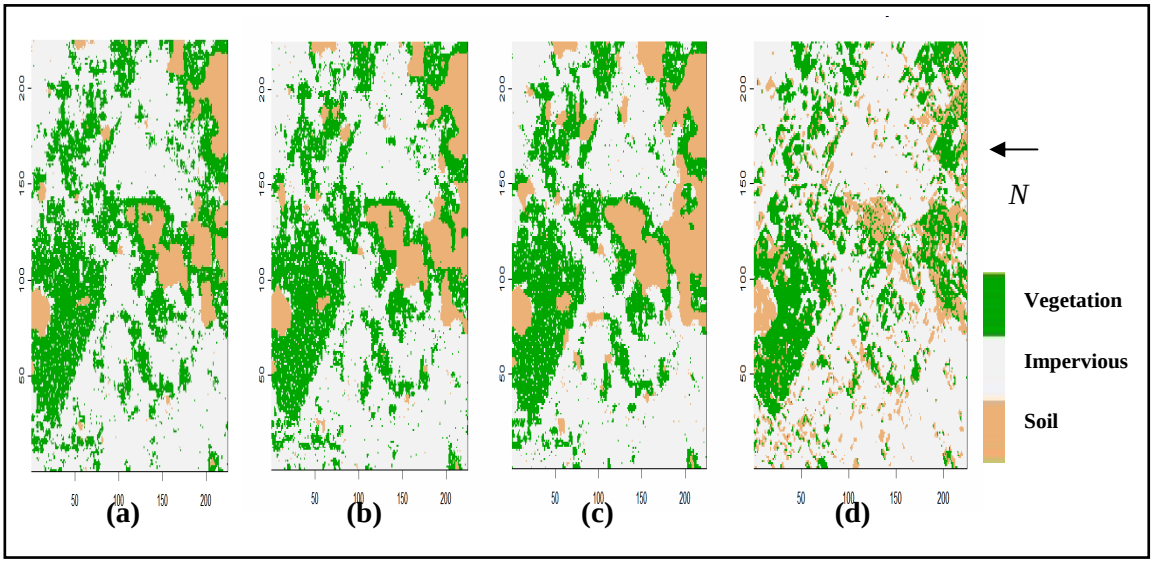

Fig 5.7 Optimized SRM for the λ values of (a) 0.4,(b) 0.45 and (c) 0.5, (d) Reference image

Visual interpretation of these resulting images shows the smoothening of the image with the growth of the λ values. Misclassification of the soil class with the vegetation is significant in the image. But the vegetation and the impervious classes have been able to maintain a close agreement with reference image. Close interpretation shows that the soil class classifies correctly in an impervious neighbourhood. This confusion carried out by the soil class can also be identified with the information from the confusion matrix. From the table 5.6 it is evident that the error of commission for the soil

class is higher than the other two classes at 61%. This shows the incorrect classification samples involved in this class.

Table 5.6 Confusion matrix for the SRM of ASTER (VNIR) image for optimal λ value of 0.45

Class	V	S	I	Total	Error of Commission (%)	User Accuracy (%)
V	7562	2486	5345	15393	50	50
S	1786	2406	1953	6145	61	49
I	2773	2414	23451	28638	18	82
Total	12121	7306	30749	50176		
Error of Omission (%)	38	67	23			
Producer Accuracy (%)	62	33	77			

5.3.2. Experimental results for the comparison of OSRM fractions for the ASTER (VNIR) image with the Hyperion linear unmixing results.

The fractions of the OSRM were compared to the Hyperion fractions in order to fined out the comparison between the two techniques. As in the previous experiment the OSRM was aggregated to show 30m spatial resolution fractions. The initial fractions generated by SVD at a spatial resolution of 16m were also aggregated to represent 30m fractions as before. The comparative results are shown in the below tables.

Table 5.7 Accuracy statistics for the ASTER (VNIR) image by CC, RMSE and AEP (a) between fractions of Hyperion linear unmixing & Reference fractions (b) between SVD fractions and the reference fractions (c) between OSRM fractions and the reference fractions (d) Between the OSRM fractions and Hyperion fractions

Class	*CC*	*RMSE*	*AEP*
Vegetation	0.6432	0.2749	1.6385
Soil	0.2460	0.1870	-0.0823
Impervious surface	0.7196	0.2688	0.2910
Total		0.7307	1.8472

(a)

Class	*CC*	*RMSE*	*AEP*
Vegetation	0.3140	0.4382	-0.5420
Soil	0.0508	0.2419	0.3238
Impervious surface	0.4158	0.3330	0.0051
Total		1.0131	-0.2131

(b)

Class	*CC*	*RMSE*	*AEP*
Vegetation	0.8208	0.2199	-0.2875
Soil	0.6267	0.1868	0.9729
Impervious surface	0.8453	0.2024	-0.0539
Total		0.6091	0.6315

(c)

Class	*CC*	*RMSE*	*AEP*
Vegetation	0.6403	0.3659	-0.7299
Soil	0.2000	0.2385	1.1498
Impervious surface	0.7399	0.2730	-0.1837
Total		0.8774	0.2362

(d)

The results illustrated by the tables above follows a similar pattern to the results shown by the IKONOS degraded image. As table 5.7(b) suggests the initial agreement of the fractions by SVD is poor with respect to the fractions estimated by the reference. With the optimization process these results have been improved significantly. This is justified by the results in the table 5.7(c), the correlation between the OSRM fractions and the reference fractions have been improved to an average in the range of 0.7, which is a good correlation between the known and the prediction. The total RMSE shows the biasness in the prediction with a high value of 0.6091 and AEP shows the over estimation of the area with a value of 0.6315.This may be explained by the errors inherited from the co-registration between the ASTER image and the reference IKONOS image, which leads to certain mismatch between the set of pixels considered for these accuracy measures. According to table 5.7(a) and (c) it is clear that the MRF base SRM technique displays a good potential for mapping accurate land cover class proportions within a pixel, from the remote sensing image than the linear unmixing technique. AEP suggests SRM technique shows a tendency for the overestimation of the class proportions but the correlation between the prediction and the known proportions have been improved significantly to a range between 0.6 to 0.8, the results shown by these tables are elaborated by the plots shown in fig 5.8.

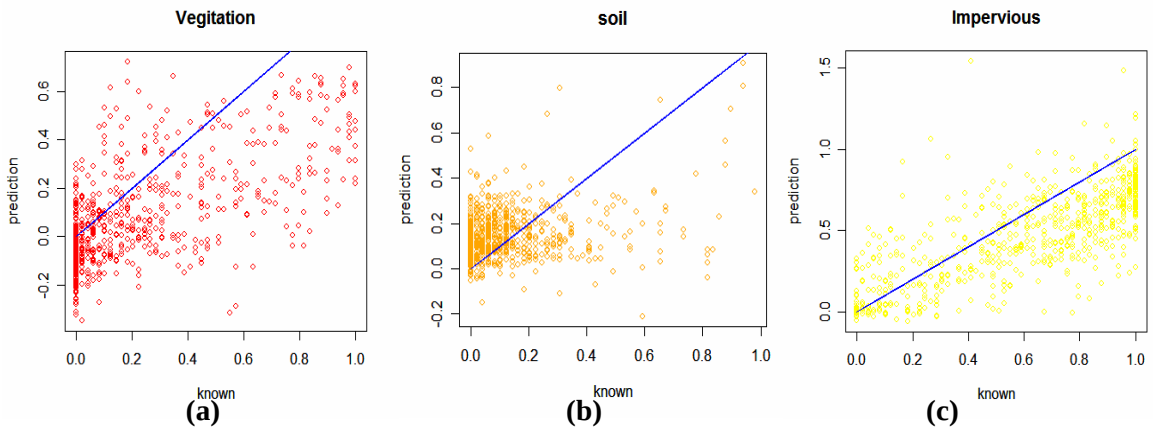

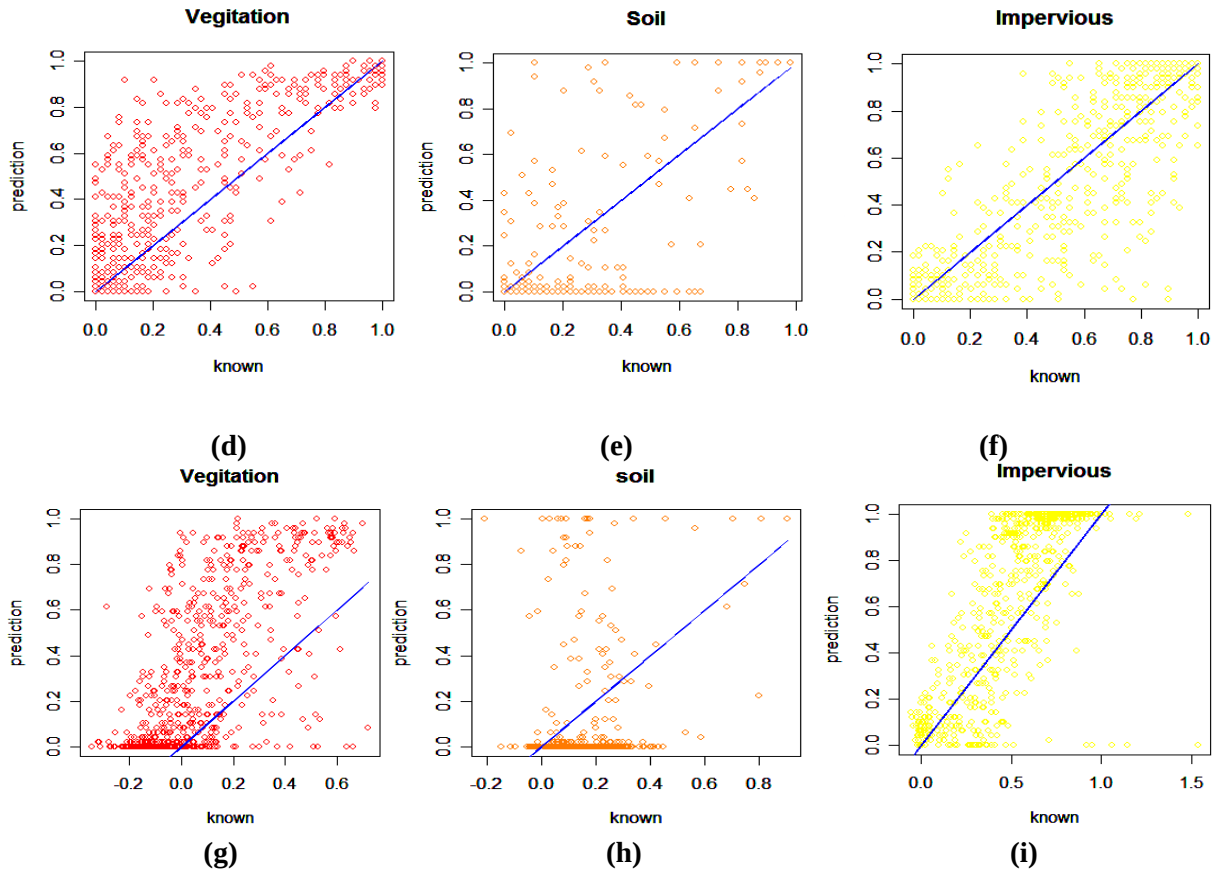

Fig 5.8 Bivariate distribution of the class proportions for V-I-S classes, with the best fitting line,(a),(b),(c),reference fractions compared to linear unmixing from Hyperion image ,(d),(e),(f)reference fractions compared to OSRM fractions as prediction,(g),(h),(i)Hyperion linear unmixing compared to OSRM fractions

5.4. Experimental results for the ASTER (SWIR) image

In this section we describe the application and results of the MRF based SRM technique for the six bands of the ASTER SWIR region. This experiment was carried out mainly to find out how the MRF based SRM technique handle the different input image characteristics. ASTER (SWIR) image represents different spatial and spectral characteristics than the inputs tried previously in this study. It has a more course spatial resolution of 30m and a spectral range representing the short wave infrared region (see chapter3). To understand the results in comparison to the previous results a subset of the same area was selected, due to the difference in spatial resolution (30m) subset represented a 30×30 pixel area. Classes were defined as mentioned earlier with there mean and covariance information. These classes show separability with TD values ranging from 1.9 to 2.0. These processing steps are shown in Appendix-B (see fig B.5 to B.7 and table B.4 to B.6).

For this experiment, certain differences were made in the preparation of the reference data set using IKONOS image. This image was resampled to grid size of 5m before applying the MLC classification to the image using the classes defined on the ASTER (SWIR) image (see section 3.5.1). This makes a scale factor of $S = 6$ to be defined between the two images, making the maximal pixel neighbours of 120 to be considered (see section 4.3).

5.4.1. Optimal smoothness parameter estimation

Tests were carried out to find the resulting optimal smoothening parameter (λ) for the ASTER (SWIR) image. Temperature parameters were defined as before. Conclusions were made using the Kappa coefficient and overall accuracy between the resulting optimum SRM and the reference image. The overall results are shown in table 5.8 and fig 5.9.

Table 5.8 λ values and the resulting OA and K values, for the ASTER (SWIR) image

Λ (λ)	OA (%)	Initial K	Final K
0.1	65.901	0.2472	0.3417
0.2	66.543	0.2472	0.3570
0.25	66.333	0.2472	0.3682
0.3	56.000	0.2472	0.2882
0.4	14.179	0.2472	0.0081
0.45	21.203	0.2472	0.0605
0.7	13.024	0.2472	0.0000

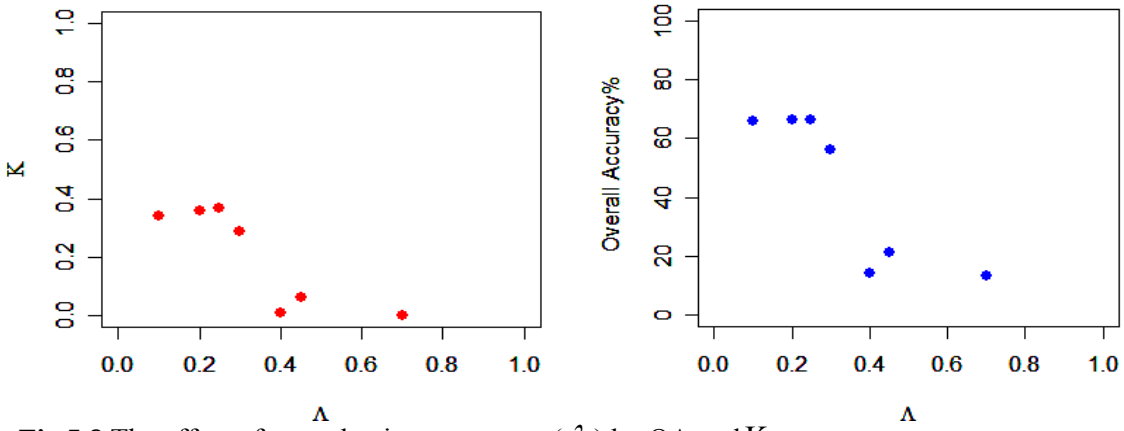

Fig 5.9 The effect of smoothening parameter (λ) by OA and K

In contrast to the previous results the optimal λ values shows a different range in achieving the optimal results. Looking at the results, the optimal values for λ seems to stay in the range of 0.1 to 0.3. And the highest accuracy levels with a K value of 0.3682 has been achieved for a λ value of 0.25. One of the reasons for this range may be the spatial resolution of the image, which makes the scene contains more homogeneous representation of objects. This means when the pixels are divided to sub-pixels the spatial dependency between the sub-pixels will not be increased significantly, still leaving the sub-pixels as mixed pixels. When this happened the contextual constraints modelled as prior energy cannot bring additional information to correctly label the pixels, claiming a low weight in the range of 0.1 to 0.3. On the other hand the labelling depends more on the likelihood constraint or spectral information, where the likelihood energy claims a higher weight $(1-\lambda)$. The resulting super resolution maps for these range is shown below.

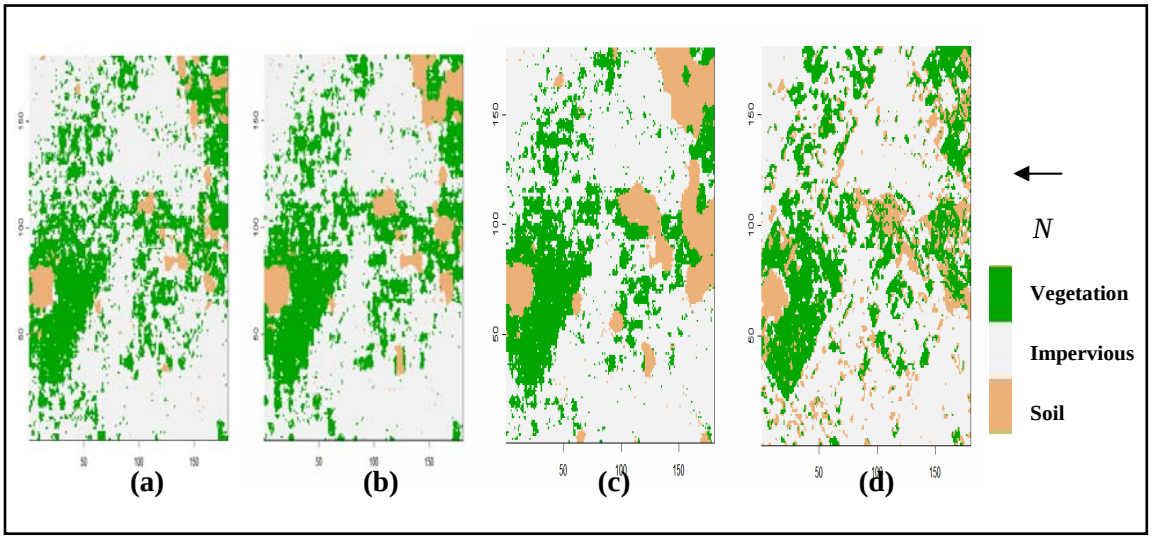

Fig 5.10 Optimized SRM for the λ values of (a) 0.1, (b) 0.2 and (c) 0.25, (d) Reference

A visual interpretation of the image 5.10(b) at optimal λ value of 0.2 has a close agreement with reference image. As in the earlier results soil class has created some confusion with vegetation class, but looking at figure 5.10(a) it can be seen that this confusion is less. Reason for this has been discussed earlier.

The confusion matrix shown in table 5.9 below gives a better understanding about the low classification accuracy for the class soil. The table shows a low user accuracy of 31% for the soil class. The misclassification of the soil class into vegetation and impervious is signified with these measures.

Table 5.9 Confusion matrix for the SRM of ASTER (SWIR) image for optimal λ value of 0.25

Class	V	S	I	Total	Error of Commission (%)	User Accuracy (%)
V	4121	994	2768	7883	48	52
S	1560	1292	1354	4206	69	31
I	2463	1873	15975	20311	21	79
Total	8144	4159	20097	32400		
Error of Omission (%)	49	69	20			
Producer Accuracy (%)	51	31	80			

The results suggest that MRF based SRM technique has been able to handle the low spatial dependency between sub pixels in labelling the pixels to each class. The optimization process with the error evaluation and energy minimization plots are shown in Appendix-B (fig B.8).

5.4.2. Experimental results for the comparison of OSRM fractions for the ASTER (SWIR) image with the Hyperion linear unmixing results.

Tests were carried out to find the comparison of the SRM results with the linear unmixing results. Initial fractions from SVD and the Fractions generated from the OSRM with the linear unmixing results were compared to the fractions generated form the IKONOS reference image, finally the results from the OSRM and Hyperion fractions were compared with each other. These results are shown in the tables below.

Table 5.10 Accuracy statistics for the ASTER (SWIR) image by CC, RMSE and AEP (a) between fractions of Hyperion linear unmixing & Reference fractions (b) between SVD fractions and the reference fractions (c) between OSRM fractions and the reference fractions (d) Between the OSRM fractions and Hyperion fractions

Class	*CC*	*RMSE*	*AEP*
Vegetation	0.6419	0.2795	0.6178
Soil	0.3800	0.1746	-0.2194
Impervious surface	0.6638	0.3032	0.2464
Total		0.7573	0.6448

(a)

Class	*CC*	*RMSE*	*AEP*
Vegetation	0.7126	0.2499	-0.3334
Soil	0.5912	0.1804	3.4077
Impervious surface	0.8237	0.1946	0.0160
Total		0.6249	3.0903

(b)

Class	*CC*	*RMSE*	*AEP*
Vegetation	0.8109	0.1949	-0.1390
Soil	0.5425	0.2004	0.6791
Impervious surface	0.8127	0.2133	-0.0169
Total		0.6086	0.5232

(c)

Class	*CC*	*RMSE*	*AEP*
Vegetation	0.7470	0.2851	-0.6710
Soil	0.3195	0.2270	1.0476
Impervious surface	0.7680	0.2803	-0.2592
Total		0.7924	0.1174

(d)

The results mirror the previous results we achieved during the experiments. According to the table 5.10(a) Hyperion fractions from linear unmixing shows a marginal association with reference fractions from IKONOS image, with the CC being 0.6419 and 0.6638 for the vegetation and impervious classes respectively. The poor classification results for the soil class has been repeated again with the CC of 0.3800. Table 5.10(b) demonstrate the initial results of the SVD fractions, which significantly improved with the optimization process. Looking at the results in table 5.10(d) it can be seen that the optimized super resolution map shows a good correlation with the results coming from the hyperspectral image, this is justified by the overall AEP value of 0.1174. Finally with respect to the tables 5.10 (a) and (c) the significant improvements in the classification results can be seen, with the

CC improving in to the range of 0.8 for the vegetation and impervious classes and for the soil class the correlation value of 0.38 in the Hyperion linear unmixing has been improved to value of 0.5425 in the SRM results. These results shown by the CC have been mirrored by the total AEP and RMSE values. The biasness in the predictions using SRM technique is less than what it is in the linear unmixing, with the total RMSE falling down from 0.7573 to 0.6086 and the total AEP is falling from 0.6448 to 0.5232. The overall results indicate that higher classification accuracies can be obtained using the SRM with respect to the linear unmixing techniques. The bivariate distributions of the class proportions leading to these results are shown below.

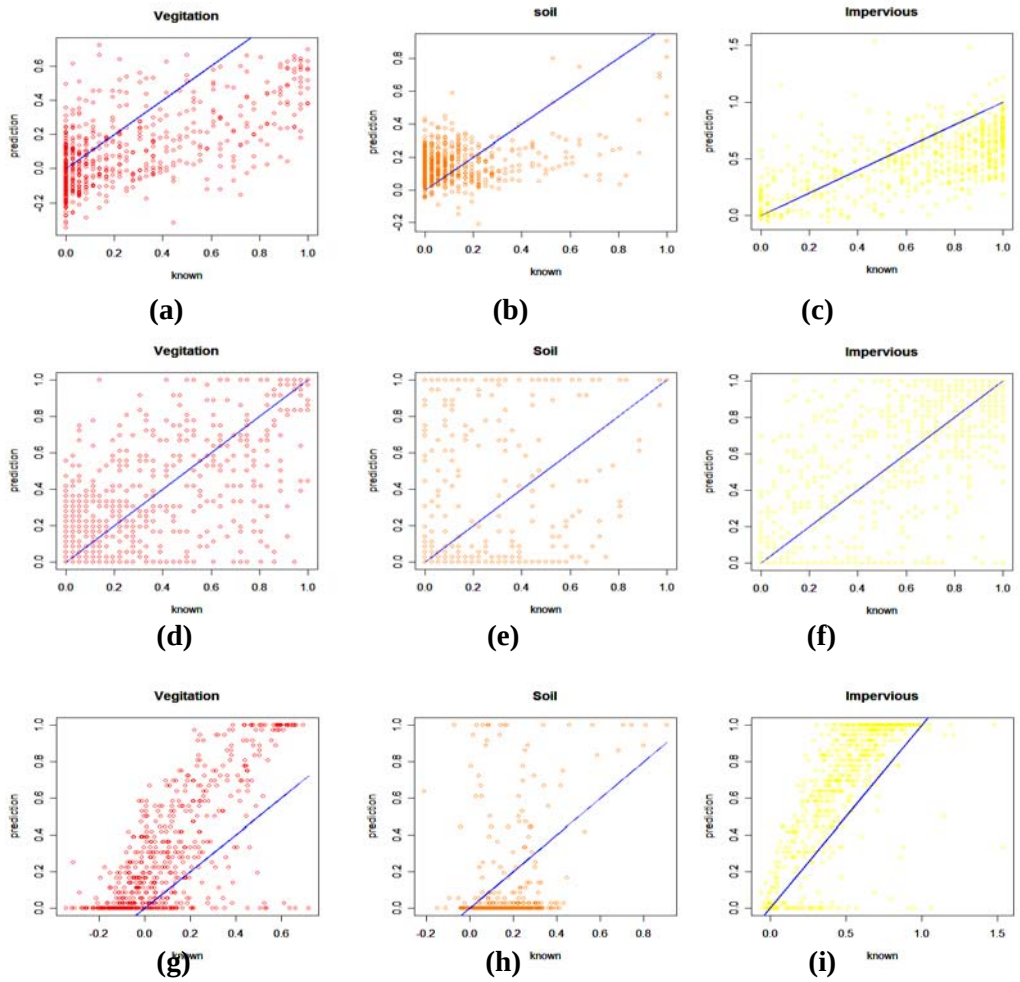

Fig 5.11 Bivariate distribution of the class proportions for V-I-S classes, with the best fitting line,(a),(b),(c), reference fractions compared to linear unmixing from Hyperion image ,(d),(e),(f) reference fractions compared to OSRM fractions as prediction,(g),(h),(i) Hyperion linear unmixing compared to OSRM fractions

5.5. Experimental results for the Landsat image

Only the 6 bands in the VNIR range with spatial resolutions of 30m were used for the experiments. The preparation of the reference data set for this image was explained in chapter 3. The MRF model was used to produce super resolution map of 5m spatial resolution. To define the likelihood energy function the classes were defined with there mean and covariance information, and the TD value for the separability of these classes were kept in the range from 1.9 to 2.0. A subset of 30x30 pixels

representing the same study area as for the previous experiments was selected for better analysis of the results. The processing results are shown in detail in Appendix-C (see fig C.1 to C.3 and table c.1 to C.3)

5.5.1. Optimal smoothness parameter estimation

In finding out the optimal smoothening parameter (λ) for the SRM, several λ values were tested for the highest K and OA agreement between the resulting SRM and the reference map. Results achieved during this experiment are shown below in the table and figure below.

Table 5.11 λ values and the resulting OA and initial and final K values, for the Landsat image

Λ (λ)	OA (%)	Initial K	Final K
0.1	68.278	0.2459	0.3753
0.2	69.954	0.2459	0.3985
0.25	71.333	0.2459	0.4224
0.3	70.710	0.2459	0.4112
0.45	54.809	0.2459	0.2226
0.7	10.222	0.2459	0.0270

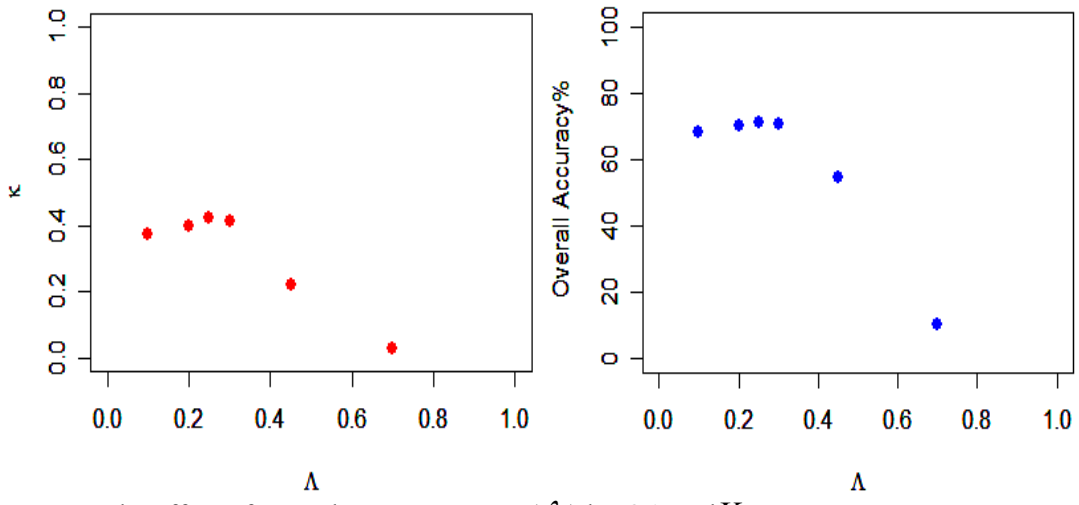

Fig 5.12 The effect of smoothness parameter (λ) by OA and K

The results follow the results achieved previously for the ASTER (SWIR) image. The optimal λ value was determined as 0.25 with highest K value of 0.4224 and OA with 71.333%. The optimal range for smoothening parameter lies between 0.1 to 0.3. This shows the similar behaviour of the MRF model parameters in generation of the SRM for the different image characteristics of the Landsat image and the ASTER (SWIR) image. This range of λ values suggests that in the generation of the OSRM it has considered the abrupt changes in the neighbourhood inherent to these low spatial resolution (30m) images. In other words the low values of λ suggests the pixel labelling consider the majority of neighbours in a very minor level.

The scale factor of 6 used in this experiment considers 120 pixels of maximal neighbourhood in defining the Gibbs potential parameters related to the spatial dependence of class attributes. At a 30m spatial resolution of the Landsat image with a neighbourhood size of 120 the validity of the assumptions regarding the purity of the pixels leading to spatial dependence tend to break apart. This can also leads to low λ values controlling the prior energy as suggested by the results. The resulting initial SRM and the optimized SRM with the temperature curves and the energy minimization is shown in Appendix-C (fig C.3). Resulting OSRM for the optimum smoothening parameters are shown below.

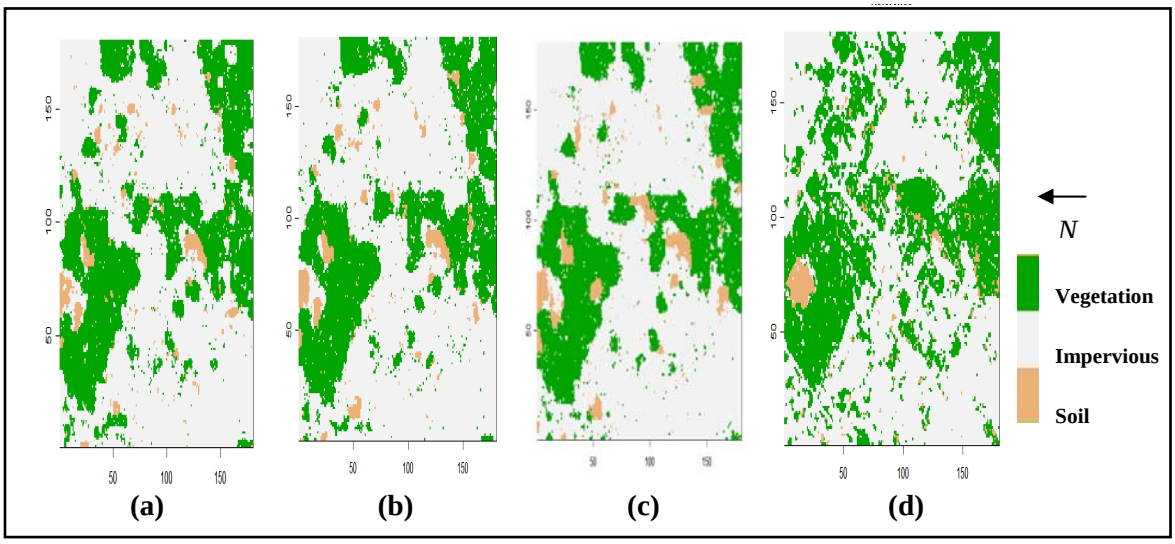

Fig 5.13 Optimized SRM for the λ values of (a) 0.2, (b) 0.25 and (c) 0.3, (d) Reference

Visual interpretation of these results shows the resemblance of the optimized super resolutions maps to the reference image. The OSRM produced with optimum λ value of 0.25 shown in figure 5.13(b) shows a high agreement with the reference image than the other two images (5.13 (a) and (b)). Vegetation class and the Impervious surface class show a high agreement with the reference image than the soil class. The confusion in classifying the soil class has been followed as in previous experiments. This is justified by the information in the confusion matrix shown below in the table 5.12.

Table 5.12 Confusion matrix for the SRM of Landsat image for optimal λ value of 0.25

Class	V	S	I	Total	Error of Commission (%)	User Accuracy (%)
V	6880	402	2938	10220	32	68
S	597	185	480	1262	85	15
I	4278	593	16047	20918	23	77
Total	11755	1180	19465	32400		
Error of Omission (%)	41	84	17			
Producer Accuracy (%)	59	16	83			

According to table 5.12 the classification accuracy of the soil class is very low 15%.And it also shows good user accuracies for the vegetation and impervious classes with 68% and 77% respectively. This follows the visual interpretation results over the optimized SRM of Landsat image.

The resulting images shows an significant smoothness for each class, this makes the OSRM more visually appealing, but it degrade the quality of the image due to the missing of the details. One reason for this is the high scale factor $(S = 6)$ used, which invariably grow the neighbourhood size. This significantly improves the effect of prior energy, with many sub pixel configurations with equivalent contextual energy, making the OSRM to become more smoother even with a low smoothening parameter value (λ). The next reason may be with a higher value of S the number of subpixel with in the coarse resolution pixel tend to increase, this makes the coarse resolution pixel to be highly mixed. Then the process requires appropriate spectral information in the means of class mean and covariance to define the likelihood energy as additional information. This is difficult with the less number of pure pixels in a 30m spatial resolution Landsat image. When the likelihood energy is controlled by a higher smoothening value $(1-\lambda)$ the more homogeneous objects (eg. Vegetation patches) with more number of pure pixels tend to be classified properly than the scattered object (eg. soil). With these adjustable limitations the achieved results seems to be acceptable for the further analysis. The results of the OSRM and the Hyperion linear unmixing were comparatively analysed. These results are shown below.

Table 5.13 Accuracy statistics for the Landsat image by CC, RMSE and AEP (a) between fractions of Hyperion linear unmixing & Reference fractions (b) between SVD fractions and the reference fractions (c) between OSRM fractions and the reference fractions (d) Between the OSRM fractions and Hyperion fractions

Class	*CC*	*RMSE*	*AEP*
Vegetation	0.8230	0.3247	0.7307
Soil	0.5708	0.1549	-2.6871
Impervious surface	0.7682	0.2633	0.2222
Total		0.7429	-1.7342

(a)

Class	*CC*	*RMSE*	*AEP*
Vegetation	0.5523	0.3007	-0.0282
Soil	0.4841	0.2181	-1.8034
Impervious surface	0.7292	0.2468	-0.0699
Total		0.7656	1.9015

(b)

Class	*CC*	*RMSE*	*AEP*
Vegetation	0.6883	0.2882	0.2759
Soil	0.3251	0.1440	-0.1624
Impervious surface	0.7290	0.2757	-0.1001
Total		0.7079	0.0134

(c)

Class	*CC*	*RMSE*	*AEP*
Vegetation	0.7023	0.3177	-0.6563
Soil	0.2689	0.1821	2.0881
Impervious surface	0.6242	0.3570	-0.3001
Total		0.8568	1.1317

(d)

According to the results in the table 5.13 (a) and (c) the linear unmixing results have a marginally high correlation with respect to the OSRM results with the reference fractions generated from the IKONOS MLC classified image. With the overall RMSE dropping slightly from 0.7429 to 0.7079 MRF base SRM results shows its advantage in correctly predicting the fractions. And this has been justified by an identical AEP measure of 0.0134 for the OSRM results. The results in the table 5.13(d) show the measures of accuracies for the OSRM fractions with respect to the Hyperion fractions. For the classes of vegetation and impervious surface the correlation between the fractions is good with average CC lying around 0.6, and the overall RMSE and the AEP values of 0.8568 and 1.1317 respectively shows some prediction errors, due to contribution of the soil class. The overall results suggest that the MRF base SRM technique on Landsat image has a marginally higher advantage than the linear unmixing technique with the hyper spectral (Hyperion) remote sensing image. The resulting plots shown below elaborate these results.

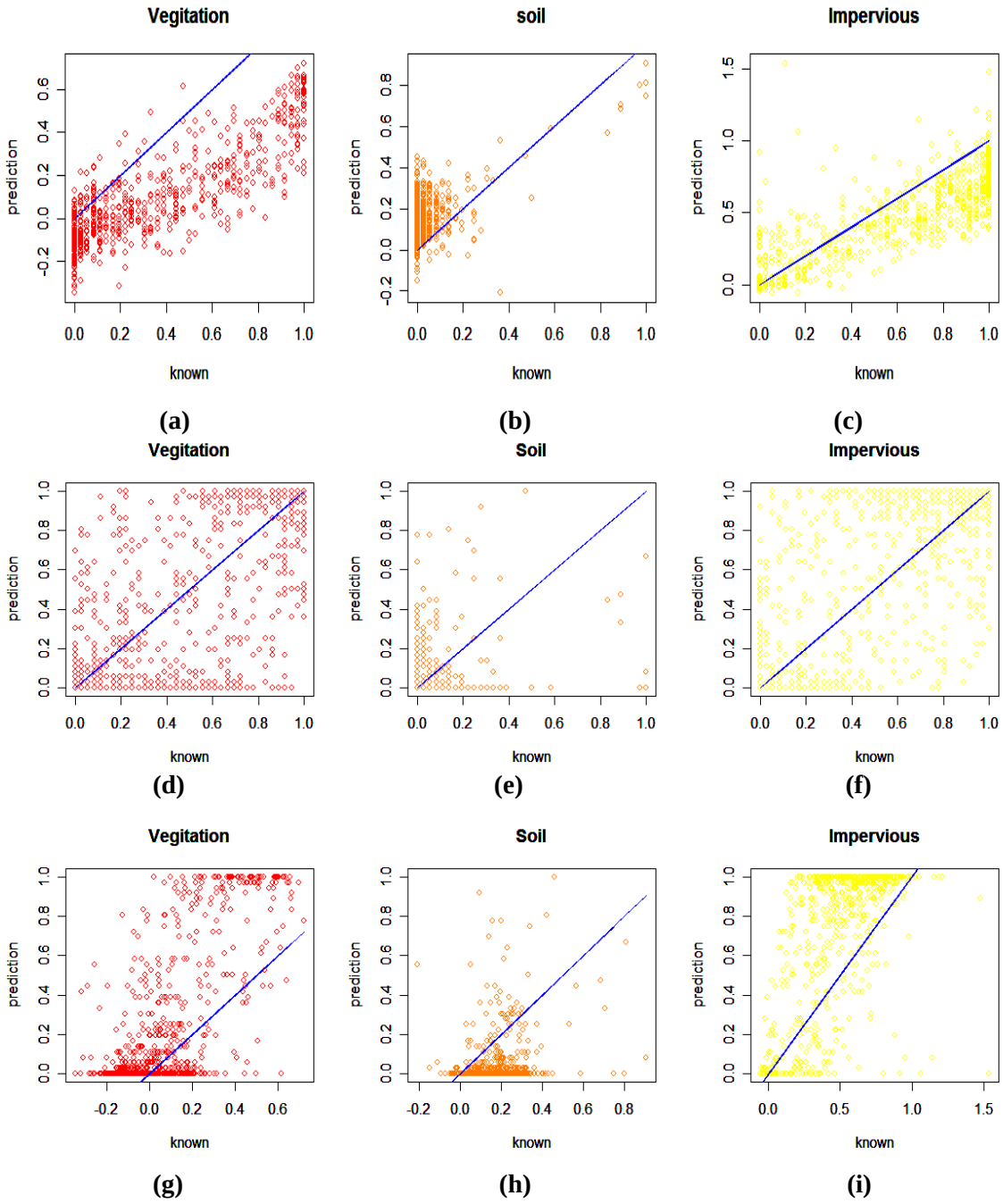

Fig 5.14 Bivariate distribution of the class proportions for V-I-S classes, with the best fitting line,(a),(b),(c)),reference fractions compared to linear unmixing from Hyperion image ,(d),(e),(f) reference fractions compared to OSRM fractions as prediction,(g),(h),(i)Hyperion linear unmixing compared to OSRM fractions

5.6. Summary of observation from the results

The results obtained on applying the MRF based SRM technique using IKONOS image shows that to model the contextual information needed for an accurate land cover classification, the global energy needs to be modelled with a higher λ value (smoothness parameter) in the range of 0.3 to 0.5. This

smoothness parameter range was justified with the similar results obtained from ASTER (VNIR) image. The λ range experienced in case of low resolution satellite images like ASTER (SWIR) and Landsat image was different wherein the global energy has a tendency to depend on likelihood energy more than the prior energy, claiming the λ values to stay in the range of 0.1 to 0.3 and also the range for the optimal λ values getting narrowed down to a lower range. In other words, it is observed that the class labelling depends more on the spectral information. This justifies the need of accurate estimation of mean and covariance matrices for each class which is fundamental for better results, using the low resolution images. The research work carried out using ASTER, Landsat and IKONOS (MSS) data suggest that the SRM technique gives higher accuracy than the linear unmixing technique using spectrally rich Hyperion data.

The overall results suggests that with different input image characteristics (spectral and spatial resolutions), the input parameters should be tuned to obtain optimal results. Moreover, these parameters tend to change, depending on the image characteristics, especially the spatial resolution. For a high spatial resolution remote sensing images, the optimal smoothness parameter takes a higher value giving contextual information more weight than the coarse spatial resolution. Pixels neighbours at a higher spatial resolution tend to belong to the same class (at high spatial resolution the pixels are more pure). This leads the Gibbs potential function to take low values. As a matter of fact these pixels which correspond to low energy state have a high probability in generating a class. This leads to a more strong behaviour of the prior energy function in the global energy construction. In other words this means that the prior energy brings in the additional information to classify the image pixels correctly. Hence this can lead it taking a higher weight (λ) than in the case of a lower spatial resolution image.

The results can also be used to observe the effect of the spectral range of these images for the optimal outputs. From all the input images, IKONOS data are quantized to unsigned 16bit values, where brightness value range is from 0 to 65535 whereas ASTER and Landsat sensor data are quantized to unsigned 8 bit value with brightness values ranging from 0 to 255. These digital numbers have not being scaled to 0% to 100% reflectance scale. Hence, in the case of IKONOS image the spectral values for the same class are scaled to larger values than in the other images (see Appendix-C, table C.4). They provide different inputs for the SRM generation process. The influence of these different spectral ranges can also be observed by their effect on the likelihood energy values. Likelihood energy depends on the Mahalanobis distance of the pixels (see eq.4.11). According to eq.4.11 the likelihood energy is modelled by using the class mean and covariance values for the Mahalanobis distance as the first part $((\sum_i \frac{1}{2}(y(b_i)-\mu_\alpha)^T \sum_\alpha^{-1}(y(b_i)-\mu_\alpha))$ and also an additive term $(\frac{1}{2}\ln\det\sum_\alpha)$ as the second. Mahalanobis distance will not be affected by the different radiometric ranges, because all the mean and covariance values and the pixel values will be lying in the same scale. But the additive term in the equation which determines the log value of the determinant of covariance matrix can change with the different radiometric scales. This additive term is a higher value in the case of IKONOS image than the other images (see Appendix-C, table C.4), which eventually gives the likelihood energy a higher value. Though the likelihood energy poses these variations due to the radiometric range of the dataset, result from IKONOS and ASTER (VNIR) images suggest that there is no significant difference in treating the likelihood energy for the optimal results. The observation on ASTER (SWIR) and Landsat images also justifies the above conclusions. Though these two images

belong to different spectral regions (see Appendix-B, table.B.4 and Appendix-C, tableC.1) the optimal results have followed similar parameter estimation. Hence, it can be concluded that the spectral range of these MSS images may not have an effective influence over the optimal SRM results.

The comparative analysis between the Hyperion linear unmixing results and the MRF based SRM results based on RMSE, AEP and correlation coefficient shows that the MRF models produce super resolution maps with accurate fractional representation for each class at the subpixel level than the linear unmixing results using the hyper spectral images.

6. Conclusion and recommendation

The main objective of this study was to analyze the effectiveness of Markov Random Field based super resolution mapping technique in an urban environment defined by V-I-S model (urban composition).The widely used linear unmixing technique was integrated to analyze the effectiveness. It contained several sub objectives as follows.

- Using the existing Markov Random Field based super resolution mapping method and modify it in order to apply on different spatial and spectral resolution images
- To integrate the advantages of hyperspectral images for the study of urban composition
- To study the effect of different input image characteristics on super resolution mapping and the determination of model parameters in the context of urban composition study
- Finally to compare the effectiveness of super resolution methods with the standard SMA techniques (Linear Unmixing)

In achieving these objectives six research questions was formulated. The study incorporates four different real satellite imageries namely IKONOS, ASTER and Landsat for the SRM technique and for making an effective analysis Hyperion hyperspectral was used for the linear Unmixing. The results obtained from the experiments were discussed in Chapter 5.This chapter dedicates it self to draw a conclusion with respect to the research questions. Further more it draws attention to some recommendations for the further research.

6.1. Conclusion

6.1.1. Parameter determination with respect to different real satellite image inputs

Parameter determination is an important step for optimizing the performance of the super resolution mapping. This study applies the MRF based super resolution mapping to a significant number of real satellite images with different characteristics for the first time. It revealed the relationship between these parameters and the accuracy of the super resolution map. The first research question tries to reveal how the class definitions and different MS satellite images reveal the relationship between the scale factor and the neighbourhood size. Two scale factors were attempted in this study; those are the scale factor of 4 for the ASTER (VNIR) and IKONOS images and scale factor of 6 for the ASTER (SWIR) and Landsat images. The training classes were defined with higher number of pixels representing each class and with maximum class separability, so that the covariance and mean information for each class will not be underdetermined (see appendix-A,B,C). For each of these scale factors the neighbourhood size was set to grow with a neighbourhood size defined by 7x7 window for the scale factor 4 and 11x11 window for the scale factor 6. Though the neighbourhood size was not set to a constant for each of these scale factors, the results suggested that the growth of the neighbourhood size with respect to the scale factor works well. This can be seen with the accuracies of the SRM generated from the ASTER (SWIR) and Landsat images with 30m spatial resolution being very close to the accuracies of the SRM generated from 16m ASTER (VNIR) image. In the case of coarse spatial

resolution image (30m), a single pixel is segregated to a large number of sub pixels to generate the SRM, when the neighbourhood size grows with respect to the scale factor all of these sub pixels can be incorporated for the prior energy generation.

The second research question draws the attention towards the smoothness parameter (λ), which acts as a balancing factor between the prior and likelihood energy functions for the global energy. In this study this was taken in the range between 0 and 1. The behaviour of this parameter differs depending on the input satellite image characteristic. Experiments suggest that, the optimal λ value has a higher sensitivity to the spatial resolution of the image and the scene characteristics of the input image. When this parameter was tested for the degraded IKONOS image (with a spatial resolution of 16m) the optimal values were achieved in the range of 0.3 to 0.5 and similar results follow for ASTER (VNIR) image (16m spatial resolution). But for the ATSER (SWIR) and Landsat images (spatial resolution of 30m) the optimal λ value ranged from 0.1 to 0.3. This suggests that for coarser spatial resolution images (with a spatial resolution greater than 16m); optimal smoothing parameter should be set to a value between 0.1 to 0.3. The higher values of λ for higher spatial resolution images suggest the pureness of the image pixels can lead to more valid contextual information than the low spatial resolution images. The MRF based SRM technique favours large and homogeneous objects more than the small discrete objects due to the presence of the rich contextual information of the large objects. The overall work suggests that though the image is of resolution less than 16m if it covers a heterogeneous scene it falls in the category of being a very coarser resolution image, which requires a λ value accordingly as suggested above.

The spectral range of the images and its effect on the likelihood energy was discussed in section 5.6. The additive term in likelihood energy (see eq.4.11), which depends on the class covariance matrix takes into account these differences in the spectral range. This term was studied for each of these images to draw a conclusion. As IKONOS image digital values are quantified to a higher radiometric range of 16bit, the additive term brought in a higher value for the likelihood energy than the other images. Also due to the SWIR spectral range of ASTER image and the VNIR spectral range of Landsat image, the log of the determinant of the covariance matrix changes. But the final results between the IKONOS degraded image (16m) and the ASTER (VNIR) image (16m) shows that the changes in the spectral range has not being effected for the optimal results. The optimal parameters followed the same trend for both these images. Furthermore the ASTER (SWIR) and Landsat (VNIR) images showed an optimal smoothness value of 0.25 for the highest kappa agreement with the reference image. In this respect, it can be seen that the variations in the spectral range of these images has not been significantly affecting the optimal smoothness parameter.

As the fourth research question tries to find out the effect of local specifics such as smog and dust for the classification results, an attempt was not put to follow this question in the study. One reason for this is that most of the images used in the study were acquired in the later months of the year where the study area Dehradun experience the winter season. This means that these images are not subjected to these local specifics in these times of the year. Dehradun normally has a very good visibility in winter season (greater than 25 km).

The fifth research question tries to find out the best possible method to asses the classification accuracy. Measures assessing accuracy of land cover classification are important because a good

practical classification method should be chosen among several available methods. Nearness between an actual classification results and the complete classification should play a major role for the accuracy assessment. This question was aggregated in this study mainly due to two reasons - one is to accurately analyse the results and the other to address certain discriminations in the past [45] over the well known accuracy measures in remote sensing techniques. According to some research conducted in the past [45] it has been shown that Kappa statistics for the accuracy has an unfavourable features. To identify these effects, this study incorporates five measures of accuracy with their own advantages (refer to chapter 4), namely Overall accuracy (OA), Kappa coefficient (K), Root Mean Square Error (RMSE), Correlation Coefficient (CC), Area Error Proportion (AEP). By using all these measures we assessed our results. The OSRM results were assessed by OA and K, while the linear unmixing results and the MRF based SRM results were analysed by RMSE, CC and AEP. Experiments shows that the agreement of OSRM with the respect to the reference image shown by K and OA values are justified by the results for the fractions between the OSRM and the reference suggested by the RMSE, CC, and AEP values (refer Chapter 5). Hence, it is suggested that analysing the results with all these accuracies will lead to a good understanding of the classification results and the pattern of error propagation than by using one accuracy measure.

The last research question which leads to the main objective of this study examines the most effective method in the context of urban composition between the MRF based SRM technique and the linear unmixing technique. According to the results obtained from the experiments over the different types of input images the MRF based SRM technique shows promising advantages over the linear unmixing technique in defining class proportions at the subpixel level. The fraction images generated form the OSRM shows higher agreement than the linear unmixing fractions on Hyperion image and with the reference fractions from IKONOS. In the case of Landsat image both these techniques compete to show more similar classification accuracy with respect to the average CC close to 0.6. Overall results suggests that SRM technique has a slight advantage and moreover in all the experiments the refinement in the subpixel class fractions due to the contextual information modelled by the prior probability can be seen looking at the accuracy measures between the initial SRM and the optimized SRM. The results also suggest the advantage of integrating the Hyperion image for the linear unmixing with respect to the multispectral images is signified by the accuracy statistics showing better results for the Hyperion fractions than the initial multispectral image fraction, and the improvement of the multispectral fractions with optimization process.

6.2. Recommendation

This research addresses most of the limitations in MRF base SRM technique in the application of the real satellite images. The technique was tested in a heterogeneous urban environment for its superiority. Future researches should be directed to address some of the existing limitations and also for further applications. The following are some of the recommendations for the further research.

- The application of the MRF based SRM technique on Hyperspectral remote sensing images to aggregate the advantages of its high spectral dimensionality.

- Assessment of the errors introduced to the model due to resampling of the image

Bibiliography

[1] Lee, S and Lathrop, R.G., 2006. Subpixel Analysis of Landsat ETM+ Using Self-Organizing Map (SOM) Neural Networks for Urban Land Cover Characterization. *IEEE Trans.on Geosci.and Remote Sensing*, 44(6): 1642-1654

[2] United, Nations. 1997. *Urban and Rural Areas 1996*, Annual. Report,ST/ESA/SER.A/166,Sales No.E.97.XIII.3.

[3] Ridd.M.K, 1995. Exploring a V-I-S (Vegetation-Impervious surface-Soil) model for urban ecosystem analysis through remote sensing: comparative anatomy for cities. *International Journal of Remote Sensing*, 16: 2165-2185.

[4] Wu, C., and Murray, A.T., 2002. Estimating impervious surface distribution by spectral mixture analysis. *Remote Sensing of Environment*, 84: 493-505.

[5] Powell, R.L., Dar, A., Roberts, .Philip E, Dennison., and Hess, L.L., 2006. Sub-pixel mapping of urban land cover using multiple endmember spectral mixture analysis: Manaus, Brazil. *Remote Sensing of Environment*: 1-15.

[6] Wu.C., 2004. Normalized spectral mixture analysis for monitoring urban composition using ETM+ Imagery. *Remote Sensing of Environment* (93): 480-492.

[7] Roberts, D.A., Gardner, M., Church, R., Ustin, S., and Green, R.O., 1995. Mapping Chaparral in the Santa Monica mountains Using Multiple End Member Spectral Mixture Models. *Remote Sensing of Environment*, 65: 267-279.

[8] B.Tso and Mather, P., M., C, 2001. *Classification methods for remotely sensed data*. London etc: Taylor & Francis.

[9] Tatem, A.J., Lewis, H.G., Atkinson, P.M., and Nixon, M.S., 2001. Super-resolution target identification from remotely sensed images using a Hopfield neural network. *IEEE Trans.on Geosci.and Remote Sensing*: 781-796.

[10] Tatem, A.J., Lewis, H.G., Atkinson, P.M., and Nixon, M.S.,2001. Multiple-class land-cover mapping at the sub-pixel scale using Hopfield neural network. *JAG*, 3(2): 184-190.

[11] Hailu, R.K., 2006. Suitability of Markov Random Field-based Method for Super-Resolution Land Cover Mapping, *MSc Thesis*, ITC, Enscede.

[12] KasetKasem, T., Arora, M.K., and Varshney, P.K.,2003. Sub-pixel Land cover Mapping Based on Markov Random Field Models. *IEEE Trans.on Geosci.and Remote Sensing*: 3456-3458.

[13] Varshney, P.K., and Arora, M.K., 2004. *Advanced Image processing Technique for Remotely Sensed Hyperspectral Data*. Germany, Springer.

[14] Tang, J, Wang, L., and Myint, S.W., 2007. Improving urban classification through fuzzy supervised classification and spectral mixture analysis. *International Journal of Remote Sensing*, 28(18): 4047-4063.

[15] Holben, B.N., Yosio, E.,and Shimabukuro, 1993. Linear mixing model applied to coarse spatial resolution data from multispectral satellite sensors. *International Journal of Remote Sensing*, 14(11): 2231-2240.

[16] Phinn, S, Stanford, M.,and Scarth, P., 2002. Monitoring the Composition and form of Urban Environment Based on Vegetation-Impervious Surface- Soil (VIS) Model by sub pixel Analysis Technique. *International Journal of Remote Sensing*, 23(20): 4131-4153.

[17] 2002. ERDAS Field Guide, fourth ed.Atlanta, Georgia.

[18] Jenson, J.R., *Introductory Digital Image Processing A Remote sensing perspective*. Prentice Hall, New Jersey.

[19] Fisher, P., 1997. The pixel:a snare and a delusion. *International Journal of Remote Sensing*, 18(13): 2593-2599.

[20] Geladi, P., and Hans, G., 1996. *Multivariate Image Analysis*. John Wiley & Sons Ltd, West Sussex, England.

[21] Geman.S and Geman.D, 1984. Stochastic relaxation, Gibbs distributions, and the Bayesian restoration of images. *IEEE Transaction on pattern analysis and machine intelligence*, 6: 721-741.

[22] Cutler, M.E, Lewis, H.G and Atkinson, P.M., 1997. Mapping sub-pixel proportional land cover with AVHRR imagery. *International Journal of Remote Sensing*, 18(4): 917-935.

[23] KasetKasem, T., Arora, M.K., and Varshney, P.K.,2005. Super-resolution land cover mapping using a Markov random field based approach. *Remote Sensing of Environment*, 96: 302-314.

[24] Neher, R and Srivastava, A., 2005. A Bayesian MRF Framework for Labelling Terrain Using Hyperspectral Imaging. *IEEE Trans.on Geosci.and Remote Sensing*, 43: 1363-1374.

[25] Jain, S., 2007. Use of IKONOS satellite data to identify informal settlement in Dehradun, India. *International journal of Remote Sensing*, 28(15): 3227-3233.

[26] Tatem, A.J., Lewis, H.G., Atkinson, P.M., and Nixon, M.S., 2003. Increasing the spatial resolution of agricultural land cover maps using Hopfield neural network. *International journal of Geographical Information science,* 17(7): 647-672.

[27] 2003. *EO-1 User Guide*, USGS Earth Resources Observation System Data Centre (EDC).

[28] ITT visual Information Solutions, http://www.ittvis.com, Accessed 19th August 2007

[29] Goodenough,D.G.,Pearlman,J.S.,Murdoch,M.,Han,T.,Chen,H., and West.C., 2003. Processing Hyperion and ALI for Forest Classification. *IEEE Trans.on Geosci.and Remote Sensing*, 41(6): 1321-1331.

[30] 2006. ITT visual information Solution, *FLAASH Module User's Guide*.

[31] December 2006. *ENVI User Guide, Version 4.3*.

[32] *ASTER Product User Guide version,5.1*, http://www.science.aster.ersdac.or.jp/en/documents/users_guide/pdf.html, Accessed 28 October 2007.

[33] 2004. *Principles of Remote Sensing*. International Institute for Geo-Information and Earth Observation, 3. ITC, Enscede.

[34] *Geo eye IKONOS User Guide*, http://www.geoeye.com/whitepapers_pdfs/GeoEye_IKONOS_product_Guide_v17.pdf Accessed October, 28th 2007.

[35] 2006. *Introduction to the R Project statistical computing for use at ITC*, Enschede.

[36] Anne H Schistad Solberg, T. T., and K Jain, A., 1996. A Markov Random Field Model for Classification of Multisource Satellite Imagery. *IEEE Trans.on Geosci.and Remote Sensing*, 34(1): 100-113.

[37] Christopher,M.Bishop., 2006. *PATTERN RECOGNITION AND MACHINE LEARNING*. Springer, New York.

[38] Cai.J., and Zhi-Qiang, L., 2001. Pattern recognition using Markov random field models. *PATTERN RECOGNITION*, 35: 725-733.

[39] Sikazwe, J., 2007. Optimizing Markov Random Fields for Super Resolution Land cover mapping (*IFA report*), ITC, The Netherlands.

[40] Kuckartz, J., 2007, Super Resolution Mapping Using Markov Random Fields, *Bsc Thesis*: Enschede, University of Twente ,The Netherlands,

[41] Kitaw.H.G., 2006. Image pan-sharpening with Markov Random Field and Simulated Annealing, *Msc Thesis*, ITC, Enscede.

[42] S.Z.Li., 1995, *Markov Random Field Modelling in Computer Vision*, Springer

[43] Ji, M.J., 1999. Effectiveness of Sub pixel Analysis in detecting and Quantifying Urban Imperviousness from Land Sat Thematic Mapper. *Geocarto International*, 14: 31-39.

[44] Tatem, A.J., Lewis, H.G., Atkinson, P.M., and Nixon, M.S.,1998. *Uncertainty in remote Sensing and GIS*.

[45] Nishii, R, Tanaka, S., 1999. Accuracy and Inaccuracy Assessment in land-cover classification. *IEEE Trans.on Geosci.and Remote Sensing*, 37(1): 491-497.

Appendix A

Hyperion linear unmixing & OSRM generation for the IKONOS degraded image.

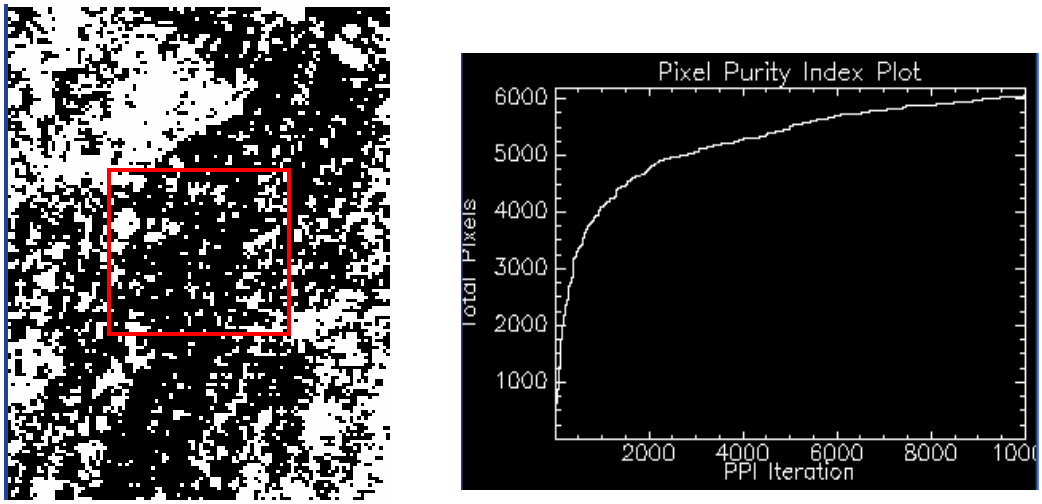

Fig A. 1 PPI image and the corresponding PPI plot for the Hyperion image

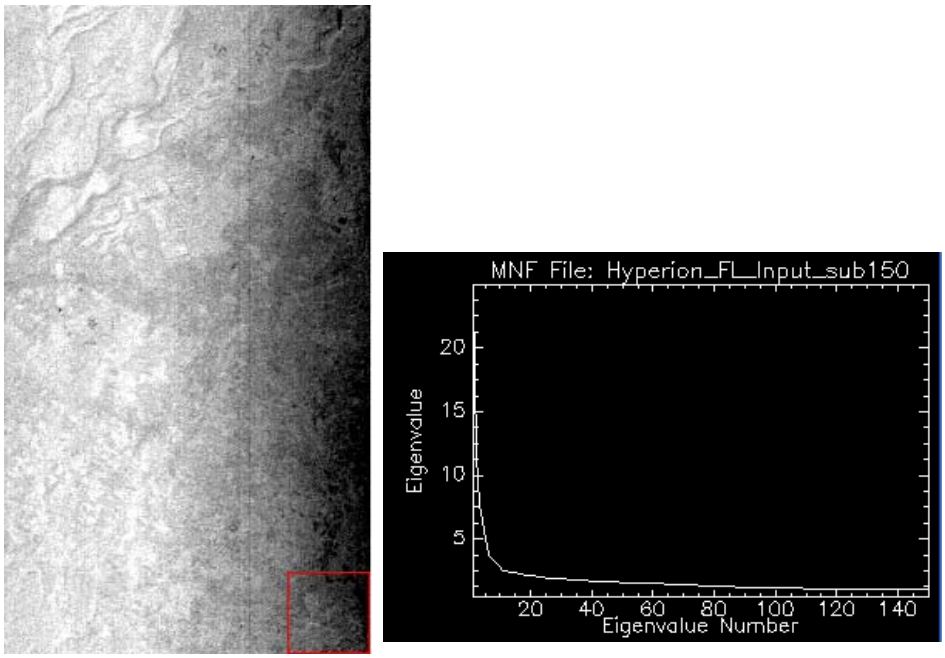

Fig A. 2"Smilling" effect inherent to Hyperion data recognized by the 1 MNF image, and the respective MNF plot

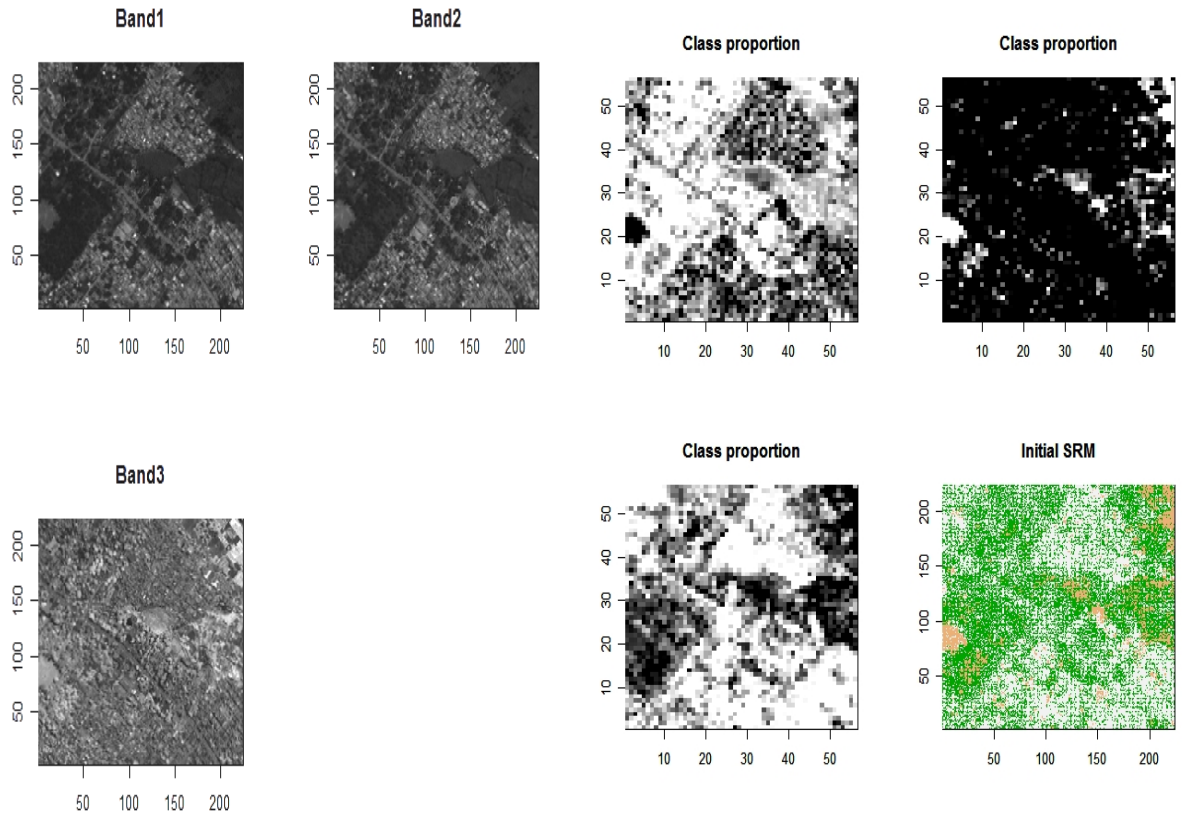

Fig A. 3 Degraded IKONOS VNIR bands with 16m spatial resolution and the fraction images generated from SVD

```
Input File: ikonstudyarea
    ROI Name: (Jeffries-Matusita, Transformed Divergence)

Vegitation [Green] 1011 points:
    Soil [Orange1] 1226 points: (1.66690558 1.99002770)
    Imperviousurface [Maroon] 243 points: (1.87790340 1.99994040)

Soil [Orange1] 1226 points:
    Vegitation [Green] 1011 points: (1.66690558 1.99002770)
    Imperviousurface [Maroon] 243 points: (1.39904981 1.60690713)

Imperviousurface [Maroon] 243 points:
    Vegitation [Green] 1011 points: (1.87790340 1.99994040)
    Soil [Orange1] 1226 points: (1.39904981 1.60690713)

Pair Separation (least to most):

Soil [Orange1] 1226 points and Imperviousurface [Maroon] 243 points - 1.39904981
Vegitation [Green] 1011 points and Soil [Orange1] 1226 points - 1.66690558
Vegitation [Green] 1011 points and Imperviousurface [Maroon] 243 points - 1.87790340
```

Fig A. 4 Class separability for the Degraded IKONOS image

Table A. 1 Class mean values for the IKONOS image

Class	Band1	Band2	Band3
Vegetation	351.827893	363.871414	548.546983
Soil	396.513051	451.156607	625.654160
Impervious Surface	479.440329	553.683128	512.518519

Table A. 2 Standard deviations for the class samples in IKONOS image

Class	Band1	Band2	Band3
Vegetation	14.887102	27.390814	95.120427
Soil	61.992404	77.054330	129.454111
Impervious Surface	59.724986	91.990536	92.585557

Table A. 3 Class covariance information for the IKONOS image

Vegetation	Band1	Band2	Band3
Band1	221.625795	358.486759	317.059579
Band2	358.486759	750.256717	1147.502087
Band3	317.059579	1147.502087	9047.895563
Soil			
Band1	3843.058197	4691.271424	3862.055946
Band2	4691.271424	5937.369740	4461.107266
Band3	3862.055946	4461.107266	16758.366828
Impervious Surface			
Band1	3567.073904	5407.557460	3807.183961
Bnad2	5407.557460	8462.258681	6399.569942
Bnad3	3807.183961	6399.569942	8572.085399

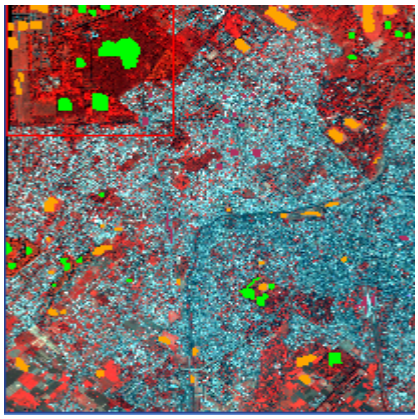

	ROI Name	Color	Pixels	Polyg
	Vegitation	Green	1,011	0/0
	Soil	Orange 1	1,226	0/0
*	Imperviousssurfac	Maroon	243	0/0

Fig A. 5 Training samples on IKONOS image and the respective number of training pixels per each class

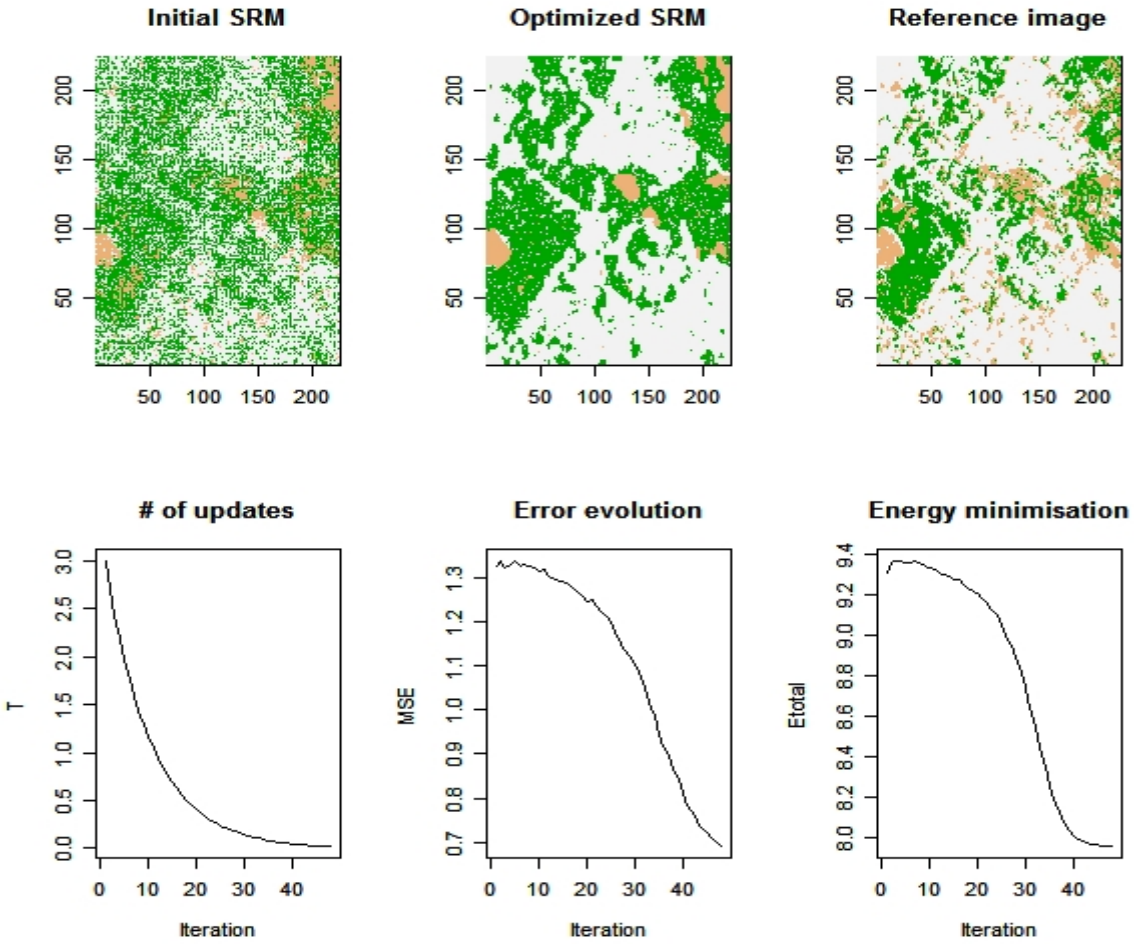

Fig A. 6 Initial SRM and optimized SRM for the IKONOS degraded image for an optimal smoothening value of 0.35

Appendix B

OSRM generation for the ASTER (VNIR) Image

```
Input File: asterstudyarea
    ROI Name: (Jeffries-Matusita, Transformed Divergence)

Vegitation [Green] 1011 points:
    Soil [Orange1] 1226 points: (1.83281559 1.95191797)
    Imperviousurface [Maroon] 243 points: (1.99948184 1.99999701)

Soil [Orange1] 1226 points:
    Vegitation [Green] 1011 points: (1.83281559 1.95191797)
    Imperviousurface [Maroon] 243 points: (1.74757939 1.98967135)

Imperviousurface [Maroon] 243 points:
    Vegitation [Green] 1011 points: (1.99948184 1.99999701)
    Soil [Orange1] 1226 points: (1.74757939 1.98967135)

Pair Separation (least to most):

Soil [Orange1] 1226 points and Imperviousurface [Maroon] 243 points - 1.74757939
Vegitation [Green] 1011 points and Soil [Orange1] 1226 points - 1.83281559
Vegitation [Green] 1011 points and Imperviousurface [Maroon] 243 points - 1.99948184
```

Fig B. 1 Class separability for the ASTER 16m image

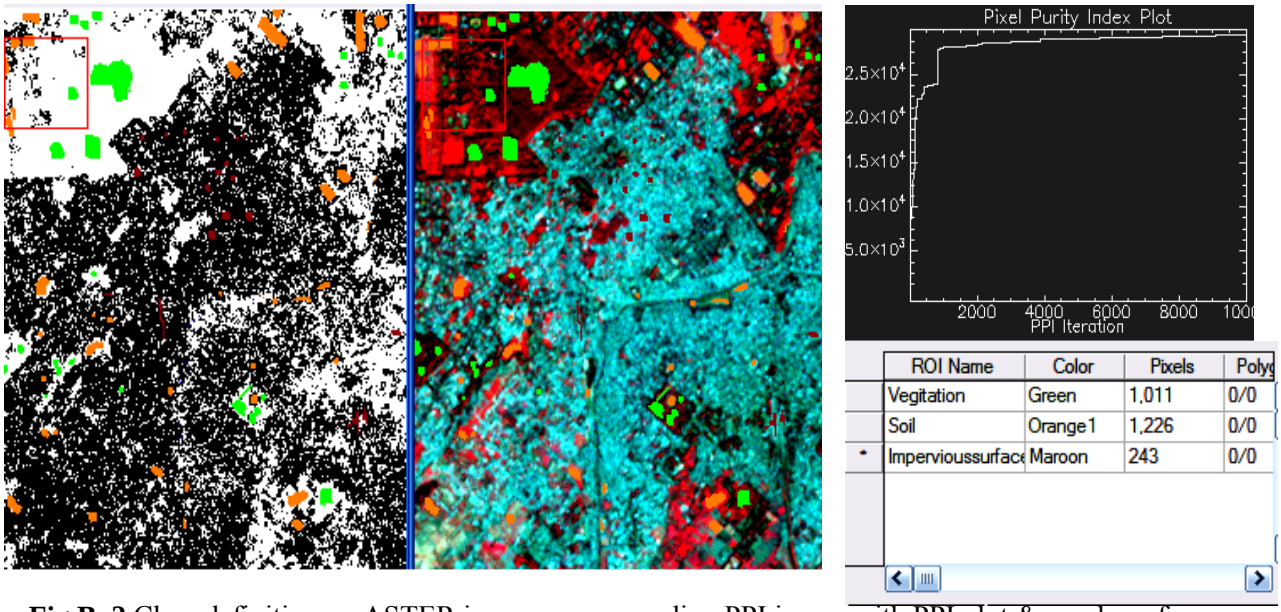

Fig B. 2 Class definition on ASTER image, corresponding PPI image with PPI plot & number of training pixels per each class

Table B. 1 Class mean values for the ASTER (VNIR) image

Class	Band1	Band2	Band3
Vegetation	20.091988	13.814045	45.396637
Soil	25.044861	20.464927	54.473083
Impervious Surface	30.205761	27.049383	40.061728

Table B. 2 Slandered deviations for the class samples in ASTER (VNIR) image

Class	Band1	Band2	Band3
Vegetation	1.204137	1.190324	3.611855
Soil	2.231231	3.465397	6.213061
Impervious Surface	30.205761	27.049383	40.061728

Table B. 3 Class covariance information for the ASTER (VNIR) image

Vegetation	Band1	Band2	Band3
Band1	1.449946	1.176528	1.387240
Band2	1.176528	1.416872	1.378780
Band3	1.387240	1.378780	13.045494
Soil			
Band1	4.978394	7.153820	-5.955118
Band2	7.153820	12.008973	-12.780129
Band3	-5.955118	-12.780129	38.602132
Impervious Surface			
Band1	6.428562	6.576574	4.764106
Bnad2	6.576574	7.857055	5.612642
Bnad3	4.764106	5.612642	10.363942

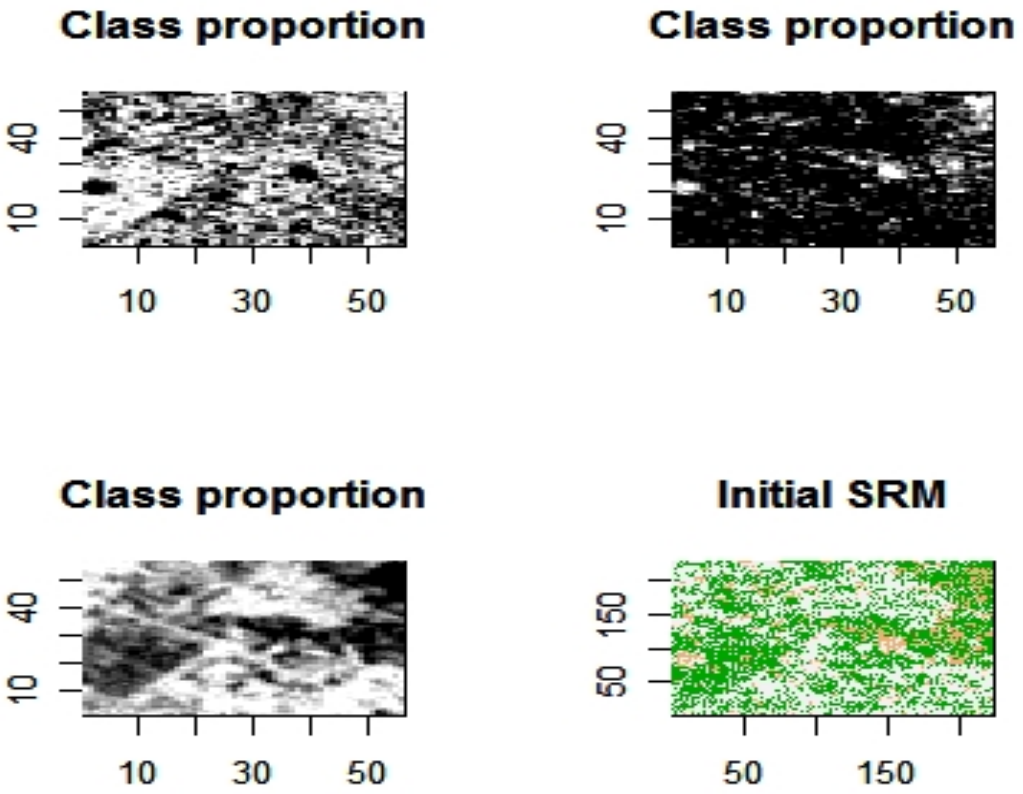

Fig B. 3 Fraction images and the initial SRM for the ASTER (VNIR) image

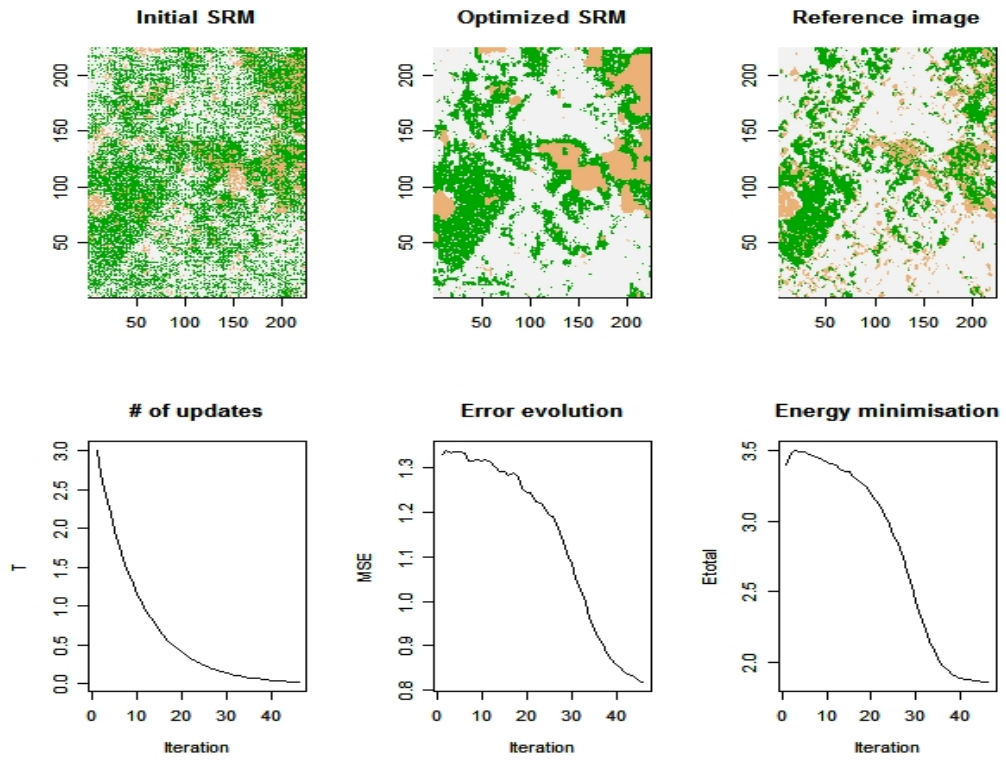

Fig B. 4 optimization process for $\lambda = 0.45$ in the ASTER (VNIR) image

OSRM generation for ASTER (SWIR) image

```
Input File: Aster_study_subIkon2
    ROI Name: (Jeffries-Matusita, Transformed Divergence)

Vegitation [Green] 1011 points:
    Soil [Orange1] 1226 points: (1.92145947 1.99768203)
    Imperviousurface [Maroon] 243 points: (1.99975796 1.99999964)

Soil [Orange1] 1226 points:
    Vegitation [Green] 1011 points: (1.92145947 1.99768203)
    Imperviousurface [Maroon] 243 points: (1.78422329 1.99904808)

Imperviousurface [Maroon] 243 points:
    Vegitation [Green] 1011 points: (1.99975796 1.99999964)
    Soil [Orange1] 1226 points: (1.78422329 1.99904808)

Pair Separation (least to most):

Soil [Orange1] 1226 points and Imperviousurface [Maroon] 243 points - 1.78422329
Vegitation [Green] 1011 points and Soil [Orange1] 1226 points - 1.92145947
Vegitation [Green] 1011 points and Imperviousurface [Maroon] 243 points - 1.99975796
```

Fig B. 5 Class separability for the ASTER 30m image

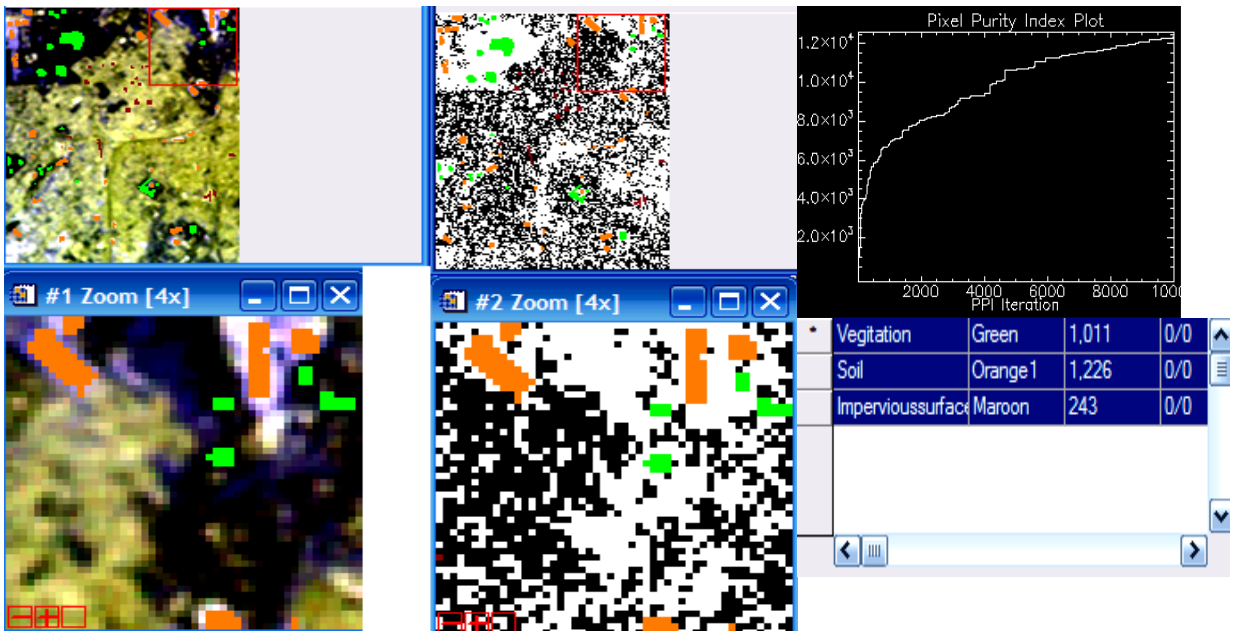

Fig B. 6 Class definition on ASTER (SWIR) image, corresponding PPI image with PPI plot & number of training pixels per each class.

Table B. 4 Class mean values for the ASTER (SWIR) image

Class	Band1	Band2	Band3	Bnad4	Band5	Band6
Vegetation	58.511375	43.348170	41.506429	37.083086	32.054402	33.912957
Soil	106.316476	73.104405	79.681077	69.680261	63.058728	51.718597
Impervious Surface	86.205761	77.855967	83.164609	75.547325	72.864198	60.539095

Table B. 5 Standard deviations for the class samples in ASTER (SWIR) image

Class	Band1	Band2	Band3	Bnad4	Bnad5	Band6
Vegetation	7.036723	5.311620	5.798490	5.665338	4.901001	2.896625
Soil	14.386025	9.381033	12.391185	10.562647	11.340870	7.856879
Impervious Surface	6.012285	4.969310	6.559775	6.135591	6.732958	4.779596

Table B. 6 Class covariance information for the ASTER (SWIR) image

Vegetation	Band1	Band2	Band3	Band4	Band5	Band6
Band1	49.515465	33.721778	38.158590	36.631727	15.232982	16.645546
Band2	33.721778	28.213311	29.657165	29.196786	25.031535	13.984791
Band3	38.158590	29.657165	33.622483	32.127188	27.694204	15.530263
Band4	36.631727	29.196786	32.127188	32.096060	27.046961	15.232982
Band5	30.771163	25.031535	27.694204	27.046961	24.019810	13.403750
Band6	16.645546	13.984791	15.530263	15.232982	13.403750	8.390436
Soil						
Band1	206.957720	97.287748	141.668361	111.751068	105.747930	62.261375
Band2	97.287748	88.003785	113.760671	98.086471	104.486925	70.509404
Band3	141.668361	113.760671	153.541470	128.928149	136.015480	90.702834
Band4	111.751068	98.086471	128.928149	111.569520	117.741242	79.439747
Band5	105.747930	104.486925	136.015480	117.741242	128.615324	87.401846
Band6	62.261375	70.509404	90.702834	79.439747	87.401846	61.730544
Impervious Surface						
Band1	36.147570	26.414056	35.077560	31.878652	32.689215	20.301840
Bnad2	26.414056	24.694045	31.656038	29.698993	32.348128	21.656481
Bnad3	35.077560	31.656038	43.030643	39.211186	42.617488	28.605108
Band4	31.878652	29.698993	39.211186	37.645478	40.062239	27.187192
Band5	32.689215	32.348128	42.617488	40.062239	45.332721	30.809050
Band6	20.301840	21.656481	28.605108	27.187192	30.809050	22.844540

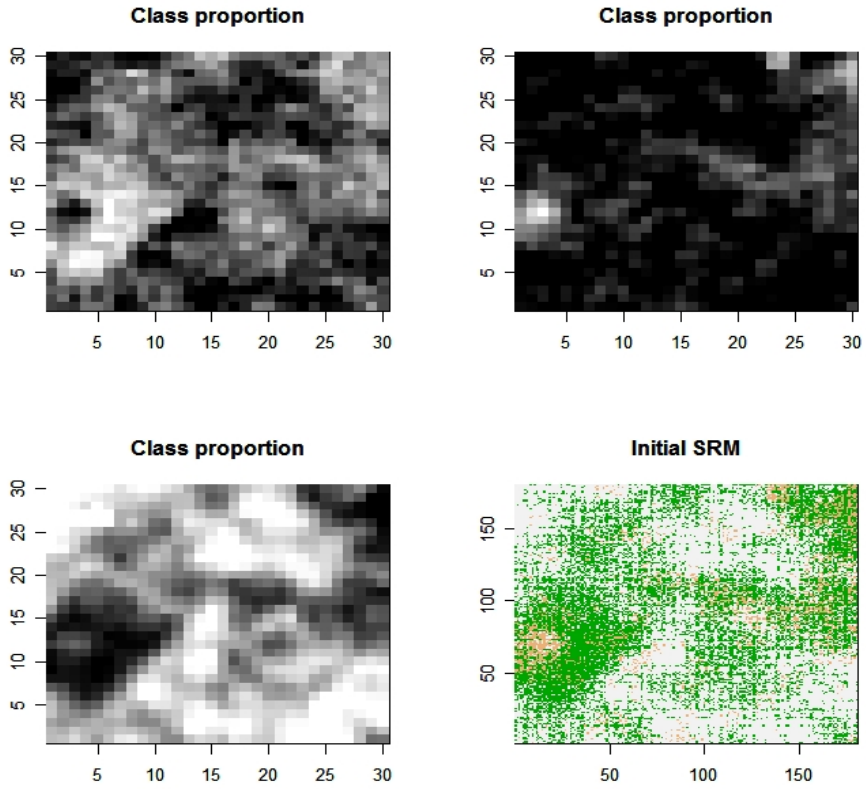

Fig B. 7 Fraction images and the initial SRM for the ASTER (SWIR) image

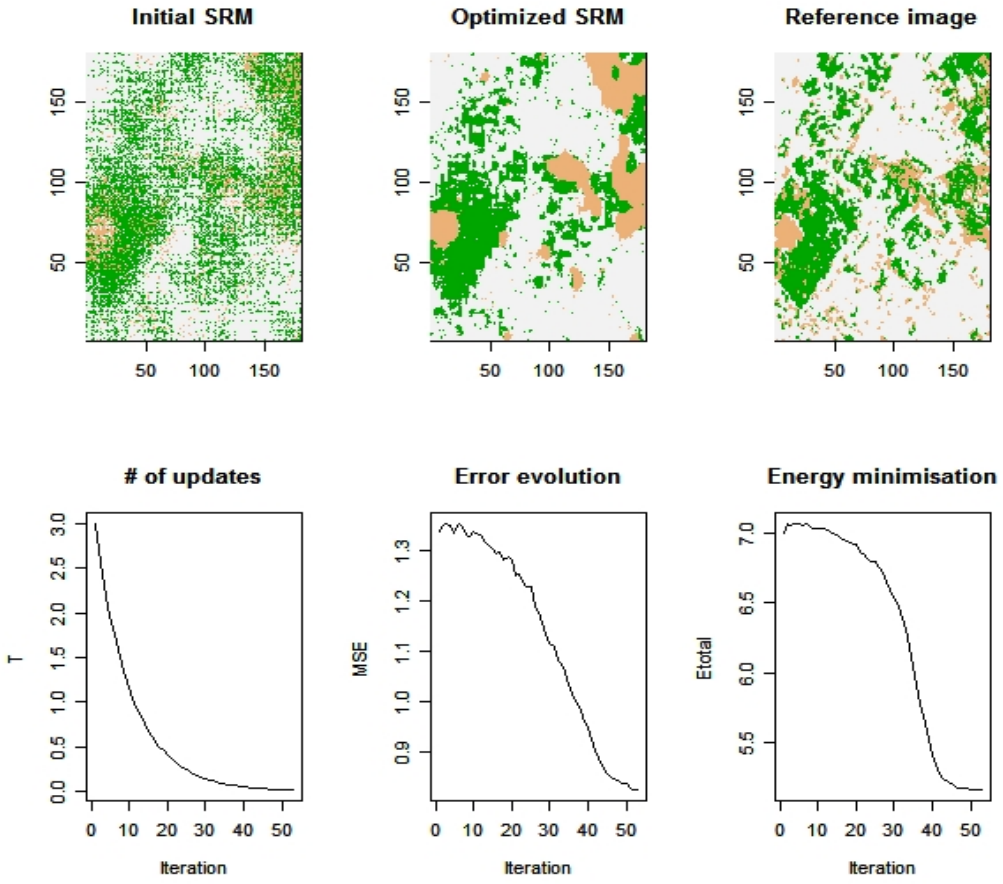

Fig B. 8 Optimization process for $\lambda = 0.25$ in the ASTER (SWIR) image

Appendix C

OSRM generation for the Landsat image

File

```
Input File: landsat_fromasterstudy_sub
    ROI Name: (Jeffries-Matusita, Transformed Divergence)

Vegitation [Green] 388 points:
    Soil [Orange1] 141 points: (1.82191037 1.95651391)
    Impervious [Magenta] 269 points: (1.97877915 1.99987144)

Soil [Orange1] 141 points:
    Vegitation [Green] 388 points: (1.82191037 1.95651391)
    Impervious [Magenta] 269 points: (1.98754606 1.99731256)

Impervious [Magenta] 269 points:
    Vegitation [Green] 388 points: (1.97877915 1.99987144)
    Soil [Orange1] 141 points: (1.98754606 1.99731256)

Pair Separation (least to most):

Vegitation [Green] 388 points and Soil [Orange1] 141 points - 1.82191037
Vegitation [Green] 388 points and Impervious [Magenta] 269 points - 1.97877915
Soil [Orange1] 141 points and Impervious [Magenta] 269 points - 1.98754606
```

Fig C. 1 Class separability for the Landsat image

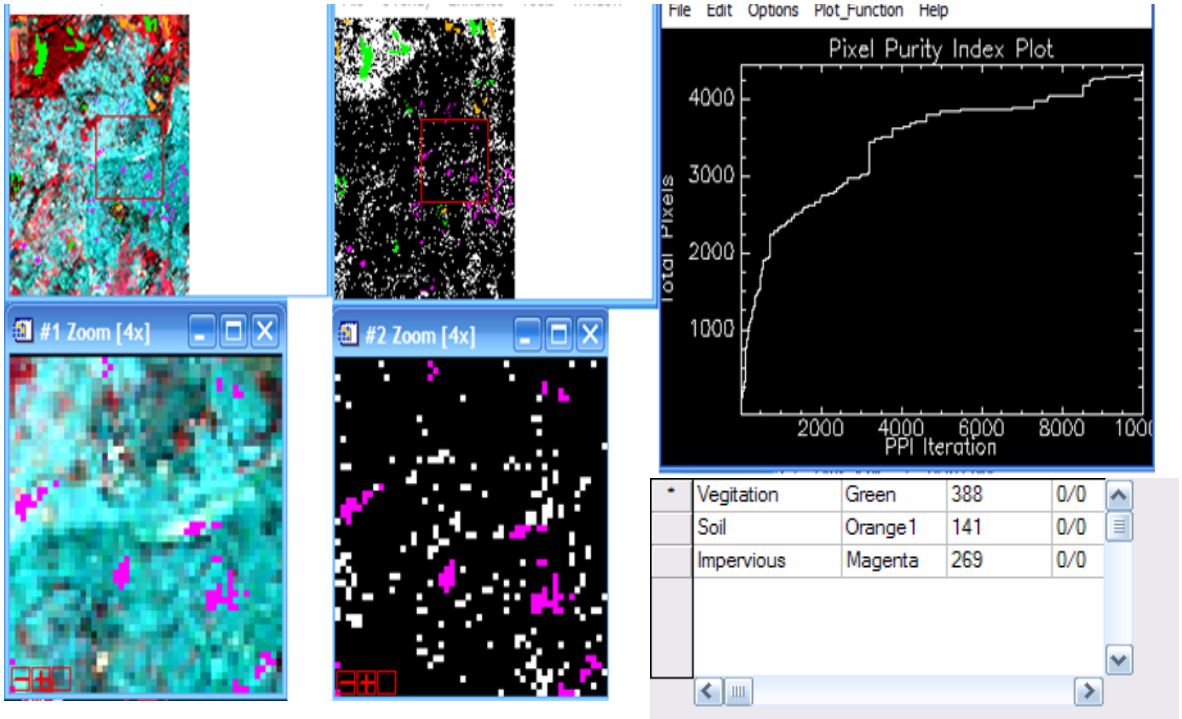

Fig C. 2 Class definition on Landsat image, corresponding PPI image with PPI plot & the number of training pixels per each class

Table C. 1 Class mean values for the Landsat image

Class	Band1	Band2	Band3	Bnad4	Band5	Band6
Vegetation	75.784387	62.148699	68.750929	60.234201	71.996283	62.401487
Soil	62.787234	50.971631	50.496454	90.070922	93.014184	56.950355
Impervious Surface	75.784387	62.148699	68.750929	60.234201	71.996283	62.401487

Table C. 2 Standard deviations for the class samples in Landsat image

Class	Band1	Band2	Band3	Bnad4	Bnad5	Band6
Vegetation	5.287797	8.187188	13.313991	13.252182	19.654573	17.463463
Soil	4.196612	5.424736	9.378261	8.630217	15.875401	13.204613
Impervious Surface	5.287797	8.187188	13.313991	13.252182	19.654573	17.463463

Table C. 3 Class covariance information for the Landsat image

Vegetation	Band1	Band2	Band3	Band4	Band5	Band6
Band1	11.145635	11.309358	14.358587	4.528251	17.264125	15.638216
Band2	11.309358	16.409414	17.912265	21.845907	31.251765	22.847492
Band3	14.358587	17.912265	24.664396	10.012087	31.904300	27.429806
Band4	4.528251	21.845907	10.012087	203.235322	108.700671	37.721157
Band5	17.264125	31.251765	31.904300	108.700671	115.254082	61.924532
Band6	15.638216	22.847492	27.429806	37.721157	61.924532	43.903434
Soil						
Band1	17.611550	20.365350	35.849240	8.800912	41.417325	45.167933
Band2	20.365350	29.427761	48.449899	17.823455	65.064691	64.805724
Band3	35.849240	48.449899	87.951773	24.157396	114.400051	114.674823
Band4	8.800912	17.823455	24.157396	74.480648	86.598987	49.060689
Band5	41.417325	65.064691	114.400051	86.598987	252.028369	194.529281
Band6	45.167933	64.805724	114.674823	49.060689	194.529281	174.361803
Impervious Surface						
Band1	27.960800	36.621733	54.449828	39.580536	61.868598	60.571964
Bnad2	36.621733	67.030045	105.339414	92.547134	142.377421	129.843062
Bnad3	54.449828	105.339414	177.262359	153.502580	239.525190	218.245894
Band4	39.580536	92.547134	153.502580	175.620318	243.612814	202.066068
Band5	61.868598	142.377421	239.525190	243.612814	386.302225	333.385826
Band6	60.571964	129.843062	218.245894	202.066068	333.385826	304.972535

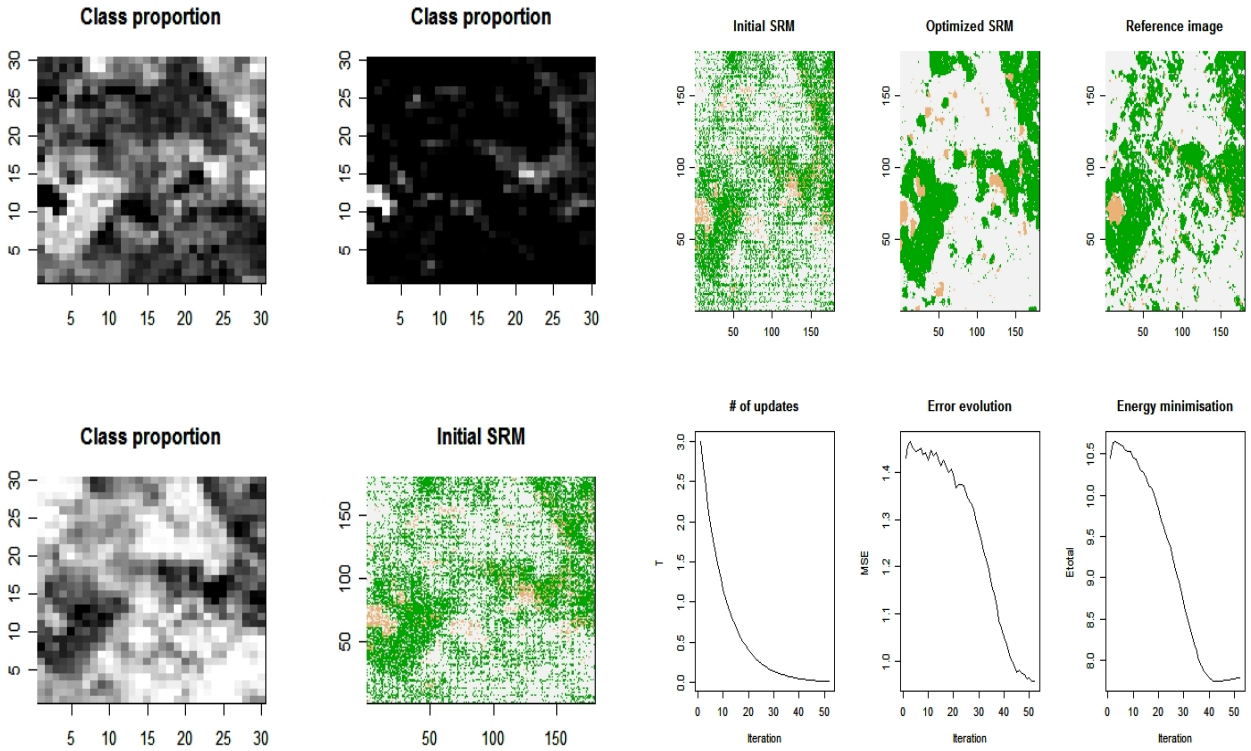

Fig C. 3 Fraction images and the initial SRM for the Landsat image and the Optimization process for $\lambda = 0.25$

Table C. 4 Log value of the determinant of the class covariance matrices for the input images

Input image	Radiometric resolution	$\frac{1}{2}\ln\det\sum_{\alpha}$
IKONOS Multispectral	Unsigned 16bit	10.646
ASTER (VNIR)	Unsigned 8bit	1.374
ASTER (SWIR)	Unsigned 8bit	4.833
Landsat	Unsigned 8bit	8.426